Radiation background studies for rare decay experiments

By

Harisree Krishnamoorthy

PHYS01201404019

Bhabha Atomic Research Centre, Mumbai - 400085

A thesis submitted
to the Board of Studies in
Physical Sciences

In partial fulfilment of requirements
For the Degree of

DOCTOR OF PHILOSOPHY
of
HOMI BHABHA NATIONAL INSTITUTE

February, 2020

ii

Homi Bhabha National Institute

Recommendations of the Viva Voice Committee

As members of the Viva Voice Committee, we certify that we have read the dissertation prepared by **Harisree Krishnamoorthy** entitled **"Radiation background studies for rare decay experiments"** and recommend that it may be accepted as fulfilling the thesis requirement for the award of Degree of Doctor of Philosophy.

	Date:
Chairman - Prof. B. K. Nayak	25-6-2020
Guide / Convener - Prof. Aradhana Shrivastava	25-6-2020
Co-Guide - Prof. Vandana Nanal	25-6-2020
Examiner - Prof. Samit Kr. Mandal	25-6-2020
Member 1 - Prof. Gobinda Majumdar	25-6-2020
Member 2 - Prof. Rudrajyoti Palit	25-6-2020
Member 3 - Prof. Satyajit Saha	25-6-2020

Final approval and acceptance of this thesis is contingent upon the candidate's submission of the final copies of the thesis to HBNI.

I hereby certify that I have read this thesis prepared under my direction and recommend that it may be accepted as fulfilling the thesis requirement.

Date: 25.6.2020

Place: Mumbai

Prof. Aradhana Shrivastava

DECLARATION

I hereby declare that the investigation presented in the thesis has been carried out by me. The work is original and has not been submitted earlier as a whole or in part for a degree/diploma at this or any other Institution/University.

February 2020, Mumbai

Harisree Krishnamoorthy

List of Publications arising from the thesis

Publications in Refereed Journal

Published

1. *Study of γ-ray background from cosmic muon induced neutrons*, **H. Krishnamoorthy**, G. Gupta, A. Garai, A. Mazumdar, A. Reza, S. Pal, S. Pethuraj, V. Nanal, A. Shrivastava, and R.G. Pillay, Eur. Phys. J. A **55**, 136 (2019)

2. *Thermal neutron induced γ-ray background in ^{124}Sn*, G. Gupta, **H. Krishnamoorthy**, A. Garai, A. Mazumdar, V. Nanal, A. Shrivastava, and R.G. Pillay, Applied Radiation and Isotopes, **158**, 4, (2020)

Refereed Conference Proceedinds

1. Muon Induced Neutron measurement setup at TIFR (MINT),**H. Kr- ishnamoorthy**, G. Gupta, A. Garai, A. Mazumdar, A. Reza, S. Pal, V. Nanal,

R.G. Pillay, A. Shrivastava, Prospects in Neutrino Physics (NuPhys2018), Cavendish Conference Centre 2018, edited by F. Di Lodovico, T. Katori, S. Pascoli, A.V. Titov, and J.R. Wilson, eConf C181219, 129 (2018) [arXiv:1903.09988v1]

Other Publications

1. *Study of the effect of external noise pickups on the performance of a cryogenic bolometer*, A. Garai, A. Reza, A. Mazumdar, **H. Krishnamoorthy**, G. Gupta, M. S. Pose, S. Mallikarjunachary, V. Nanal, R. G. Pillay, S. Ramakrishnan, Rev. Sci. Instrum. **90** (2019) 096104

2. *Studies on $\beta \leftrightarrow \alpha$ transition in Sn and Sn-rich alloys for a cryogenic tin bolometer*, A Mazumdar, A Garai, **H Krishnamoorthy**, G Gupta, A Reza, A Thamizhavel, V Nanal, R G Pillay and A Shrivastava, Materials Research Express **6** (2019) 076521

3. *Study of the Jacobi shape transition in A≈30 nuclei*, Balaram Dey, C. Ghosh, Deepak Pandit, A. K. Rhine Kumar, S. Pal, V. Nanal, R. G. Pillay, P. Arumugam, S. De, G. Gupta, **H. Krishnamoorthy**, E. T. Mirgule, Surajit Pal, and P. C. Rout , Phys. Rev. C **97**, 014317 (2018)

4. *New limit for the half-life of double beta decay of ^{94}Zr to the first excited state of ^{94}Mo*, N. Dokania, V. Nanal, G. Gupta, S. Pal, R. G. Pillay, P. K. Rath, V.I. Tretyak, A. Garai, **H. Krishnamoorthy**, C. Ghosh, P. K. Raina and K. G. Bhushan, Eur. Phys. J. A **53**, 74 (2017)

Symposium and conference proceedings

1. *Muon Induced Neutron measurement setup at TIFR (MINT)*, **H. Krishnamoorthy**, G. Gupta, A. Garai, A. Mazumdar, A. Reza, S. Pal, V. Nanal, R.G. Pillay, A. Shrivastava, Proceedings of the DAE Symp. on Nucl. Phys. **63** (2018) 1146.

2. *Assessment of borated rubber for neutron shield*, **H. Krishnamoorthy**, G. Gupta, A. Garai, A. Mazumdar, S. Pal, V. Nanal, R.G. Pillay, A. Shrivastava, Proceedings of the DAE Symp. on Nucl. Phys. **63** (2018) 1148

3. *The neutron induced γ-ray background in ^{124}Sn*, G. Gupta, **H. Krishnamoorthy**,
A. Garai, A. Mazumdar, V. Nanal, A. Shrivastava, R.G. Pillay, Proceedings of the DAE Symp. on Nucl. Phys. **63** (2018) 232.

4. *Modeling of an electrically cooled HPGe detector*, G. Gupta, **H. Krishnamoorthy**,
A. Garai, A. Mazumdar, A. Reza, V. Nanal, R.G. Pillay, Proceedings of the DAE Symp. on Nucl. Phys. **63** (2018) 1142.

5. *Radiopurity studies of tin-lead and tin-bismuth alloys for the development of a cryogenic bolometer*, A. Mazumdar, G. Gupta, A. Garai, **H. Krishnamoorthy**, A. Reza, V. Nanal, R. G. Pillay, A. Shrivastava, A.Thamizhavel, Proceedings of the DAE Symp. on Nucl. Phys. **63** (2018) 1152.

6. *A pulse height analysis technique for cryogenic bolometers*, A. Garai, A. Mazumdar, A. Reza, **H. Krishnamoorthy**, G. Gupta, V. Nanal, R.G. Pillay, Proceedings of the DAE Symp. on Nucl. Phys. **63** (2018) 1140.

7. *Design and. development of a front-end preamplifier for bolometric detector*, A. Reza, A. Garai, A. Mazumdar, V. Vatsa, **H. Krishnamoorthy**, G. Gupta, M.S. Pose, S. Mallikarjunachary, V. Nanal, R.G. Pillay, Proceedings of the DAE Symp. on Nucl. Phys. **63** (2018) 1124.

8. *Complete Fusion in ^9Be + ^{159}Tb at near barrier energies*, G. Gupta, Malika Kaushik, Swati Thakur, **H. Krishnamoorthy**, V. Nanal, A. Shrivastava, Pushpendra P. Singh, R.G. Pillay, C.S. Palshetkar, K. Mahata, K. Ramachandran, S. Pal, S. Pandit, V.V. Parkar, Proceedings of the DAE Symp. on Nucl. Phys. **63** (2018) 650.

9. *Study of fusion and direct reaction at near barrier energies in ^9Be + ^{197}Au*, Malika Kaushik, G. Gupta, Swati Thakur, **H. Krishnamoorthy**, V. Nanal, A. Shrivastava, Pushpendra P. Singh, R. G. Pillay, C. S. Palshetkar, K. Mahata, K. Ramachandran, S. Pal, S. K. Pandit, V. V. Parakar, Proceedings of the DAE Symp. on Nucl. Phys. **63** (2018) 598.

10. *Characterization of CLYC detector*,Balaram Dey, **H. Krishnamoorthy**, S. Pal, M.S, Pose, V. Nanal,R.G. Pillay, Proceedings of the DAE-BRNS Symp. on Nucl. Phys. **62**, (2017) 994.

11. *Radiopurity Study of CsI and CsI(Tl) detectors for the mini-DINO*, G. Gupta, **H. Krishnamoorthy**, A. Garai, A. Mazumdar, V. Nanal,R.G. Pillay,

S. Saha,S. Ghosh,S.G. Singh, Shashwati Sen, S.C. Gadkari, Proceedings of the DAE-BRNS Symp. on Nucl. Phys. **62**, (2017) 998.

12. *Radiopurity studies of indium-doped tin alloys for TIN.TIN*, A. Mazumdar, G.Gupta, J. Raval, A. Garai, **H. Krishnamoorthy**, V. Nanal, R.G. Pillay, A. Shrivastava, A. Thamizhavel, R. Mondal, Proceedings of the DAE-BRNS Symp. on Nucl. Phys.**62**, (2017) 1118.

13. *Anomaly in the giant dipole resonance spectrum of* ^{28}Si, Balaram Dey, C Ghosh, Deepak, Pandit, A K Rhine Kumar,S Pal, V Nanal, R G Pillay, P Arumugam, S De, **H. Krishnamoorthy**, G Gupta, E T Mirgule, Surajit Pal, P C Rout, Proceedings of the DAE-BRNS Symp. on Nucl. Phys. **62**, (2017) 446

14. *Estimation of Neutron Background in TIFR Low-Background Experimental Set-up (TILES)*, **H. Krishnamoorthy**, A. Garai, G. Gupta, N. Dokania, V. Nanal, R. G. Pillay, A. Shrivastava, Proceedings of the DAE-BRNS Symp. on Nucl. Phys. **61**, (2016) 1014.

15. *Study of Jacobi shape transition in cluster and non- cluster nuclei*, Balaram Dey, C. Ghosh, S Pal, D. Pandit, V. Nanal, R. G. Pillay, **H. Krishnamoorthy**, G. Gupta, P. C. Rout, E. T. Mirgule, Sukanya De, M.S. Pose, Surajit Pal, Proceedings of the DAE-BRNS Symp. on Nucl. Phys. **61**, (2016) 100

16. *Improvements to Tifr Low background Experimental Setup (TiLES)*, G. Gupta, N. Dokania, **H. Krishnamoorthy**, A. Garai, C. Ghosh, M.S. Pose,V. Nanal, R. G. Pillay, Proceedings of the DAE-BRNS Symp. on Nucl. Phys.**61**, (2016) 1026

17. *Study of radioactive impurities in NTD Ge sensors for mK thermometry*, A. Garai, G. Gupta, **H. Krishnamoorthy**, N. Dokania, V. Nanal, R. G. Pillay, A. Shrivastava, K. C. Jagadeesan, S. V. Thakare, Proceedings of the DAE-BRNS Symp. on Nucl. Phys. **61**, (2016) 1068

18. *Study of double beta decay of ^{94}Zr to the first excited state of ^{94}Mo*, N. Dokania, V. Nanal, G. Gupta, S. Pal, R. G. Pillay, P. K. Rath, V.I. Tretyak, A. Garai, **H. Krishnamoorthy**, C Ghosh, P.K. Raina, K.G. Bhushan, Proceedings of the DAE-BRNS Symp. On Nucl. Phys.**61**, (2016) 84

February 2020, Mumbai

Harisree Krishnamoorthy

DEDICATED TO

Amma and Appa for the unconditional love and support

Shri Mahaperiyava for the blessings and grace

ACKNOWLEDGEMENTS

Contents

List of Figures

List of Tables

List of Abbreviations

$0\nu\beta\beta$ Neutrinoless double beta decay

$2\nu\beta\beta$ Two neutrino double beta decay

BWH   Bodi West Hills

CFD   Constant Fraction Discrimination

CL   Confidence Level

DAQ   Data Acquisition system

DPP   Digital Pulse Processing

ENDF   Evaluated Nuclear Data File

FWHM   Full Width at Half Maximum

HDPE   High Density PolyEthylene

INO   India-based Neutrino Observatory

IO   Inverted Ordering

LAMPS   Linux Advanced Multi-Parameter System

MINT   Muon Induced Neutron measurement setup at TIFR

NO   Normal Ordering

NTD Ge   Neutron Transmutation Doped Germanium

PSD   Pulse Shape Discrimination

ROI   Region Of Interest

SIMS   secondary ion mass spectroscopy

$\mathbf{t}_c$ Cooldown time after neutron irradiation

$\mathbf{T}_{data}$ Counting period of the gamma ray spectrum

TiLES   Tifr Low background Experimental Setup

TIN.TIN   The INdia-based TIN detector

Synopsis

Neutrinos were proposed by W. Pauli in 1930 to explain the continuous energy spectrum of electrons from nuclear β decay [1]. Direct experimental detection of neutrinos happened in 1956, with the detection of $\bar{\nu}_e$ by Clyde L. Cowan and Frederick Reines in a nuclear reactor based experiment [2]. It was initially thought that neutrinos could be massless. The observation of neutrino oscillations robustly establishes that neutrinos have finite mass. However, the oscillation experiments are sensitive only to the mass squared differences and not to the absolute neutrino masses. The nature of neutrinos, which can be Dirac (particle and antiparticle is distinct) or Majorana (particle and antiparticle is the same), is another open question of fundamental importance that remains to be answered [3].

Double beta decay ($2\nu\beta\beta$) is a second order weak interaction process, that occurs in nuclei in which the single beta decay is either energetically forbidden or spin suppressed [4]. A nucleus N(A,Z) transforms to N(A,Z+2) by $2\nu\beta\beta$ as:

$$N(A, Z) \rightarrow N(A, Z + 2) + 2e^- + 2\bar{\nu}_e \tag{1}$$

There are around 35 naturally occurring isotopes in which $2\nu\beta\beta$ is possible, thirteen of which have been measured in direct experiments [5, 6]. The typical observed $T_{1/2}$ for $2\nu\beta\beta$ is $> 10^{18}$ years. If neutrinos are Majorana particles with non zero mass, the above process can also proceed via neutrinoless double beta decay ($0\nu\beta\beta$) [7] which violates the lepton number by two units ($\Delta L = 2$). The Neutrinoless double beta decay is perhaps the only experimental probe to understand the nature of the neutrino and one of the experiments sensitive to the absolute neutrino mass. The $T_{1/2}^{0\nu}$ is related to the effective neutrino mass $\langle m_{2\beta} \rangle$ by:

$$\frac{1}{T_{1/2}^{0\nu}} = G_{0\nu} |M_{0\nu}|^2 \frac{|\langle m_{2\beta} \rangle|^2}{m_e^2} \tag{2}$$

where $G_{0\nu}^N$, $M_{0\nu}^N$ and m_e are the phase space factor, nuclear matrix element and electron mass, respectively. In the case of observation of signal for $0\nu\beta\beta$, the half life $T_{1/2}^{0\nu}$ can be obtained from the relation :

$$T_{1/2}^{0\nu} = ln2 \frac{N_A \epsilon M i t}{A N_{obs}} \tag{3}$$

where N_A is the Avogadro's number, ϵ is the detection efficiency, i is the isotopic abundance, M is the detector mass, A is the molar mass, N_{obs} is the number of events attributed to $0\nu\beta\beta$ and t is the duration of measurement. In the case of non-observation, a lower limit on the $T_{1/2}$ of $0\nu\beta\beta$ can be placed as:

$$T_{1/2}^{0\nu} > \frac{N_A i \epsilon}{A f_{CL}} \sqrt{\frac{Mt}{N_{bkg} \Delta E}} \tag{4}$$

where f_{CL} is the number of standard deviations corresponding to a given confidence interval, N_{bkg} is the number of background events per unit energy expressed in $(keV^{-1}kg^{-1}y^{-1})$ and ΔE is the detector resolution.

Major experimental efforts are currently underway to study $0\nu\beta\beta$ in various candidate isotopes [7]. No experiment has observed an unquestionable $0\nu\beta\beta$ signal till date. The best limits achieved for $T_{1/2}^{0\nu}$ (at 90% C.L.) is $T_{1/2}^{0\nu}$ (^{136}Xe) > 1.07×10^{26} y by KamLAND-Zen experiment [8]. *TIN.TIN* collaboration at TIFR aims to develop cryogenic tin bolometer for the study of $0\nu\beta\beta$ in ^{124}Sn [9]. The ^{124}Sn has an isotopic abundance of 5.8% and a moderately high $Q_{\beta\beta}$ value of 2.2911 ± 0.0015 MeV [10]. Tin becomes superconducting at 3.7 K and can be used as a calorimetric detector at mK. Cryogenic bolometer detectors have excellent energy resolution ($\sim 0.2\%$) and hence well suited for $0\nu\beta\beta$ studies.

Given the rare nature of $0\nu\beta\beta$, the background reduction is extremely important to achieve the required sensitivity levels. The sources of background includes natural radioactivity (α, β, γ rays and neutrons), cosmic muons and muon induced shower of secondary particles. The contribution from natural radioactivity can be minimized by choosing materials of high radiopurity and appropriate active/passive shielding. The cosmic muon flux can be cut down by going underground. Among the muon induced secondaries, neutrons pose a serious difficulty due to the production in the detector vicinity and hard energy spectrum [11, 12]. These neutrons can give rise to γ ray background via $(n, n'\gamma)$ reactions or through (n, γ) reactions after thermalization. The high energy γ ray background can adversely affect the sensitivity of the experiment.

This thesis is focussed on understanding of different aspects and impact of neutron background for $0\nu\beta\beta$ in ^{124}Sn . The secondary neutron production from

cosmic muons was assessed with two independent measurements which involves indirect and direct experimental detection of cosmic muon induced neutrons. The γ ray background from fast neutrons produced by cosmic ray muons in TiLES low background HPGe set up is measured from $(n, n'\gamma)$ reactions in Ge detector and Cu shield. The contribution to secondary neutron production from stopping and non stopping muons is also independently assessed from MINT experiment which involves the direct detection of neutrons after thermalization. Materials such as borated rubber and high density polyethylene (HDPE) have been studied to assess neutron attenuation properties and radiopurity. The γ background arising from thermal neutron capture reactions in ^{124}Sn has been studied by thermal neutron irradiation and the contribution of thermal neutron induced γ ray background to the region of interest for $Q_{\beta\beta}$ in ^{124}Sn is also presented.

Neutron absorption studies

Shield design for low background experiments needs to optimized for minimizing γ ray and neutron background arising from the detector surroundings. Hydrogen rich materials such as polyethylene or rubber, loaded with Boron are well suited for this purpose. Thermal neutrons are attenuated by ^{10}B(n, α) reaction, without generating any additional γ ray background. The attenuation of thermal neutron flux was studied as a function of Boron loading in the Borated rubber with ^{252}Cf neutron source. It was observed that the thermal neutron counts significantly decreases with 10% Boron loading (90% of the thermal neutron flux is attenuated) and saturates (to a value of 92%) at around 30% of Boron loading. Fast neutron activation of the borated rubber sample was also done at the Pelletron Linac facility, with neutron flux $\phi_n \sim 10^6 \ ncm^{-2}s^{-1}$ to assess the

γ ray background that may arise from dissolved impurities in the rubber. The presence of Zn was observed in borated rubber, which makes it undesirable for application in low background experiments.

In order to understand the thermalization of fast neutrons in the HDPE and to optimize the absorber thickness for studying cosmic muon induced neutrons, measurements were carried out with fast neutrons from ^{249}Am-^{9}Be and ^{252}Cf sources. The absorber thickness was optimized to 10 cm, in order to detect both thermal neutrons and 2.2 MeV γ ray. For ^{252}Cf source ($E_n^{max} \sim 10$ MeV), 5 cm thick HDPE thermalizes ~50% of the neutrons. Further, ~80% of the thermalized neutrons are absorbed in 5 cm HDPE.

Muon Induced Neutron measurement setup at TIFR (MINT)

The MINT is designed to detect neutrons originating from cosmic muon induced reactions in the target materials after thermalization using Cs_2LiYCl_6 (CLYC)(1 inch $\times$ 1 inch) and NaIL (2 inch $\times$ 4 inch) detectors. The intrinsic thermal neutron detection efficiency for CLYC and NaIL is the order of 25% and 50% respectively, with excellent pulse shape discrimination (PSD) capability. The detectors are surrounded by 10 cm thick HDPE (high density polyethylene). Four plastic scintillators are used in the setup for muon detection, two at the top and two at the bottom. The fast neutrons generated by muon interactions in the target are thermalized in 10 cm thick HDPE surrounding the detectors and detected by ^{6}Li$(n, \alpha)^3$H reaction, giving a unique energy signal with 3.2 MeVee light output. The digital data acquisition has been setup using CAEN V1730B digitizer (500 MHz, 14 bit ADC). The coincidence search, between a neutron

events in CLYC/NaIL and muon events is performed offline with ROOT[13] based analysis code. The γ ray 2.2 MeV is also visible in NaIL detector, though the yield could not be reasonably extracted due the Compton background arising from 2614.5 keV background γ ray.

Measurements have been performed with target blocks of 30 cm thickness and area of $40cm \times 40cm$ for Pb and $30cm \times 30cm$ for Fe. The contribution to the secondary neutron production from cosmic muons is assessed for stopping and non-stopping muons in the target, with suitable trigger definition of top and bottom muon detectors.

TABLE 0.1: Cosmic muon induced neutron yield with Pb and Fe. The errors quoted are statistical.

Target	Pb (n/μ)	Fe (n/μ)
Stopping muons	$8.80(0.26) \times 10^{-3}$	$1.22(0.23) \times 10^{-4}$
Non-stopping muons	$2.41(0.45) \times 10^{-2}$	$1.87(0.61) \times 10^{-3}$
Total	$3.27(0.52) \times 10^{-2}$	$1.99(0.65) \times 10^{-3}$

The neutron contribution from stopping muons in Pb is found to be a factor of 72 higher compared to the production in Fe, for the present geometry. The expected ratio is ~98, considering that the muon capture rate in target materials is expected to scale as Z^4.

γ-ray background from cosmic muon induced neutrons

Contribution to γ-ray background from secondary neutrons, originating from cosmic muon interactions in Pb-Cu composite shield of TiLES low background

HPGe detector [14], has been measured via $(n, n'\gamma)$ reactions in Cu and Ge. Cosmic ray muons entering the setup are detected with plastic scintillator detector placed above the setup.

The data adding to a live collection time of 329.2 d was acquired, corresponding to to $1.24 \pm 0.06 \times 10^9$ muon triggers. The data acquisition system consists of a commercial CAEN N6724 digitizer (14-bit ADC, 100 MS/s). The data from each detector is acquired on an event by event basis with a time stamp. The coincidence/anti-coincidence between HPGe and plastic scintillator is projected using offline algorithms developed in ROOT [13] and C++. The coincidence search algorithm filters γ-ray events in HPGe detector within a 50 μs time window of the muon trigger in the plastic scintillator. The optimal prompt time window was chosen to be T_{prompt} = 15 μs. The background includes contributions from chance coincidence, neutrons from non triggering muons, as well as ambient neutrons from natural radioactivity.
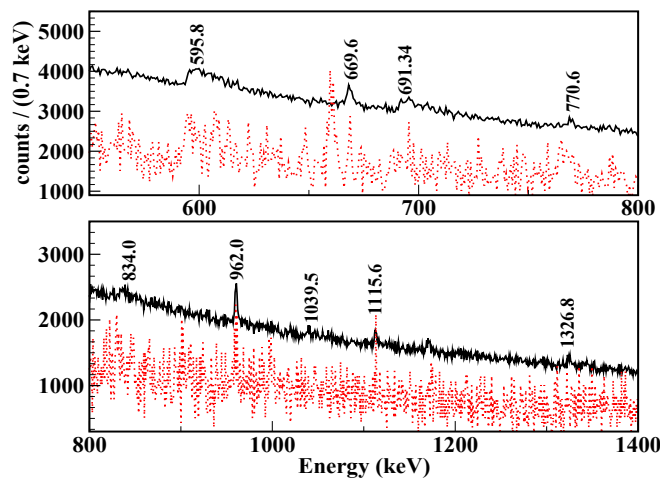
FIGURE 0.1: Prompt (black) and chance (red) gated γ-ray spectra in the TiLES HPGe detector. The chance gated spectrum has been scaled up by an arbitrary factor (~330) for better viewing (T_{data} = 329.2 days).

For Monte Carlo simulations, the energy and angular distributions of the cosmic ray muons were obtained from CORSIKA software [15]. These distributions of cosmic ray muons were used as input in GEANT4 [16, 17]. A total of 5×10^6 muons were generated with a charge ratio of 1.276 ± 0.003. Two versions of GEANT4, 10.00 and 10.05 each with two different Physics Lists, QGSP_BERT_HP and Shielding Physics are employed in the simulations. Neutron multiplicity, N_n/N_μ, was obtained between 0.111 and 0.126 for different simulation sets. The spatial and energy distribution of the generated neutrons were stored and used for the generation of γ rays from $(n, n'\gamma)$. A total of 1.435×10^8 neutron events were generated. Intensities of γ rays of interest are extracted from both measured and simulated spectra and are normalized to the incident muon counts for comparison. The choice of γ rays was restricted by measurable intensities above the background in the experimental spectrum to minimize the fitting errors. Given the broad line shapes in Ge, only 595.8 keV γ-ray of ^{74}Ge having highest intensity is considered, whereas in case of ^{63}Cu and ^{65}Cu yield of multiple prominent γ rays are used for comparison. While GEANT4.10.00 significantly under-predicts the γ-ray production in Cu, reasonably good agreement with the experimental data is obtained with GEANT4.10.05. The present $(n, n'\gamma)$ data provides crucial input for validation of GEANT4.10.05 simulation of both muon induced neutron production and neutron inelastic scattering. The simulations have further shown the presence of several high energy γ rays in the range 2-8 MeV and the contribution of the Compton tail of these high energy γ-rays to lower energy of interest (2-2.5 MeV) can be a significant factor for background in rare decay studies.

Thermal neutron induced γ-ray background in ^{124}Sn

The thermal neutron-induced γ-ray background in ^{124}Sn is investigated in connection with $0\nu\beta\beta$ studies in ^{124}Sn. A 99.26%-enriched sample of ^{124}Sn was irradiated at Dhruva reactor at BARC, Mumbai, with a thermal neutron fluence of 3×10^{15}/cm^2. The γ ray spectrum of the irradiated Sn sample was measured after a cool-down time of t_c, ~10 min. The $T_{1/2}$ of 331.9 keV γ ray, from ^{125m}Sn, was measured to be 10.01(8) min, which is consistent with the literature value [18]. No additional short-lived impurities were observed in the spectrum.

The irradiated sample was measured in TiLES [14] setup after a cooldown period of 1d. The observed intensities of most of the γ rays of interest from the decay of ^{125}Sn and ^{125}Sb are consistent with the reference values, except for very weak ($<$ 0.1%) high-energy γ-rays. The coincidence summing probability of two γ rays (γ_1, γ_2) in a given cascade to the photopeak of E_{γ_0} ($= E_{\gamma_1} + E_{\gamma_2}$) was evaluated using GEANT4 [17] simulations for a for a few energies of interest. The simulations illustrate that the intensities of the weak decay branches are affected by the coincident summing.

To assess the neutron-induced background in the ROI close to $Q_{\beta\beta}(^{124}$Sn), the spectrum of the irradiated Sn sample was measured in a close counting geometry after $t_c \sim$ 1 d and 39 d ($\sim 4T_{1/2}$) as well as after a prolonged cool-down time of 1.5 y. (see Fig. 0.2). Three energy windows namely, 2282–2300 keV (w1: $Q_{\beta\beta} \pm$ 9 keV), 2269–2281 keV (w2: photopeak region of the highest-energy γ ray in the ^{125}Sn decay cascade), and 2166–2265 keV (w3: as a measure of the integral background level), were chosen for the analysis. In the window
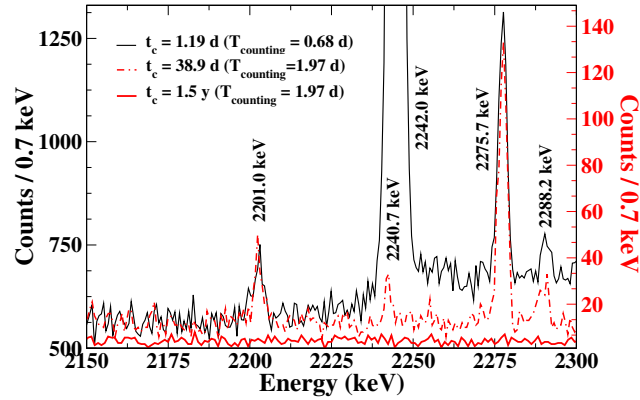
FIGURE 0.2: Comparison of energy spectra in the vicinity of region of interest after different cool-down times. The left scale corresponds to $t_c = 1.19$ d, while that for $t_c = 38.9$ d and 1.5 y is indicated on the right side.

w1, the peak at 2288.2 keV, which results purely from coincidence summing effect, is observed. The photopeak at 2275.7 keV was visible in the window w1. The measured yields are also compared with the expected yield inclusive of the coincident summing contribution obtained in the simulation and the counts showed a reduction consistent with $T_{1/2}(^{125}\text{Sn})$.

The activity due to $^{124}\text{Sn}(n,\gamma)$ in the 2282–2300 keV energy window, immediately after the irradiation, is estimated to be 14.4 mBq/g/keV for an incident neutron fluence of $3 \times 10^{15}/\text{cm}^2$. After the prolonged cool-down period of 1.5 y, the integral counts in all three energy windows are found to be similar to the ambient background. For energy windows w1 and w2, the minimum detectable limit for detection (L_D) can be estimated by Currie's method [19]. We obtain $L_D \sim 25$ μBq/keV. Hence, the activity after $t_c = 1.5$ y is found to be lower than 1 mBq/g/keV.

In a Sn detector module, the background contribution in the ROI will arise both from the high-energy electrons from the β- decay of ^{125}Sn to the ground state of ^{125}Sb ($I = 81\%$) and from the γ rays originating after the β-decay of

^{125}Sn to ^{125}Sb($\frac{11}{2}^{+}$) (I = 0.29%). The expected fraction of electrons in this energy window, which is close to Q_β, is $\approx 1 \times 10^{-3}$. Assuming that the decay cascade of ^{125}Sb($\frac{11}{2}^{+}$) is contained within the detector module, the maximum contribution to the background from γ rays is $\approx 3 \times 10^{-3}$ (of the order of the feeding fraction). To estimate the tolerable neutron dose, based on the observed background in the w1 energy range, a fraction of $\approx 5 \times 10^{-3}$ spread over a 10 keV window is assumed to contribute to the ROI. The prolonged exposure of ^{124}Sn to thermal neutrons will lead to a build-up of ^{125}Sn and the expected equilibrium concentration will be $\approx K/\lambda$, where K is the production rate and λ is the decay constant. To achieve a desired background rate of 10^{-2} counts/(kg y keV) in an energy window of 2282–2300 keV, the Sn detector material should not be exposed to a neutron flux larger than 3×10^{-5} n/cm^2/s during the handling or processing stages.

To summarize, various aspects of neutron background relevant to the study of rare event experiments have been looked at. From the MINT setup, the contribution to the neutron production for Pb and Fe targets are compared. The neutron production in Pb is found to higher by a factor of 72. The γ ray background from fast neutrons generated by cosmic muons in Pb/Cu composite shield of TiLES is investigated by $(n, n'\gamma)$ reactions. Monte Carlo simulations with GEANT4.10.05 shows good agreement with the experimental results for Shielding Physics list. The γ ray background to the crucial $Q_{\beta\beta}$ region in ^{124}Sn arising from thermal neutron capture is assessed to be 14.4 mBq/g/keV for an incident thermal neutron flux of 3×10^{15} neutrons/cm^2. Further, it is concluded that the Sn detector material should not be exposed to a thermal neutron flux greater than 3×10^{-5} neutrons/cm^2/s in order to achieve a background rate of

$\sim 10^{-2}$ in the ROI. Understanding and minimization of fast and thermal neutron background is crucial for achieving the required sensitivity in $0\nu\beta\beta$ experiments. This work provides important inputs towards the understanding the impact of neutron background for *TIN.TIN* experiment.

Introduction

The standard model of particle physics [20] is extremely successful in describing the fundamental constituents of matter and the forces through which they interact. It has convincingly explained many experimental results and made several predictions including the existence of Higgs boson [21–23], which was discovered in the Large Hadron Collider [24]. In spite of the success of the Standard Model, there are several fundamental questions which remain unanswered. The origin of the neutrino mass, the nature of neutrinos and the absolute neutrino mass [25], the existence of dark matter, the excess of matter over the antimatter in the universe etc. are some of the most important unresolved issues. Hence these processes are crucial probes for the physics beyond standard model. Several large scale experimental efforts have been initiated at different parts of the world for probing the neutrino oscillations [26–29], neutrinoless double beta decay and other rare nuclear decays [8, 30, 31], existence of dark matter [32–36], etc. As the signal rates are extremely low due to the rare nature of these processes, the experiments need to be meticulously designed for the choice of detector materials,

shielding configuration and background rejection strategies. Though the techniques employed to achieve the required sensitivity level varies from experiment to experiment, many of the requirements such as large detector mass, materials of high radiopurity, the employment of active and passive shields for background rejection etc. are common to all the rare event experimental searches. In addition to this, deep underground laboratories are chosen for housing the experiments, in order to mitigate the background contribution from cosmic muons. Therefore, the key challenge is achieving unprecedented background levels to be able to attain the required sensitivities.

The following sections briefly discuss the importance of background reduction for rare event searches, the sources of background, techniques of background reduction, followed by neutrino oscillations, neutrinoless double beta decay and experimental efforts directed towards detecting it. Finally, experiments designed to detect dark matter interactions is also briefly discussed, with emphasis on the low background aspects.

1.1 Rare event searches: The need for low background

The beginning of the low background physics started with neutrino physics experiments, which aimed to measure the solar and atmospheric neutrino fluxes. As the interaction probability for neutrinos is extremely low, the need for underground laboratories, large detectors and ultrapure materials became necessary. Subsequently, other rare and interesting processes like proton decay, neutrinoless double beta decay, dark matter interactions, cross section measurements related to nuclear astrophysics processes etc. were also studied with similar experimental

facilities. Various background techniques have been employed in these experiments to achieve ever-decreasing levels of radioactive backgrounds. Impressive limits on the cross sections and half lives of various rare processes have been obtained owing to the unprecedented levels of background achieved. Some of the experiments with best achieved background includes the KamLAND-Zen experiment searching for $0\nu\beta\beta$ in ^{136}Xe, with $N_{bkg} = 1.5 \times 10^{-4} \ keV^{-1}kg^{-1}y^{-1}$ [8] and XENON1T experiment with $N_{bkg} = 8.5 \times 10^{-2} keVee^{-1}kg^{-1}y^{-1}$ [35]. The measurement of double electron capture half life of $T_{1/2}^{ECEC}$ ^{124}Xe $= 1.8 \times 10^{22} \ y$ by XENON1T [37] experiment demonstrates the power of the ultra-low background achieved by the experiment. It is to be noted that the improvement in the background index is achieved in phases, by improving the background rejection strategies and implementing various analysis cuts over the data that is acquired for prolonged periods. The signature of any of these rare processes will not be individually unique, but must be distinguished on a statistical basis against the dominant background.

1.1.1 Sources of radiation background

- **Natural radioactivity**: The contribution from natural radioactivity arises from the α, β, γ rays from the decay chain of primordial isotopes ^{235}U,^{238}U, ^{232}Th and ^{40}K isotopes ($T_{1/2} \sim 10^9 - 10^{10}$ y). The high energy γ rays such as 2448 keV from ^{214}Bi and 2615 keV from ^{208}Tl constitutes an important source of background. Isotopes of Radon, namely, ^{222}Rn ($T_{1/2} = 3.8 \ d$),^{220}Rn ($T_{1/2} = 55.6 \ s$), ^{219}Rn ($T_{1/2} = 3.96 \ s$) are gaseous sources of radioactive background, that are produced in the decay chain of ^{238}U, ^{232}Th and ^{235}U, respectively. The α and β emitting isotopes, which can be present

as surface/volume contamination in the detector and the bremsstrahlung arising from them contributes to the background. This can contribute to additional β and γ ray events. Above 3 MeV, α emitting impurities are the chief source of background which needs to be minimized.

- **Cosmic rays**: Primary cosmic rays and the cosmic rays induced shower of particles constitutes important source of the background. Hence the rare decay experiments are performed at underground laboratory sites, such as under a mountain, with high overburden arising from the rock cover. Though the primary cosmic muons flux can be cut down by going deep underground and by active veto, the muon induced secondary particles are difficult to mitigate. The cosmic muons can directly deposit energy in the detector or give raise to background via secondary particles and cosmogenic activation[38, 39].

- **Neutron background**: Neutrons arises from the spontaneous fission of ^{235,238}U and ^{232}Th isotopes present in the rock and the surrounding materials. The alpha emitters can also induce (α,n) reaction in the lighter isotopes, giving rise to neutrons. These neutrons have energies $\lesssim 20$ MeV. Additionally, cosmic muons can also interact with the rock and the high-Z shielding materials surrounding the detector to produce neutrons that range in energy upto ~ 10 GeV. Neutrons can get thermalized and captured or inelastically scatter in the detector/surrounding materials to produce additional γ ray background. For example, the production of long lived isomeric states like ^{60}Co ($T_{1/2} = 1925$ d) and ^{56}Co ($T_{1/2} = 78$ d) in Cu, are also caused by neutron activation. Copper is a widely used material in

most of the experiments, either as a part of the detector setup or passive γ ray shielding and these reactions are of concern as they can contribute to the background [40].

1.1.2   Techniques of background reduction

The low background physics has emerged as a dedicated branch of study after the advent of the rare event experiments. As mentioned earlier, some of the sources of background like cosmic muons or the natural activity is common for all the experiments while other sources of background might be experiment specific. This section briefly discusses the strategies of background reduction that are employed by various experiments.

- **Radiopurity:** Minimizing the contamination of radioactive isotopes in the detector active volume and the surrounding shield materials is one of the most important factors. The α and β emitting isotopes within the detector fiducial volume needs to be minimized to the best possible levels. For example, in the case of Darkside experiment, the presence of ^{39}Ar isotope with $T_{1/2}$ = 239 y, Q_{β} = 565 keV at the level of 1 part in 10^{15} in the LAr-TPC, produces an activity of 1 Bq/Kg [36], when the Argon extracted from the atmospheric sources. The production of ^{39}Ar takes place typically via ^{40}Ar(n,2n)^{39}Ar reaction. Hence deep underground sources, that has been shielded from cosmic radiation for many half-lives of ^{39}Ar are extracted and purified to achieve ultra low levels of ^{39}Ar isotope concentration. The storage of the detector components in the underground location, is a commonly implemented method to reduce the cosmogenic background. The Borexino experiment that detects the low energy solar neutrinos from

[7]Be, employs liquid scintillator with radiopurity levels greater than $5 \times 10^{-15} g/g$ of U and Th equivalent (reported in mass concentration, per unit mass of detector components) [41]. In the case of XENON1T experiment, the levels of [85]Kr ($T_{1/2}$ = 10.74 *y*, Q_β = 687 *keV*) in LXe needs to be reduced to the concentration levels of 10^{-13} [35]. [222]Rn isotope, which is a progeny of [238]U with $T_{1/2}$ = 3.8 *d* is continuously supplied from the detector components. The implementation of radon suppression techniques by flushing the system with pure boil-off N_2 gas in a closed loop system, at a pressure slightly above the atmospheric pressure, mitigates the background arising from Radon. Purification systems based on adsorption and various other gas purification methods are also implemented [42–44].

- **Active shield for cosmic muons:** As discussed earlier, the interaction of cosmic ray muons and the shower of secondary particles generated is a common source of background for all the experiments with rare event signatures. All the rare event search experiments are hence housed at laboratories located in the deep underground, where the muon flux is significantly attenuated. Figure 1.1 shows the relation between the cosmic muon flux and the depth. The depth is measured in units of kilometer water equivalent (km.w.e), which corresponds to the depth of water in km, that is necessary to provide the same amount of shielding from cosmic ray muons. While the underground laboratories provides passive shield for the cosmic muons, additional active veto is often employed to mitigate the residual flux. In many of the major experiments, ultrapure water Cherenkov or liquid scintillator tanks outside the fiducial volume is used as active veto
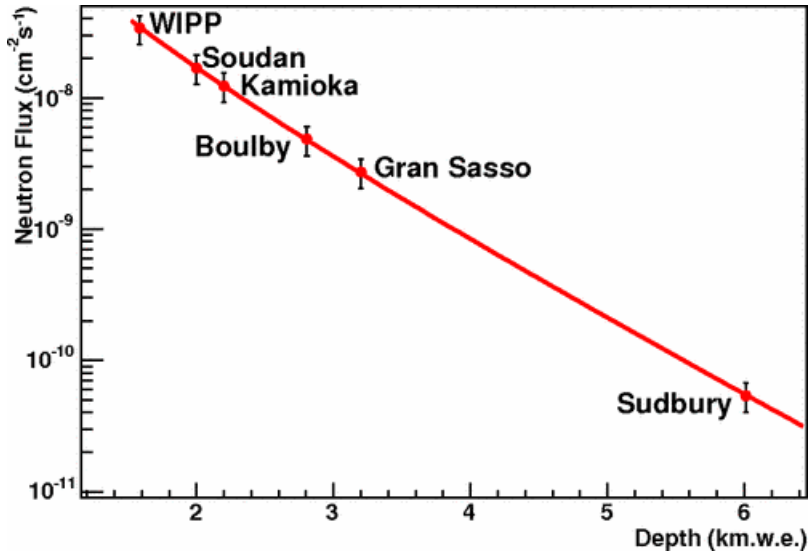
FIGURE 1.1: The comparison of the cosmic muon flux at various underground locations. Figure adapted from [11]

to eliminate the cosmic muons. In most of the cases, this also acts as passive shield against the external radioactive background. Active muon veto is also used to suppress the secondary particles, such as neutrons, that are generated by the cosmic muon interaction with the detector and the surroundings.

- **Passive shield:** The detector systems are shielded with passive graded shield to eliminate the external radioactive background from the immediate surroundings of the detector. The CDMS [45] and CRESST [46] experiments employ graded shielding of Cu and low activity Pb along with High Density Polyethylene (HDPE) blocks to shield against the external radiation (γ rays and neutrons). However, the presence of high-Z materials like Cu and Pb in the detector vicinity can lead to the generation of secondary particles from cosmic muon interactions. Shields based on

ultrapure water or liquid scintillator provides an alternative to this. These materials can not only act as passive shield against the external radiation, but also as active veto detectors for cosmic muons and muon induced particles. Experiments that employ this type of shielding includes XENON1T, LUX-ZEPLIN, Borexino, PandaX, EXO etc.

- **Particle discrimination and tracking:** The signature of the event of interest often has a unique spatial or time profile in the case of many experiments. The GERDA experiment uses the difference in the energy deposition of single and multi-sited events for the discrimination between the $0\nu\beta\beta$ and the background events [30]. While the former has point like energy deposition, the latter has energy deposition at multiple locations. This provides a powerful discrimination strategy against various radioactive backgrounds. In the case of experiments employing LXe dual phase TPCs, two signals from the liquid and the gaseous phase of the detector is used for the reconstruction of the energy, position and the recoil type. The characteristics of these signals provides the capability to reject various kinds of background [35, 47, 48]. In the case of SuperNEMO detector, a thin layer of $\beta\beta$-emitting isotope sandwiched between trackers and surrounded by calorimetry for the three-dimensional reconstruction of charged particle tracks, as well as energy measurements [49].

1.2 Experimental search for rare events

This section describes the physics motivation for various rare event searches with emphasis on neutrinoless double beta decay. The discovery of neutrinos,

the motivation for neutrino mass from the observation of neutrino oscillations, neutrinoless double beta decay and associated experiments and direct dark matter searches are described.

1.2.1 Neutrino interactions

The radioactive decay of Uranium was discovered by Henri Becquerel in 1896, marking the beginning of the study of weak interactions. The α and γ rays from the radioactive decay were found to have unique energy, while the energy spectrum of β rays was found to be continuous. This would either lead to non-conservation of energy, momentum and angular momentum in the nuclear β decay or would require the existence of a new particle. In order to remedy this situation, the existence of neutrino was proposed by W. Pauli in 1930, as weakly interacting neutral fermion that accounts for the missing energy and angular momentum [1]. Following this, Enrico Fermi formulated the theory of β decay in 1934. The direct experimental detection of neutrinos happened in 1956, by Clyde L. Cowan and Frederick Reines in a nuclear reactor based experiment [2]. In the year 1958, the helicity of neutrino was determined to be -1 (+1 for antineutrino) by Goldhaber et al. [50].

Neutrinos were initially assumed to be massless fermions, before the neutrino oscillations were discovered. In the year 1956, Davis et al. [51] experimentally confirmed the deficit of solar neutrinos, compared to the predictions by Bahcall et al. [52]. This provided the first evidence of neutrino oscillations. In the following years, various experiments observed oscillations in atmospheric [53], solar [54–59], reactor [60–62], and accelerator [63, 64] neutrinos, providing compelling evidence of non-zero neutrino mass. This was also the first evidence

of the physics beyond the standard model.

Neutrino Oscillations

Oscillations of neutrinos are a consequence of the presence of flavour neutrino mixing, or lepton mixing between the flavour and the mass eigen states of neutrinos. The eigen states of the weak interaction or the flavour eigen states (ν_e, ν_μ and ν_τ) are connected to the mass eigen states by a Unitary matrix U, called Pontecorvo-Maki-Nakagawa-Sakata (PMNS) mixing matrix [65] as:

$$\nu_l(x) = \Sigma_j U_{lj} \nu_j(x) \qquad l = e, \mu, \tau \tag{1.1}$$

In the three neutrino framework, the matrix U can be parametrized by three mixing angles and one or three CP violating phases depending on whether the neutrinos are Dirac or Majorana particles. The mixing matrix takes the form:

U=

$$\begin{bmatrix} c_{12}c_{13} & s_{12}c_{13} & s_{13}e^{-i\delta} \\ -s_{12}c_{23} - c_{12}s_{23}s_{13}e^{i\delta} & c_{12}c_{23} - s_{12}s_{23}s_{13}e^{i\delta} & s_{23}c_{13} \\ s_{12}s_{23} - c_{12}c_{23}s_{13}e^{i\delta} & -c_{12}s_{23} - s_{12}c_{23}s_{13}e^{i\delta} & c_{23}c_{13} \end{bmatrix}$$

$$\times \text{diag}(1, e^{i\frac{\alpha_{21}}{2}}, e^{i\frac{\alpha_{31}}{2}})$$

where $s_{ij} = sin(\theta_{ij})$ and $c_{ij} = cos(\theta_{ij})$, δ is the Dirac CP violation phase and α_{21} and α_{31} are the two Majorana CP violation phases.

The flavour transition probability in neutrino oscillations depends on the neutrino energy E, the distance travelled by the neutrino from the point of production to the point of detection, the elements of the PMNS mixing matrix and on the

mass squared difference $\Delta m_{ij}^2 = m_i^2 - m_j^2$. The probability of flavour transition from $|\nu_l\rangle$ to $|\nu_m\rangle$, $P_{lm} = |\langle \nu_m | \nu_l(t) \rangle|^2$, can be written as:

$$
\begin{aligned}
P_{lm} = \delta_{lm} &- 4 \sum_{i>j} Re(U_{li}^* U_{mj}^* U_{mi} U_{lj}) \, sin^2 \left(\frac{(m_i^2 - m_j^2)L}{4E} \right) \\
&+ 2 \sum_{i>j} Im(U_{li}^* U_{mj}^* U_{mi} U_{lj}) \, sin^2 \left(\frac{(m_i^2 - m_j^2)L}{4E} \right)
\end{aligned}
\tag{1.2}
$$

The current neutrino oscillation data has been fitted well in terms of two mass squared differences namely, the solar mass splitting, ($\Delta m_{21}^2 = 7.6 \times 10^{-5} eV^2$) and the atmospheric mass splitting ($|\Delta m_{31}|^2 = 2.5 \times 10^{-3} eV^2$). In the case of solar mass splitting, due to the presence of matter effects in the sun, it is known that $\Delta m_{21}^2 > 0^2$ which constrains the product $\Delta m_{21}^2 cos(2\theta_{12})$ to be positive. In the case of atmospheric mass splitting, the oscillations are measured only in the vacuum, the sign of Δm_{31}^2 is yet unknown. As a result of this, there are two possible orderings for the neutrino masses: normal ordering (NO) where ($m_1 < m_2 \ll m_3$) and $\Delta m_{31}^2 > 0$ and inverted ordering (IO) where ($m_3 \ll m_1 < m_2$) and $\Delta m_{31}^2 < 0$. In the case of Quasi degenerate neutrino masses, $m_1 \simeq m_2 \simeq m_3 \gg \Delta m_{ij}^2$.
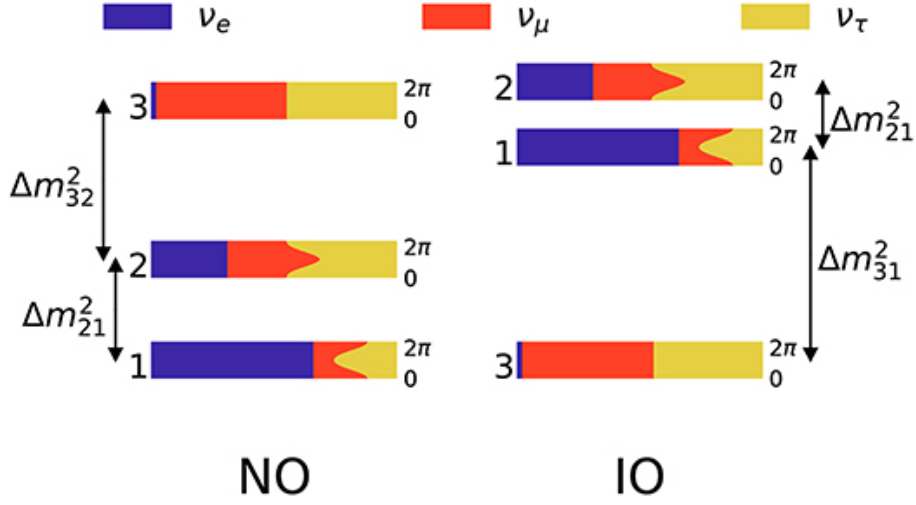
FIGURE 1.2: A schematic of neutrino flavour mixing in the normal and the inverted mass ordering. Figure adapted from [25]

The fit on the neutrino oscillation parameters determined from the latest global analysis is listed in Table 1.

TABLE 1.1: Neutrino oscillation parameters from the global analysis [25]

Parameter	Best-fit $\pm 1\sigma$	2σ range	3σ range
$\Delta m_{21}^2 [10^{-5} eV^2]$	$7.55^{+0.20}_{-0.16}$	7.20-7.94	7.05-8.14
$\|\Delta m_{31}\|^2 [10^{-3} eV^2]$ (NO)	2.5 ± 0.03	2.44-2.57	2.41-2.60
$\|\Delta m_{31}\|^2 [10^{-3} eV^2]$ (IO)	$2.42^{+0.03}_{-0.04}$	2.34-2.47	2.31-2.51
$sin^2(\theta_{12})/10^{-1}$	$3.12^{+0.20}_{-0.16}$	2.89-3.59	2.73-3.79
$sin^2(\theta_{23})/10^{-1}$ (NO)	$5.47^{+0.20}_{-0.30}$	4.67-5.83	4.45-5.99
$sin^2(\theta_{23})/10^{-1}$ (IO)	$5.51^{+0.18}_{-0.30}$	4.91-5.84	4.53-5.98
$sin^2(\theta_{13})/10^{-2}$ (NO)	$5.47^{+0.20}_{-0.30}$	4.67-5.83	4.45-5.99
$sin^2(\theta_{13}) 10^{-2}$ (IO)	$2.160^{+0.083}_{-0.069}$	2.03-2.34	1.96-2.41
δ_{CP}/π (NO)	$1.32^{+0.21}_{-0.15}$	1.01-1.75	0.87-1.94
δ_{CP}/π (IO)	$1.56^{+0.13}_{-0.15}$	1.27-1.82	1.12-1.94

The neutrino flavour transition amplitude, as written in Eq. (1.2), depends only the mass square differences Δm_{ij}^2, the mixing angles $\theta_{12}, \theta_{23}, \theta_{13}$ and the Dirac CP violation phase δ. It does not depend on the Majorana phases or the nature of the neutrino. The knowledge of the nature of neutrinos with definite

masses (Majorana or Dirac) is extremely important for the understanding of the origin of small neutrino masses, which necessitates the study $0\nu\beta\beta$ in different nuclei.

1.2.2 Neutrinoless double beta decay

Double beta decay ($2\nu\beta\beta$) is an isobaric transition from a parent nucleus (A,Z) to a daughter nucleus (A,Z + 2), along with the emission of two electrons and two electron type antineutrinos. It is a second order weak nuclear interaction process introduced by Goeppert-Mayer in 1935 [4] and studied by Furry in 1939 [66]. The nuclear transformation in double beta decay process can be written as:

$$(A, Z) \rightarrow (A, Z + 2) + 2e^- + 2\bar{\nu}_e \tag{1.3}$$

The typical half life of $2\nu\beta\beta$ process is $> 10^{19}$ y. It was was first deduced in a radiochemical experiment in 1950, and subsequently observed in real time in fourteen nuclei (including $2\nu\beta\beta$ and $2\nu ECEC$ process) since the first laboratory measurement [67].

Majorana proposed the possibility of a single quantum field for neutral fermions, that describes the situation in which the particles and antiparticles coincide, as in the case of photons [3]. This allows the possibility for electrically neutral spin 1/2 fermions to be their own antiparticles. In the context of double beta decay process, this would imply that the conclusions of the theory will remain unchanged even if there existed only one type of neutrino, i.e. neutrino and antineutrino is the same particle. In this process, the initial nucleus (A, Z) emits one beta particle and goes into a virtual intermediate nucleus (A, Z + 1) and a virtual neutrino (Racah sequence). The virtual neutrino induces the decay of

this intermediate nucleus with emission of the second beta particle and is itself absorbed. This process known as Neutrinoless double beta decay ($0\nu\beta\beta$) can be written as:

$$(A, Z) \rightarrow (A, Z + 2) + 2e^- \qquad (1.4)$$

Before the discovery of parity violation in the weak interactions by [68, 69], the $T_{1/2}$ of $0\nu\beta\beta$ process was estimated to be much lower than $2\nu\beta\beta$. After the V-A nature of weak interactions was established, it became clear that the $T_{1/2}$ of $0\nu\beta\beta$ would significantly exceed that of $2\nu\beta\beta$, with typical $T_{1/2} > 10^{26}$ y with the explicit violation of the lepton number ($\Delta L = 2$). The discovery $0\nu\beta\beta$ would therefore demonstrate that lepton number is not a symmetry of nature and could reveal the role leptons played in the creation of the matter-antimatter asymmetry in the Universe. It must however be pointed out that, $0\nu\beta\beta$ is possible only if neutrinos are Majorana particles with non-zero mass. Neutrino masses require either the existence of right-handed neutrinos or violation of the lepton number so that Majorana masses are possible. The $0\nu\beta\beta$ process is perhaps the only experimental probe to understand the nature of the neutrinos, i.e. if neutrinos are Dirac or Majorana particles. The experimental searches for $0\nu\beta\beta$ involves large detector masses, high energy resolutions and ultra low backgrounds,in order to achieve unparalleled sensitivities to extremely small effects due to the Majorana neutrino masses. There are around 35 possible candidates in which the occurrence of $0\nu\beta\beta$ decay is possible. The single beta decay process in these cases is either energetically forbidden or spin suppressed. In the case of $0\nu\beta\beta$, the signature is characterized by a peak at the Q-value of the decay, which corresponds to the sum energy of the emitted electrons.
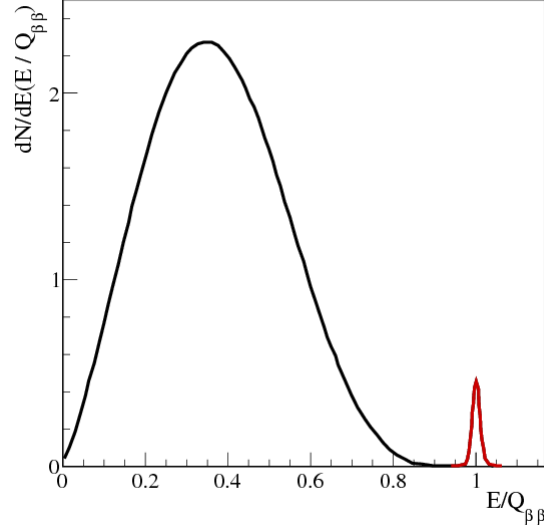
FIGURE 1.3: Representation of the sum energy spectrum of electrons emerging from double beta decay process. The peak indicated in red, indicates the expected peak from $0\nu\beta\beta$ decay. Figure adapted from [70].

The major experimental challenge in the case of rare event searches like $0\nu\beta\beta$ is the suppression of various backgrounds. Given the rarity of the process, with $T_{1/2} > 10^{26}$ y, background reduction plays a pivotal role in driving the next generation tonne scale experiments to achieve the required sensitivity levels. The effective Majorana mass $|m_{\beta\beta}|$ is not a directly measurable quantity. The $T_{1/2}$ of $0\nu\beta\beta$ decay is related to the product of the effective neutrino Majorana mass and the nuclear matrix element by the following relation:

$$\frac{1}{T_{1/2}^{0\nu}} = G_{0\nu}|M_{0\nu}|^2 \frac{|\langle m_{\beta\beta}\rangle|^2}{m_e^2} \tag{1.5}$$

where $G_{0\nu}$, $M_{0\nu}$ and m_e are the phase space factor, nuclear matrix element and electron mass, respectively. The effective neutrino Majorana mass is given by:

$$m_{\beta\beta} = \sum_i U_{ei}^2 m_i \tag{1.6}$$

where U_{ei} are the elements of the PMNS matrix.

The value of $m_{\beta\beta}$ is also sensitive to the neutrino mass ordering, in the case where the lightest neutrino mass is below 40 meV as shown in figure 1.4. If the inverted mass ordering is true, then the value of $m_{\beta\beta}$ has to be larger than 10 meV, while in the case of normal ordering it must be below $\sim$ 7 meV. Thus experiments with sensitivity to probe $m_{\beta\beta}$ < 10 meV can rule out the inverted scenario in the case of non observation of $0\nu\beta\beta$.
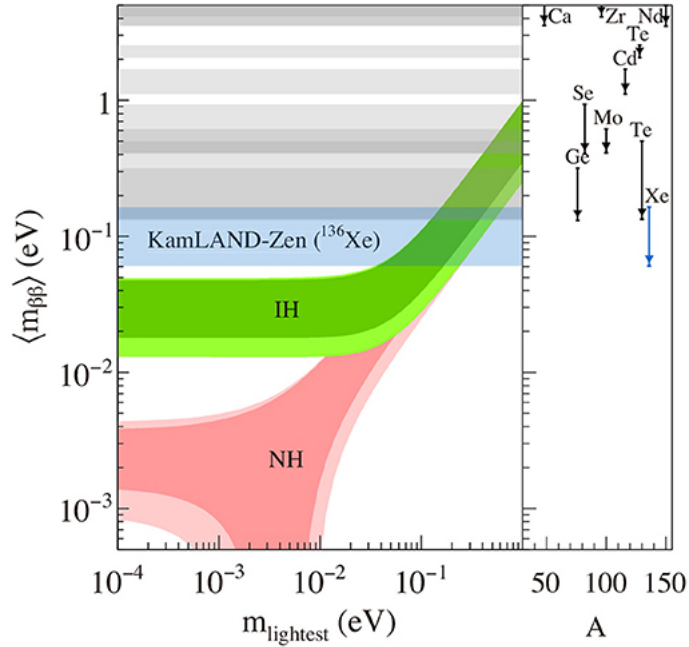
FIGURE 1.4: Predictions on effective Majorana neutrino mass $m_{\beta\beta}$ as a function of the lightest neutrino mass $m_{lightest}$, and the experimental limits from the $0\nu\beta\beta$ decay searches (at 90% C.L.). Figure adapted from [8].

In the case of observation of signal for $0\nu\beta\beta$, the half life $T_{1/2}^{0\nu}$ can be obtained from the relation :

$$T_{1/2}^{0\nu} = ln2\frac{N_A\epsilon Mit}{AN_{obs}} \tag{1.7}$$

where N_A is the Avogadro's number, ϵ is the detection efficiency, i is the

isotopic abundance, M is the detector mass, A is the molar mass, N_{obs} is the number of events attributed to $0\nu\beta\beta$ and t is the duration of measurement. In the case of non-observation, a lower limit on the $T_{1/2}$ of $0\nu\beta\beta$ can be placed as:

$$T_{1/2}^{0\nu} > \frac{N_A i \epsilon}{A f_{CL}} \sqrt{\frac{Mt}{N_{bkg} \Delta E}} \qquad (1.8)$$

where f_{CL} is the number of standard deviations corresponding to a given confidence interval, N_{bkg} is the number of background events per unit energy expressed in $(keV^{-1} kg^{-1} y^{-1})$ and ΔE is the detector resolution. To achieve high sensitivity in double beta decay detection, the following elements are necessary:

- Large detector mass and high isotopic abundance

- High energy resolution is necessary to distinguish the peak arising from $0\nu\beta\beta$ from the continuum background of $2\nu\beta\beta$

- High detection efficiency

- Ultra low levels of background, which is the most important and challenging factor in the case of rare decay experiments

- High $Q_{\beta\beta}$ value. The event rate in the case of $0\nu\beta\beta$ decay is $\propto Q_{\beta\beta}^5$. For $Q_{\beta\beta} > 2.6 MeV$, the region of interest (ROI) is also free from the background due to γ rays from natural radioactivity.

1.2.3 Experimental searches for $0\nu\beta\beta$

The major ongoing experimental efforts in various candidate isotopes for $0\nu\beta\beta$ is briefly discussed here:

- The **KamLAND-Zen** experiment [8] studies $0\nu\beta\beta$ in ^{136}Xe isotope. The main detector consists of enriched Xe (with ^{136}Xe) is dissolved in the liquid scintillator contained in a 1.5 m balloon inside the original KamLAND detector. The volume outside is also filled with scintillator material. This acts as an excellent active shield to the external backgrounds. With an exposure of 504 kg.y, the limit on $T_{1/2}$ has been set to 1.07×10^{26} y (at 90% C.L.). The next upgrade of KamLAND-Zen with 750 kg of ^{136}Xe, aims to reach a sensitivity of $T_{1/2}^{0\nu} \simeq 5 \times 10^{26}$ y.

- The **GERmanium Detector Array (GERDA)** experiment [30] studies ^{76}Ge isotope employing bare Germanuim detectors with 86% enrichment . The detectors are immersed in liquid Ar (LAr) for cooling the Ge crystal and γ ray shielding, supplemented by additional water shield. The current limit on the $T_{1/2}^{0\nu}(^{76}$Ge$)$ from GERDA is 8×10^{25} y (at 90% C.L.). The GERDA and **Majorana demonstrator** [71](also based on ^{76}Ge), will join to work on the LEGEND project (Large Enriched Germanium Experiment for Neutrinoless Double beta decay) [72]. The proposed LEGEND-200 module aims to achieve a sensitivity of $T_{1/2}^{0\nu} \simeq 1 \times 10^{27}$ y, with 200 kg of Germanium and 5 years of exposure. Further, the LEGEND-1000 module aims to achieve $T_{1/2}^{0\nu} \simeq 1 \times 10^{28}$ y with a 1 tonne detector and an exposure time of 10 years, covering the inverted mass ordering region.

- The **Cryogenic Underground Observatory for Rare Events (CUORE)** [73] studies ^{130}Te isotope using cryogenic bolometric detectors made from TeO_2. The experiment is currently running with a tonne scale detector. It is projected to achieve a sensitivity of $T_{1/2}^{0\nu} \simeq 9 \times 10^{25}$ y after 5 years of

data taking.

- The **CUPID (CUORE Upgrade with Particle ID)** [74] is an upgrade to the CUORE experiment. The isotope of interest is ^{82}Se. The experiment plans to make use of particle tracking techniques to achieve a superior background rejection aiming to reach 0.1 count/ton-y. The present run, with the precursor CUPID-0, has already provided the best limit on $T^{0\nu}_{1/2}(^{82}\text{Se})$ as 3.5×10^{24} y (at 90% C.L.) [75]. The target sensitivity is $T^{0\nu}_{1/2} \gtrsim 1 \times 10^{27}$ y.

- The **Enriched Xenon Observatory -200 (EXO-200)** [76] studies $0\nu\beta\beta$ in ^{136}Xe isotope. Ultra pure liquid Xenon (LXe) enriched with ^{136}Xe is used as both the source and the detector. Time Projection Chambers (TPC) are used to detect the ionization electrons. The three dimensional event reconstruction provides excellent rejection against the Compton background in this case. The limit on the $T^{0\nu}_{1/2}$ of is placed as 1.1×10^{25} y (at 90% C.L.). The improved version of the experiment **nEXO** [77],will use 5 tons of liquid Xenon to achieve a sensitivity of $T^{0\nu}_{1/2} \gtrsim 1 \times 10^{28}$ y with 10 y exposure.

- The **Neutrino Experiment with a Xenon TPC (NEXT)** [78], which studies ^{136}Xe isotope, employs gaseous Xenon in a High Pressure Xenon chamber (HPXe). The chamber is maintained at a typical pressure of 15 bar TPC is used for event reconstruction. This technique has many advantages including the possibility of excellent trajectory reconstruction, which improves the background, superior energy resolution and scalability. The

NEXT-100 phase, which plans to employ 100 kg of ^{136}Xe is expected to reach a sensitivity of $T_{1/2}^{0\nu} \gtrsim 1 \times 10^{26}$ y, with five years of data taking.

- The **Neutrino Ettore Majorana Observatory (NEMO-3)** [49] studies $0\nu\beta\beta$ in seven isotopes, with focus on ^{100}Mo (7 kg) [79] and ^{82}Se (1 kg). The current established limits for ^{82}Se is $T_{1/2}^{0\nu} > 2.5 \times 10^{23}$ y (at 90% C.L.). The other isotopes studied in the smaller scale are ^{116}Cd, ^{150}Nd, ^{96}Zr, ^{48}Ca, ^{130}Te. The NEMO employs a thin layer of $\beta\beta$-emitting isotope is sandwiched between trackers and surrounded by calorimeters. This allows full topological reconstruction of the charged particle tracks and energy measurement. The **SuperNEMO** experiment, which is the successor of NEMO-3, is under construction.

- The **SNO+** experiment [80] plans to employ 1% of ^{130}Te by weight in 760 ton of ultra pure liquid scintillator to achieve an ultimate sensitivity of $T_{1/2}^{0\nu} \gtrsim 1 \times 10^{27}$ y.

The other experimental efforts include **CANDLES** experiment [81] that employs scintillating CaF_2 crystals to study ^{48}Ca isotope, **AMoRE** [82] designed to measure the lifetime of ^{100}Mo , **COBRA** [83] experiment employing CdZnTe crystals, **Aurora** experiment [84] that employs enriched ^{116}CdWO$_4$ crystal scintillators to study $0\nu\beta\beta$ in ^{116}Cd. The recent exprimental effort to study the two-neutrino electron capture with positron emission in ^{106}Cd [85] has achieved a half life limit of 4×10^{21} y (at 90% C.L.), which is the best limit currently achieved for this isotope.

TABLE 1.2: The best achieved limits for $T_{1/2}$ and m_ν in major $0\nu\beta\beta$ experiments (at 90% C.L.)

Experiment	Isotope	Q-value (MeV)	Limit on $T^{0\nu}_{1/2}$ (y)	N_{bkg} $(keV^{-1}kg^{-1}y^{-1})$	m_ν (meV)
CUPID-0	^{82}Se	2.955	2.4×10^{24}	3.6×10^{-3}	376-770
CUORE	^{130}Te	2.530	1.5×10^{25}	1.4×10^{-2}	110-520
GERDA	^{76}Ge	2.039	8.0×10^{25}	0.7×10^{-3}	150-330
KamLAND-Zen	^{136}Xe	2.458	1.07×10^{26}	1.5×10^{-4}	61-165

1.2.4 Dark matter interactions

The matter in the universe as we know today, accounts for only 5% of the observed gravitational effects. Various observations from cosmological and astrophysical sources such as the rotation curve of galaxies, gravitational lensing, cosmic microwave background (CMB) radiation etc. confirms that majority of the universe is made of substance that is not the ordinary matter. The prominent candidates that are hypothesized to constitute the dark matter includes Weakly Interacting massive Particles or WIMPs, sterile neutrinos, axions and supersymmetric particles. Though the standard model neutrinos do satisfy the conditions to be a candidate for dark matter, their masses are too tiny and can supply only a small fraction of the observed dark matter. Hence the nature of dark matter is not yet conclusively known and remains a question of fundamental importance. To increase the discovery potential for dark matter, it is necessary to have independent detector technologies and varieties of targets, spread across various geographical locations. Experiments that search for dark matter can either be direct in which the nuclear recoil resulting from the scattering of the dark matter particle off the detector nucleus constitutes the event signature or indirect search which looks for the annihilation of dark matter particles to standard model

particles or vice versa. In the case of direct dark matter searches, background reduction is extremely important and most of these experiments are located deep underground. Neutrons are particularly important as a source of background, since the scattering of the neutrons off the nucleus mimics the signature produced by the scattering of the WIMP. The table 1.3 summarizes the details of major direct dark matter experiments.

TABLE 1.3: The major experimental efforts involved in the direct dark matter search. The detectors used, the achieved limits on the spin-dependent WIMP cross section (σ_{SI} at 90% C.L.), the achieved background levels (N_{bkg}) and the shielding configurations employed are discussed.

Experiment	Detector	Limit on $\sigma_{SI}(cm^2)$	N_{bkg} $(keV^{-1}kg^{-1}y^{-1})$	Shielding configuration
CDMS/SuperCDMS [45]	Ge and Si	5.4×10^{-42} at 5 GeV	$\sim 4 \times 10^2$	Cu (3 cm), Pb (22.5 cm), polyethylene (40 cm), plastic scintillator (μ-veto)
LUX-ZEPLIN (LZ) [86]	LXe (dual phase) TPC	1.4×10^{-48} at 40 GeV (projected)	$\sim 4 \times 10^{-4}$	LXe, Gd-loaded liquid scintillator, water shield
XENON1T [35]	LXe (dual phase) TPC	4.1×10^{-47} at 30 GeV	$\sim 9 \times 10^{-3}$	Water Cherenkov (μ-veto+passive shield)
CRESST[46]	CaWO$_4$	$\sim 1 \times 10^{-24}$ <1 GeV	$\sim 10^3$	Cu (14 cm), Pb (20 cm) polyethylene (50 cm), LN$_2$ purging, μ-veto
PandaX [87]	LXe (dual phase) TPC	8.6×10^{-47} at 40 GeV	$\sim 3 \times 10^{-1}$	ultrapure water
Darkside-50 [36]	LAr (dual phase) TPC	1.14×10^{-44} at 100 GeV	$\sim 1 \times 10^{-3}$	5% Boron loaded liquid scintillator, water Cherenkov
DEAP-3600 [88]	LAr (single phase) TPC	3.9×10^{-45} at 100 GeV	$\sim 3 \times 10^{-4}$	Water Cherenkov (μ-veto+passive shield)

Another important dark matter experiment is the **DAMA/LIBRA** [89, 90], which aims to investigate the presence of dark matter particles in the galactic halo by exploiting the model independent dark matter annual modulation signature. The experiment employs highly radio-pure NaI(Tl) detectors sensitive to wide range of dark matter candidates, interaction types and astrophysical scenarios [91]. The combined analysis on the Phase1 [92] and Phase2 [93] data of the DAMA/LIBRA gives a modulation amplitude of 0.0096±0.0008 cpd/kg/keV and

a phase of 145±5 days which are well in agreement with the expected value for the dark matter particles. However, the results from the other experiments with similar sensitivity but different detection techniques are not consistent with DAMA's results. In view of this, new experiments such as **ANAIS (annual modulation with NaI scintillators)** [94], **COSINE-100** [95], **DM-Ice17** [96], **SABRE (Sodium-iodide with Active Background REjection)** [97] have been set up to perform model independent test of DAMA's observation using the same detector material. Some of these experiments are expected to attain 3σ coverage of DAMA region with five years of data taking.

The next generation direct dark matter detection experiments such as LZ, PandaX-4T, XENONnT would ultimately reach sensitivities enough to hit the neutrino floor, where the coherent neutrino nucleus scattering would become the dominant background.

1.2.5 Other rare event measurements

Nuclear astrophysics experiments aims at determining the nuclear properties and reaction rates that impact our understanding of how the stars work and evolve. The understanding of nucleosynthesis of elements requires the measurements of typically sub pico-barn cross sections. This requires low energy accelerators, stable beams, materials of high radiopurity and low background levels. Collaborations such as LUNA [98] (The Laboratory for Underground Nuclear Astrophysics) at Gran Sasso underground laboratory and CASPER (Compact Accelerator System for Performing Astrophysical Research) located at Sanford Underground Research Facility aims to measure cross sections and reaction rates of consequence to the stellar nucleosynthesis.

The α and β decay of certain isotopes are also extremely rare in nature. These processes are important to understand various aspects pertaining to the properties of atomic nuclei. The requirements of low background and radiopurity are similar to other low background experiments. Several decays of long half life like α decay of ^{151}Eu, ($T_{1/2} \sim 5 \times 10^{18}$ y) and ^{180}W, ($T_{1/2} \sim 1 \times 10^{18}$ y), both to the ground state of daughter nucleus, have been measured recently, after the improvement in the low background experimental techniques and underground facilities became available [99].

1.3   The TIN.TIN experiment

A feasibility study to search for $0\nu\beta\beta$ in ^{124}Sn based on cryogenic particle detector has been initiated in India [9]. The TIN.TIN (The INdia-based TIN detector) experiment will be housed in the underground facility, coming up at Bodi West Hills (BWH) in Madurai, at the proposed India based Neutrino Observatory (INO) [100]. The experiment will have an overburden of $\sim$ 1000 m of rock. The ^{124}Sn isotope has moderate isotopic abundance 5.8% and a reasonably high Q value of 2.2911±0.0015 MeV [10]. The $2\nu\beta\beta$ process has not yet been observed directly by the experiments. The lower limit on the $T_{1/2}$ of $2\nu\beta\beta$ in ^{124}Sn is currently in the range of (0.8 to 1.2) $\times 10^{21}$ y, at 90% C.L [101, 102]. The cryogenic bolometers with excellent energy resolution and high sensitivity, are well suited for rare event studies like NDBD or dark matter search. For this purpose, a custom-built cryogen-free dilution refrigerator, having a large cooling power of 1.4 mW at 120 mK, has been installed at TIFR, India [103]. The dilution refrigerator can support a total mass of 100 kg, including the Sn detector and 5 cm low activity Pb. Tin becomes superconducting below 3.7 K and at T<100 mK its

specific heat has only lattice contributions and can be used to make a bolometric detector. Very small size Sn bolometers have been found to give the best energy resolution at sub-kelvin temperature. It is envisaged that the prototype stage of TIN.TIN would consist of an array of ~30 Tin crystals (natural/enriched ~ $3 \times 3 \times 3$ cm^3 each) arranged in a tower geometry with corresponding read-out sensors. Neutron transmutation doped (NTD) sensors are developed indigenously, for this purpose [104, 105]. A dedicated low background HPGe-based setup, TiLES [14], is also operational at TIFR for material characterization and low background studies for TIN.TIN.

The background reduction plays a pivotol role in TIN.TIN, like all the other experiments that are designed to look for rare events. The most important contribution to the background will arise from the radioactive impurities present in the Tin crystal and other materials in the viscinity of the detector such as the components of the cryostat, sensors and readout wires. Though the cosmic muon flux will be reduced by orders of magnitude at the underground laboratory site, there will be a non-negligible contribution to the background via direct energy deposition, production of radioactive isotopes in the detector and surrounding materials, and via the production of secondary particles upon interacting with high Z materials. The neutrons that are produced from the spontaneous fission and (α, n) reactions from the natural radioactivity present in the rock and surrounding materials, also contribute to the background. These neutrons can excite the nucleas by capture or scattering reactions, contributing to electron and γ ray background in the detector fiducial volume. The experimental setup of TIN.TIN is envisaged to be similar to that of the CUORE experiment [73], consisting of an array of Tin bolometric detectors. A combination of active and passive shields

along with particle discrimination techniques will be implemented in the final experiment to discriminate against the background events.

This thesis is focussed on the understanding of different aspects and impact of neutron background for $0\nu\beta\beta$ in ^{124}Sn. The possibility of using borated rubber as a neutron shield in rare decay experiments is assessed. The attenuation of thermal neutrons in the borated rubber is studied as a function of Boron concentration using fast neutrons from ^{241}Am-^{9}Be and ^{252}Cf fast neutron sources. The thermalization of neutrons are also studied in plain HDPE. The thickness of the HDPE has been optimized for the simultaneous detection of thermal neutrons and γ rays originating from the neutron capture in Hydrogen. Fast neutron activation studies of borated rubber, borated HDPE, and plain HDPE are carried out to understand and the presence of any dissolved impurities, which have been identified by the presence of the characteristic γ rays resulting from the neutron activation.

The secondary neutron production from cosmic muons has been assessed with two independent measurements which involves direct and indirect experimental detection of cosmic muon induced neutrons. The contribution to secondary neutron production from stopping and non stopping muons is assessed from MINT (Muon Induced Neutron measurement setup at TIFR) which involves the direct detection of neutrons which are produced from cosmic muon induced reactions. MINT consists of novel, high efficiency thermal neutron detectors, CLYC and NaIL. The detectors are surrounded by 10 cm HDPE for the thermalization of cosmic muon induced neutrons. Preliminary measurements have been carried out at the sea level to understand the neutron production in Pb. An estimation of the contribution from stopping muons to the secondary neutron production is

also obtained for Fe and Pb targets. Independently, the γ ray background arising from cosmic muon induced fast neutrons has been measured in the TiLES low background HPGe set up. The fast neutrons undergo $(n, n'\gamma)$ reactions in Ge detector and Cu shield to produce characteristic γ rays. Monte Carlo simulations have also been performed to understand the cosmic muon induced neutron background in the TiLES setup. Finally, the γ background arising from thermal neutron capture reactions in ^{124}Sn has been studied by thermal neutron irradiation of enriched ^{124}Sn sample. The contribution of thermal neutron induced γ ray background to the region of interest for $Q_{\beta\beta}$ in ^{124}Sn is estimated from the observed activity in the irradiated ^{124}Sn sample.

Neutron absorption studies

Introduction

This chapter describes the characterization of materials for neutron shielding properties. As discussed in Chapter 1, neutrons constitute an important source of background for rare event experiments. Neutron spectroscopy is in general, difficult compared to γ ray detection because of their weak interaction with matter and their large dynamic range in energy. Fast neutrons are generally detected with materials rich in hydrogen via neutron inelastic scattering reactions. For thermal neutron detection, detectors loaded with materials of high neutron capture cross section like ^{6}Li, are used. In this chapter, the description of the CLYC and NaIL detectors, which are novel class of scintillator detectors, with dual detection capability for neutrons and gamma rays, is presented. The properties of these detectors are briefly described, with the measurements conducted using γ ray and neutron sources. The thermalization of neutrons in high density polyethylene (HDPE) is studied using ^{249}Am-^{9}Be and ^{252}Cf neutron sources, which is described in the Section 2.2. The thickness of the HDPE is optimized

for the simultaneous detection of both thermal neutron and γ rays from the neutron capture. The possibility of using Boron loaded rubber as a passive neutron shield is assessed. The thermal neutron attenuation properties of Boron loaded rubber is studied for varying Boron concentrations, as described in Section 2.3. The fast neutron activation studies, to assess the presence of dissolved impurities, in borated rubber, borated HDPE and non borated HDPE are presented in the Section 2.4. The impurities in the samples are identified from the characteristic γ ray energies and tracking of the respective half lives. The suitability of these materials in low background applications is evaluated from the observed γ ray activity from the fast neutron activation.

2.1   Thermal neutron detectors

The detectors with neutron/gamma dual detection capability has garnered great interest in the recent days. The most important characteristics for neutron detection is high neutron detection efficiency and good discrimination capability against the γ ray background. The CLYC and NaIL detectors are new class of detectors with these desired characteristics. These detectors have wide applications including radiation safety, nuclear material detection, fundamental research and so on. The characteristics of CLYC and NaIL detector is described here.

2.1.1   The CLYC detector

The CLYC ($Cs_2LiYCl_6 : Ce$) detector is a novel class of particle detector, that belongs to elapsolite crystal family which combines the properties of γ ray detectors with moderate resolution and ^{3}He neutron detectors. It is suitable for a wide range of applications involving high energy neutrons (1-10 MeV), thermal neutrons and γ rays. Thermal neutrons are detected via capture reaction ^{6}Li(n, α)

^{3}H, which produces a unique signal with ~3.2 MeVee light output [106]. The presence of ^{35}Cl in CLYC detector enables the measurement of fast neutrons through the reaction ^{35}Cl(n,p)^{35}S [107]. The light yield of CLYC detector for γ ray and thermal neutron excitation is ~20000 photons/MeV and ~ 70500/neutron, respectively [108]. Due to high light output, the energy resolution of CLYC detector is ~ 4% at 662 keV, which is better than the commonly used scintillators such as BaF$_2$ and NaI. Further, the CLYC detector output signal has an ultrafast scintillation decay component ($\sim$ 2 ns) only for γ-ray induced interactions, which enables n-γ separation through the pulse shape discrimination (PSD). The PSD parameter, is defined by (Q$_L$-Q$_S$/Q$_L$) where Q$_L$ and Q$_S$ represents the long and short gates for the charge integration. The CLYC detector, with its moderate energy resolution and high neutron capture efficiency, is ideally suited for the simultaneous measurement of neutrons and γ rays.

For the present measurements, cylindrical CLYC detector of 1″ × 1″ dimensions, procured from M/S Scionix, is used (shown in the Figure 2.1). The detector was coupled to a 2″ Hamamatsu R13089 photo multiplier tube (PMT), which was operated between -850 to -900 V. Pulse height of ~ 30 mV is obtained at 661 keV. The energy vs PSD spectra with ^{249}Am-^{9}Be source are shown in Figure

FIGURE 2.1: The CLYC detector used in the measurements.

2.2. The top and bottom panels show the spectra for configurations without and with HDPE (10 cm) absorbers between the source and detector. Neutron events

are indicated by rectangular box in both panels. A clear n-γ separation is evident

from Figure 2.2. The fast neutrons with varying energy are seen scattered within

the band while the thermal neutron capture results in an intense peak. It can

be seen that with 10 cm HDPE brick, most of the neutrons are thermalized and

only a narrow peak is visible in the neutron band in the bottom panel of Figure

2.2. The energy spectra for different sources are shown in Figure 2.3. Energy

resolution of the detector was measured and found to be $\sim 5\%$ at 662 keV. In the

bottom panel of Figure 2.3, taken with ^{249}Am-^{9}Be and 10 cm HDPE, a peak at

~ 2.2 MeV arising due to thermal neutron capture in HDPE is also visible.
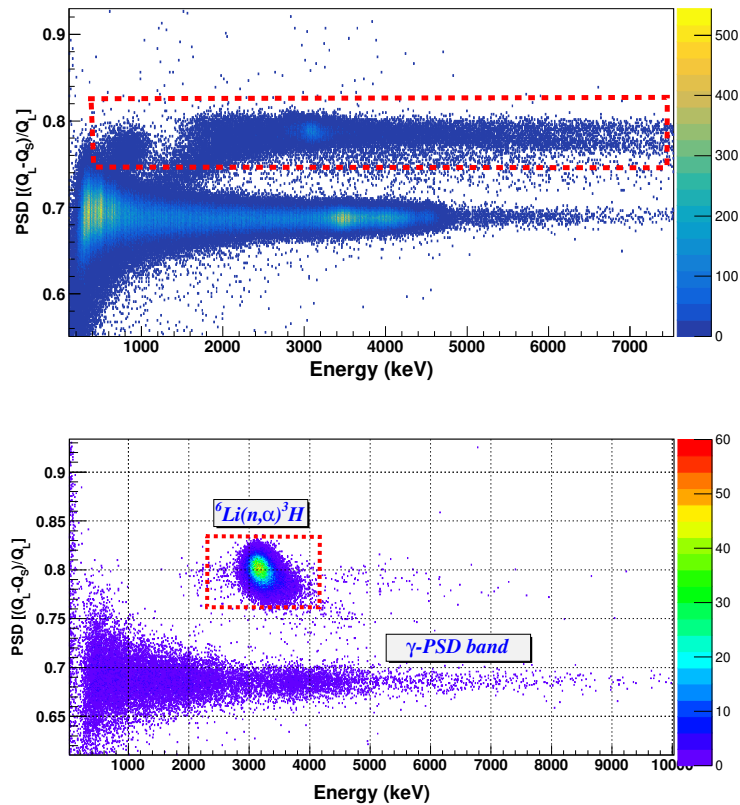
FIGURE 2.2: The energy-PSD spectrum of CLYC detector for fast (top panel) and thermal (bottom panel) neutron detection. The thermal neutron spectrum is taken with 10 cm of HDPE. Neutron PSD band is indicated in red.
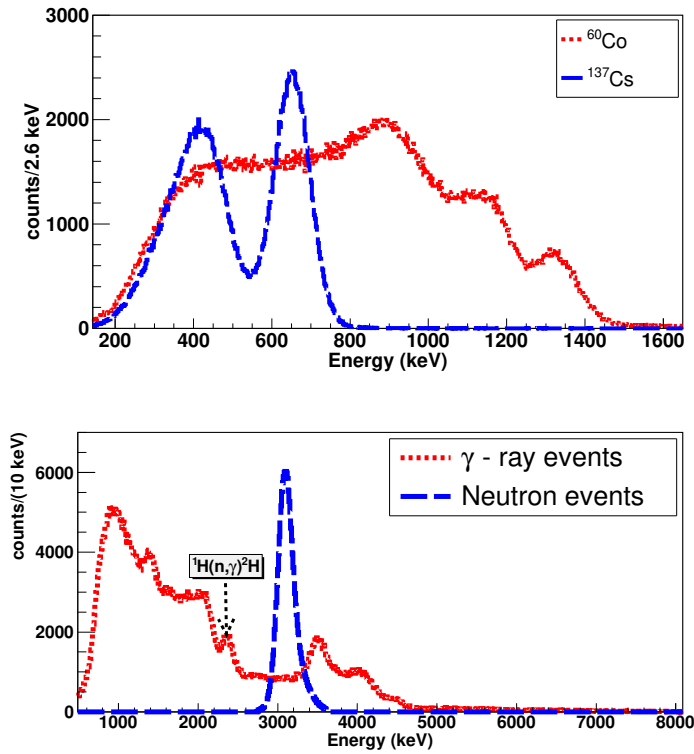
FIGURE 2.3: The energy spectrum of CLYC detector using ^{137}Cs and ^{60}Co source (top panel) and ^{249}Am-^{9}Be source with 10 cm HDPE (bottom panel)

2.1.2 The NaIL detector

The ^{6}Li co-doped NaI crystal, is an attractive detector for neutron/gamma dual detection. The introduction of ^{6}Li enables efficient thermal neutron detection while retaining the favourable scintillation properties of the standard NaI material. The NaIL detectors also have additional advantage over the elapsolite based detectors like CLYC or CLLB in terms of the large possible crystal size. Thermal neutrons are detected via capture reaction ^{6}Li$(n, \alpha)^3$H, which produces a unique signal with ~3.2 MeVee light output, similar to the CLYC detector. The light yield of the NaIL detector is ~ 34000 photons/MeV. In this case also, the identification of neutron and γ ray events is based on pulse shape discrimination, which exploits

the difference in the decay time of the pulses generated from the neutrons and the γ rays. In the case of NaIL detector, neutron pulses decay faster than the γ ray pulses.

For the present measurements, cylindrical NaIL detector of $2'' \times 4''$ dimensions, procured from Saint-Gobain, is used (shown in Figure 2.4). The detector is coupled to a $2''$ Hamamatsu R6231-21 photo multiplier tube (PMT), which was operated between +800 to +850 V. The energy vs PSD spectra with ^{249}Am-
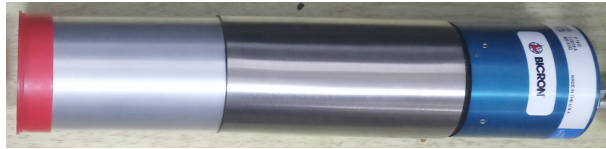
FIGURE 2.4: The NaIL detector used in the measurements.

^{9}Be source, taken with 10 cm of HDPE, are shown in Figure 2.5. An excellent separation between the thermal neutrons and γ ray events is evident. The γ rays originating from ^{1}H$(n, \gamma)^2$H is also clearly visible at 2.2 MeV. The presence of multiple and efficient channels of thermal neutron detection makes the NaIL detector a desirable option for detecting neutrons from cosmic muon induced reactions. The energy resolution of the detector was measured and found to be $\sim$ 7% at 662 keV. However, NaIL detectors are not sensitive to fast neutrons. Figure 2.6, shows the spectra of NaIL detector using ^{137}Cs and ^{60}Co sources (top panel) and ^{249}Am-^{9}Be with 10 cm HDPE (bottom panel). The peak at $\sim$ 2.2 MeV arising due to thermal neutron capture in HDPE is clearly visible.

All the spectra shown are acquired with V1730B digitizer (shown in Figure 2.7) (16 channel, 14 bit ADC, 500 MS/s, 2 V$_{pp}$), with digiTES-4.3.3 data acquisition software. This digitizer has an in-built constant fraction discrimination (CFD) algorithm and gives the time stamp, PSD and energy information. The
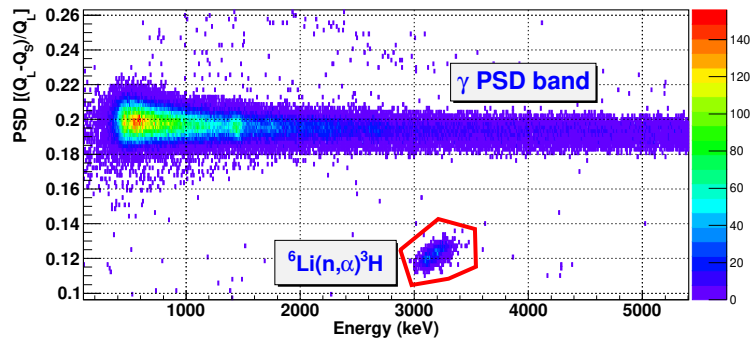
FIGURE 2.5: The energy-PSD spectrum of NaIL detector thermal neutron detection.
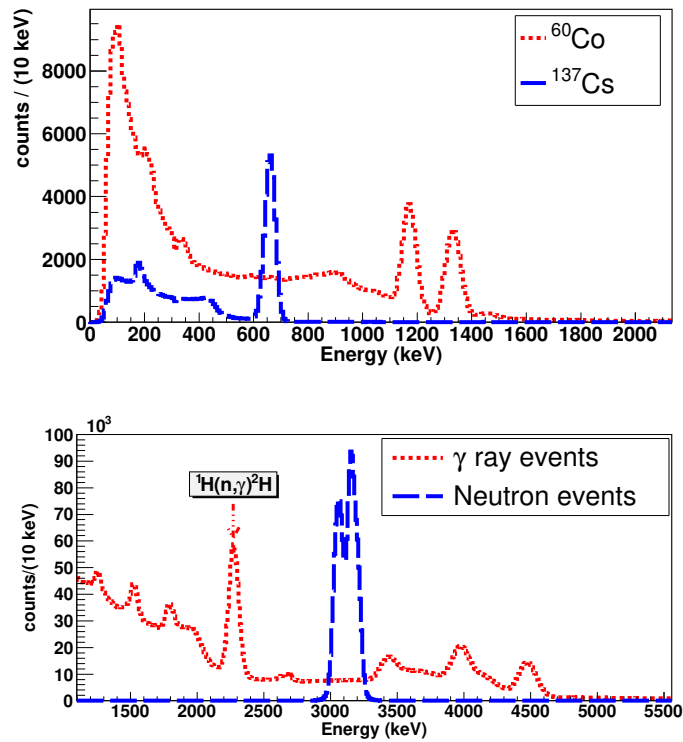
FIGURE 2.6: The energy spectrum of NaIL detector using ^{137}Cs and ^{60}Co source (top panel) and [249]Am-[9]Be source with 10 cm HDPE (bottom panel)

digital parameters for the neutron detectors are also optimized for obtaining the best PSD resolution. The anode output of the detectors were integrated in two

different gates, namely Q_S (short gate) and Q_L (long gate) for n-γ discrimination using PSD technique and energy measurement, respectively. The optimized digital data acquisition parameters are listed below:

Parameter	CLYC	NaIL
Long gate width in ns(Q_L)	1000	2000
Short gate width in ns(Q_S)	300	800
Pre-gate in ns	150	400
CFD delay in ns	30	10
CFD fraction	50%	50%
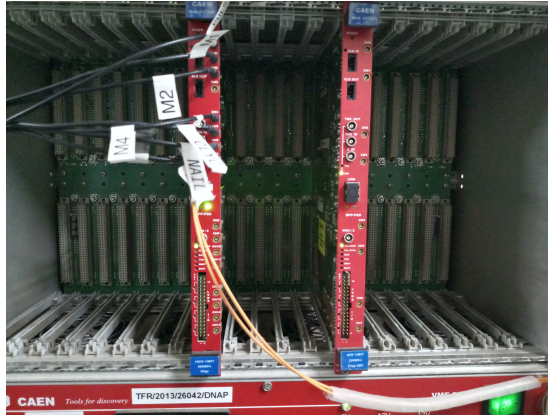
FIGURE 2.7: The V1730B digitizer used for data acquisition

2.1.3   Efficiency of CLYC and NaIL detectors

Monte Carlo simulations were performed with GEANT4 toolkit [16, 17] to estimate the thermal neutron detection efficiency of these neutron detectors. A beam of thermal neutrons are made incident on the NaIL/CLYC detector as shown in Figure 2.8. For NaIL detector, the concentration of ^{6}Li is 1% by weight is considered, as per the manufacturer specifications. For the CLYC detector, the chemical composition of the crystal is considered. A total of of 10^6 thermal neutrons were generated in a beam, from a plane parallel to the lateral face
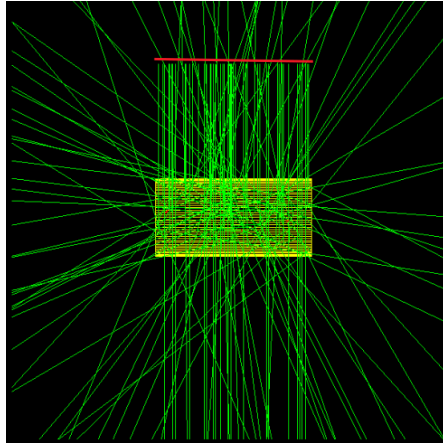
FIGURE 2.8: The geometry of the CLYC/NaIL detector with the planar thermal neutron source, used to determine the intrinsic thermal neutron detection efficiency. The generation plane of thermal neutrons is indicated in red.

of the detector, such that all the generated neutrons fall on the detector face. The detected thermal neutrons are characterized by a peak at 4.78 MeV, at the Q-value of the $^6\text{Li}(n, \alpha)^3\text{H}$ reaction. It may be noted that the light output for the reactions is not incorporated in the simulations. The simulated spectrum of thermal neutron detection in NaIL detector is shown in Figure 2.9. The peak arising from the neutron capture reaction in ^6Li is marked by the dotted lines. The efficiency in the simulations is defined by the number of observed counts in the thermal neutron capture peak to the total number of incident neutrons. Intrinsic thermal neutron efficiency of $\sim$ 53%. and $\sim$25% is obtained for the NaIL and CLYC detectors, respectively.
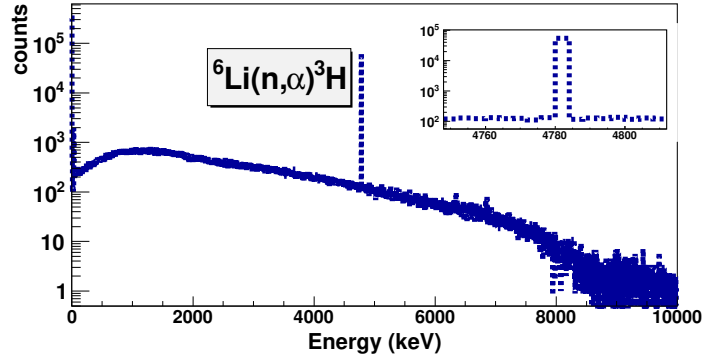
FIGURE 2.9: The simulated spectrum of thermal neutron detection in the NaIL detector. The peak arising from the thermal neutron capture is shown in the inset.

2.2   Neutron thermalization in HDPE

Materials such as water, paraffin, high density polyethylene (HDPE) etc., which are rich in hydrogen are traditionally used for the slowing down of fast neutrons. The extent of fast neutron flux attenuation depends on the incident neutron energy as well as the thickness of the moderator. The thermalized neutrons can also undergo capture reaction in hydrogen to produce γ rays of energy 2.2 MeV. To design a setup for the detection of neutrons produced by cosmic ray muons, after thermalization, it is important to understand the absorption of thermal neutrons in the absorber material. With this motivation, the attenuation of neutrons in the HDPE is studied using ^{249}Am-^{9}Be ($\sim$20000 neutrons/s) and ^{252}Cf ($\sim$3500 neutrons/s) neutron sources. The arrangement of the source and the detectors is shown in the Figure 2.10. The CLYC detector was used for the detection of neutrons after thermalization. For the detection of γ rays from ^{1}H(n, γ)^{2}H reaction, BGO detector is employed. The yield of the thermal neutrons and the γ rays for varying moderator thickness is shown below. From the Figures 2.11, it can be seen that the thermal neutron counts reduce with the increasing thickness
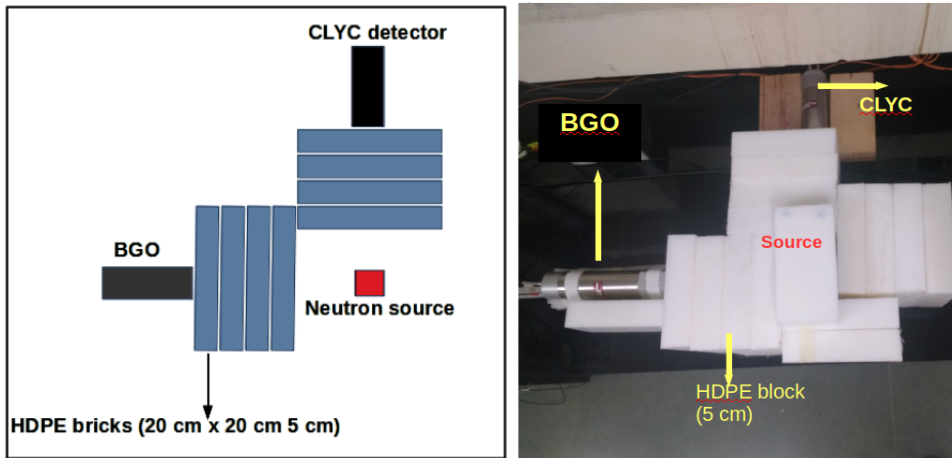
FIGURE 2.10: The schematic of the measurement setup for the optimization of HDPE thickness with CLYC and γ ray detectors (left panel). The picture of the setup is shown in the right panel.

of the HDPE. This can be attributed to the capture of the thermalized neutrons in the hydrogen of the absorber, to produce γ rays. The intensity of 2.2 MeV γ ray peak, increases initially and stays constant for moderator thickness of 10-15 cm and slowly starts to fall when the thickness is increased to 20 cm.

The optimum moderator thickness, suitable for thermalization of fast neutrons, is decided to be 10 cm based on the above measurements, which is suitable for the detection of both thermal neutrons and γ rays from neutron capture.

2.3 Thermal neutron attenuation in Borated rubber

Hydrogen rich materials loaded with Boron are well suited candidates for neutron shielding purposes. The fast neutrons can be thermalized by hydrogen present in the rubber and the high thermal neutron capture cross section of $^{10}B(n, \alpha)^{7}Li$ reaction (3840 b) can be exploited to significantly attenuate the
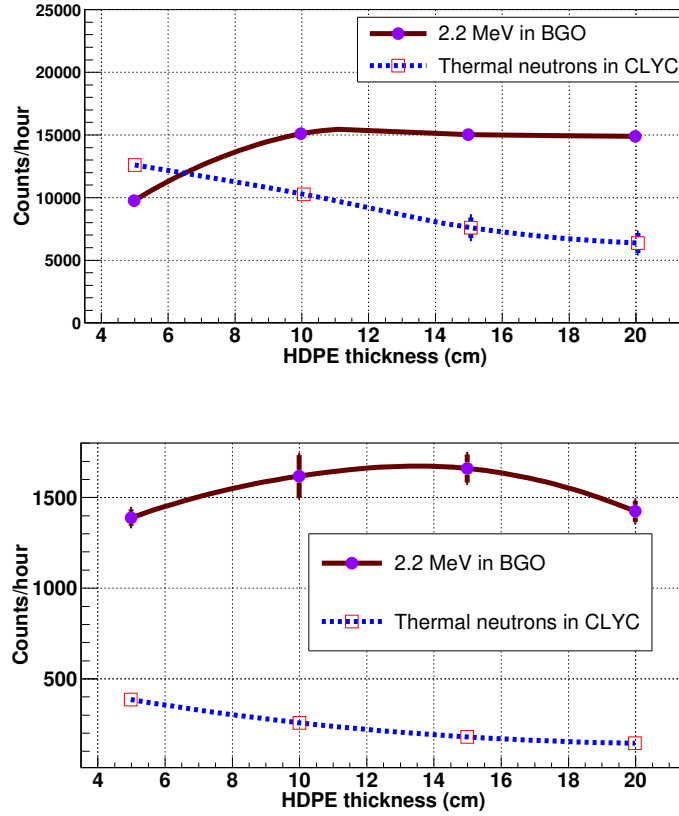
FIGURE 2.11: The yield of thermal neutron in CLYC detector and 2.2 MeV γ ray in the BGO, plotted as a function of HDPE thickness. The top panel shows the plots with ^{249}Am-^{9}Be and the bottom panel with ^{252}Cf neutron sources, respectively.

neutron flux without the production of any additional γ rays. For this purpose, borated rubber with varying concentrations of Boron, namely 10%, 20%, 30% and 50% (measured by weight) procured from Boron Rubbers India, were used. The measurement setup (schematic shown in Figure 2.12) consists of a CLYC detector for the detection of thermal neutrons and a CeBr$_3$ detector for the detection of gamma rays of energy 2.2 MeV, originating from the neutron capture in Hydrogen. The schematic of the measurement setup is shown below. Neutrons from ^{252}Cf neutron source (∼3500 dps) is used for the measurements. The data
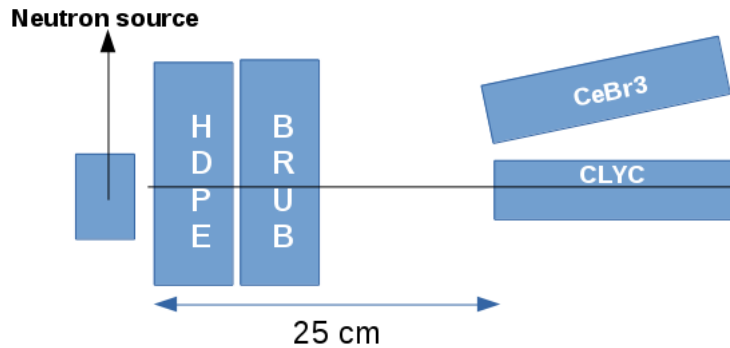
FIGURE 2.12: The arrangement of CLYC and CeBr$_3$ detectors for detecting thermal neutrons and 2.2 MeV γ rays originating from neutrons reactions in the Borated rubber.

was acquired using a the CAEN N6751 digitizer with DPP_PSD software. The parameters of the digital acquisition were optimized for obtaining best PSD separation in the CLYC. Neutrons from the source are thermalized with a High Density Polyethylene (HDPE) block of 5 cm thickness and transmitted through the borated rubber absorber. As seen in Figure 2.13, ~90% of the thermal neutron
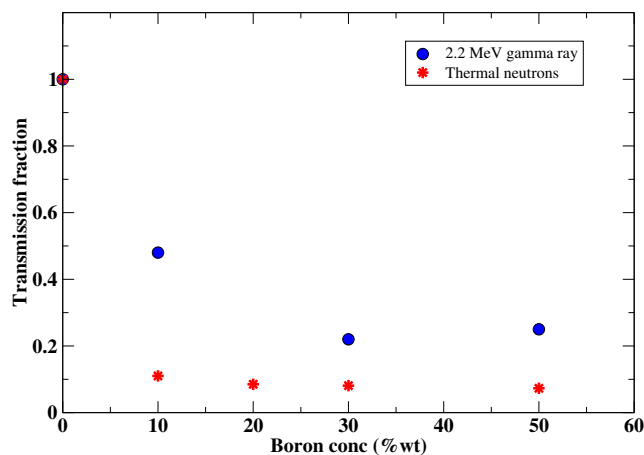
FIGURE 2.13: The transmission fraction of thermal neutrons and 2.2 MeV gamma rays for different concentrations of Boron. The transmission fraction is normalized with respect to the configuration with no absorber

flux is attenuated with 10% Boron loading. The concentration of Boron beyond 10% does not seem to affect the thermal neutron attenuation drastically. With 30% of Boron loading, the thermal neutron attenuation saturates to ~92%. It can also be seen that the counts 2.2 MeV gamma rays systematically reduces with the increasing Boron concentration.

2.4   Fast neutron activation studies

To assess the suitability of a material to be employed as low background shield, it is also important to assess the presence of dissolved impurities. For this purpose, borated rubber, borated HDPE and non-borated HDPE samples of dimension 1cm × 1cm × 1cm was irradiated in the Pelletron Linac facility, Mumbai [109] with fast neutrons from $^9Be(p,n)^9B$ (Q = -1.850 MeV) reaction. The schematic diagram of neutron irradiation setup is shown in Figure 2.14.
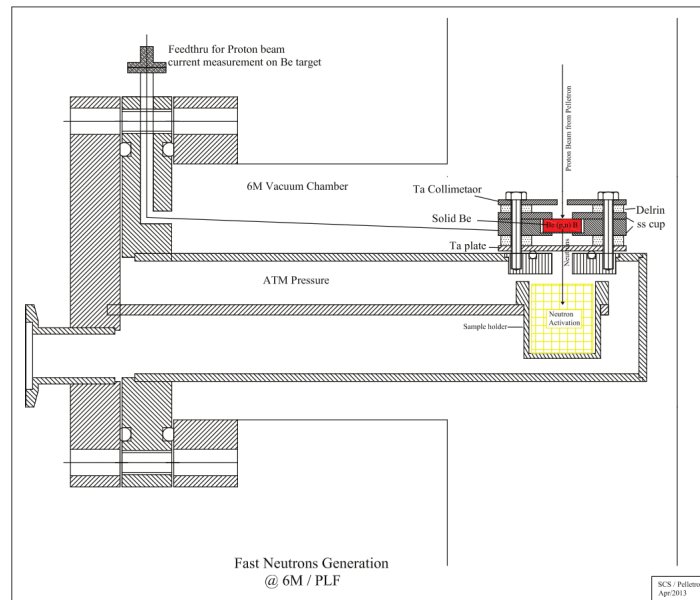
FIGURE 2.14: A schematic diagram of the neutron irradiation set up showing the production target (red box) and sample mount (yellow grid)[109]

Proton beams of energy $E_P \sim 20$ MeV on a Be target (5 mm thick) were used to obtain an average neutron flux $\sim 10^6$ n cm^{-2} s^{-1} integrated over neutron energy range, $E_n = \sim 0.1$ to ~18 MeV.

After irradiation, the samples were counted offline in the TiLES low background HPGe detector [14] for the identification of characteristic γ rays of reaction products resulting from the neutron activation. Figure 2.15, 2.18 and 2.21 shows the gamma ray spectra of the irradiated borated rubber, borated HDPE and, non borated HDPE, respectively. The list of the identified γ rays and their origin, along with the measured and literature values of the respective half lives are listed in Table 2.1.
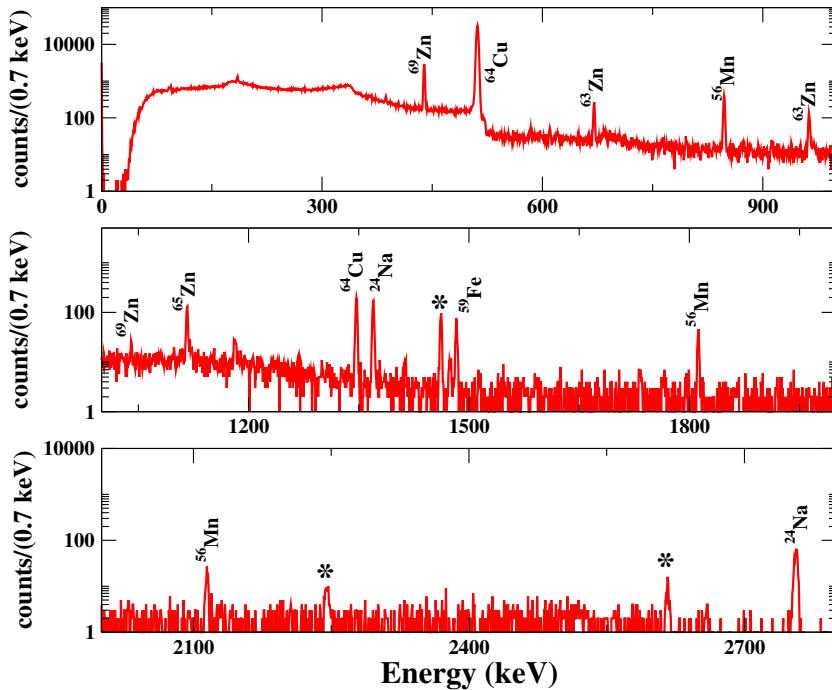
FIGURE 2.15: γ ray spectrum of irradiated borated rubber taken in HPGe detector. Sample counted on face. T_{irr} = 12 hours, T_{data} = 25 min. T_c = 1.61 h. γ rays from the ambient background are indicated with (*)

TABLE 2.1: Observed γ-rays in the irradiated samples. Lines marked with (*) could not
         be tracked due to low statistics.

Target	Reaction channel	E_γ (keV)	$T_{1/2}^{exp}$	$T_{1/2}^{ref}$
Borated rubber	$^{56}Fe(n,p)^{56}Mn$	846.8 1810.8 2113.1	2.7(4) h	2.5789(1) h
	$^{64}Zn(n,2n)^{63}Zn$	511 669.6 962.1	43 (10) m	38.5 (5)m
	$^{64}Zn(n,p)^{64}Cu$	1345.8 511	13.1(5) h	12.701 (2) h
	$^{64}Zn(n,\gamma)^{65}Zn$ $^{66}Zn(n,2n)^{65}Zn$	1115.5	*	243.93(9) d
	$^{68}Zn(n,\gamma)^{69}Zn$ $^{70}Zn(n,2n)^{69}Zn$	438.6	14.1(4) h	13.7 (2) h
	$^{27}Al(n,\alpha)^{24}Na$	1368.6 2754.0	*	14.997(12) h
Borated HDPE	$^{56}Fe(n,p)^{56}Mn$	846.8 1810.8 2113.1 2523.1 2657.6 2959.9	2.67(7) h	2.5789(1) h
	$^{59}Co(n,2n)^{58}Co$	810.6	*	70.86(6) d
	$^{54}Fe(n,\alpha)^{51}Cr$	320.08	*	27.7025(24) d
	$^{27}Al(n,\alpha)^{24}Na$	1368.6 2754.0	13(7) h	14.997(12) h
Non-borated HDPE	$^{19}F(n,2n)^{18}F$	511	114(13) m	109.77(5) m
	$^{27}Al(n,\alpha)^{24}Na$	1368.6 2754.0	15(7) h	14.997(12) h
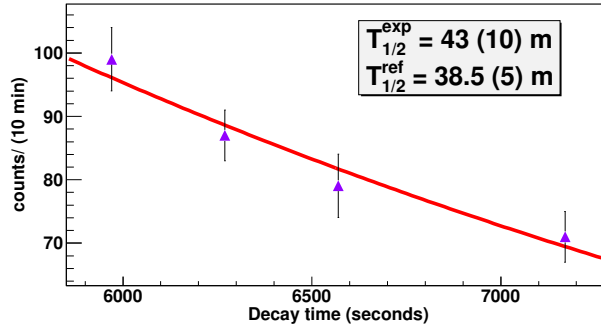
FIGURE 2.16: Decay curve for 962.1 keV from ^{63}Zn in the borated rubber sample. E_P = 20 MeV, T_{irr} = 12 hours.
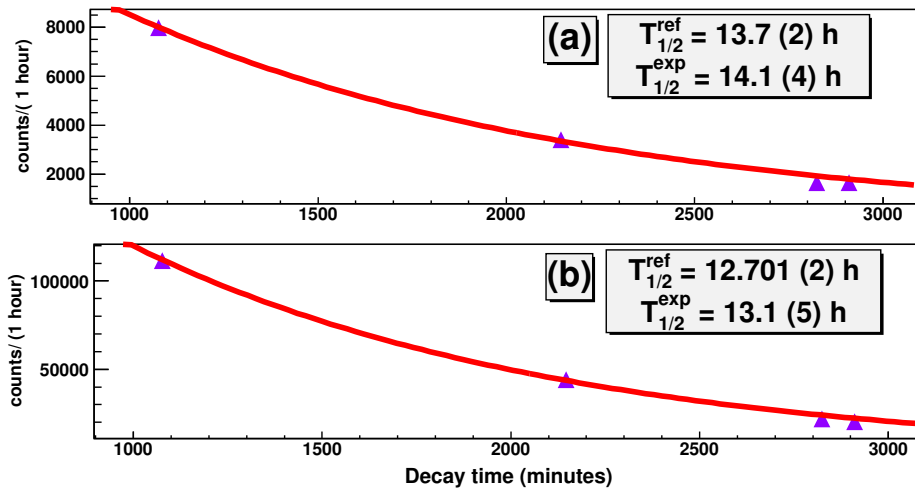
FIGURE 2.17: Decay curve for (a) 438.6 keV from ^{69}Zn and (b) 511.0 keV from ^{64}Cu from the borated rubber. E_P = 20 MeV, T_{irr} = 12 hours.

The identified γ rays, from the neutron activation of borated rubber indicates the presence of Zn and Fe. The origin of the γ rays are also confirmed by the half life tracking. The presence of Zn in the borated rubber is attributed to the addition of Boron-Zinc compounds that are used to incorporate the Boron into the rubber matrix. However, the origin of neutron activation lines from Fe
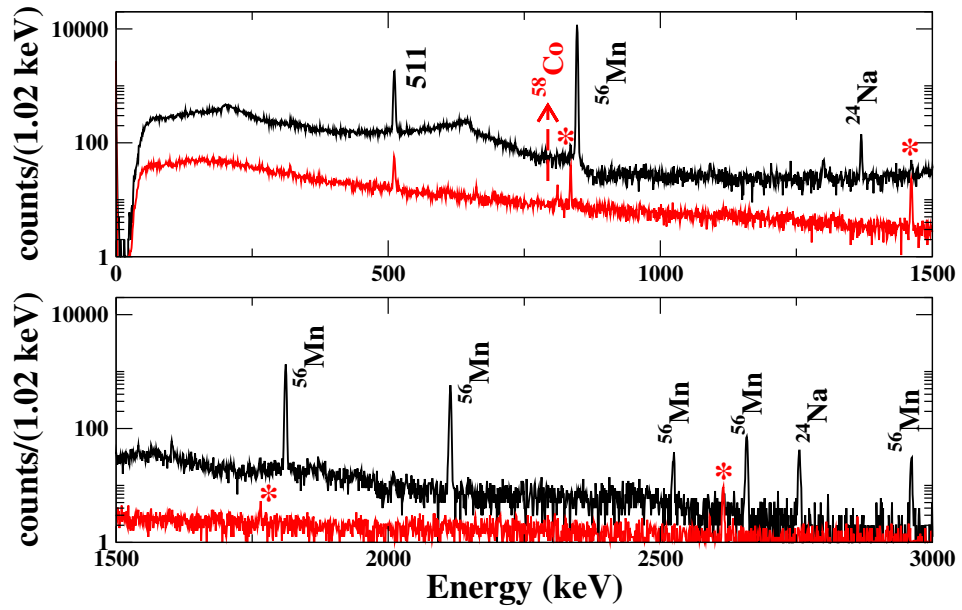
FIGURE 2.18: γ ray spectrum of irradiated borated HDPE taken in HPGe detector. Sample counted on face. T_{irr} = 12 hours, T_{data} = 4.5 h. The spectra for T_c = 2.5 h and T_c = 8.5 d are shown in black and red, respectively. γ rays from the background are inicated with (*)

FIGURE 2.19: Decay curve for 846.8 keV from ^{56}Mn in the borated HDPE sample. E_P = 20 MeV, T_{irr} = 12 hours.

are unclear. Although borated rubber is an efficient thermal neutron absorber, the observation of high energy γ-rays like 1345.8 keV from ^{68}Zn$(n, \gamma)^{69}$Zn and
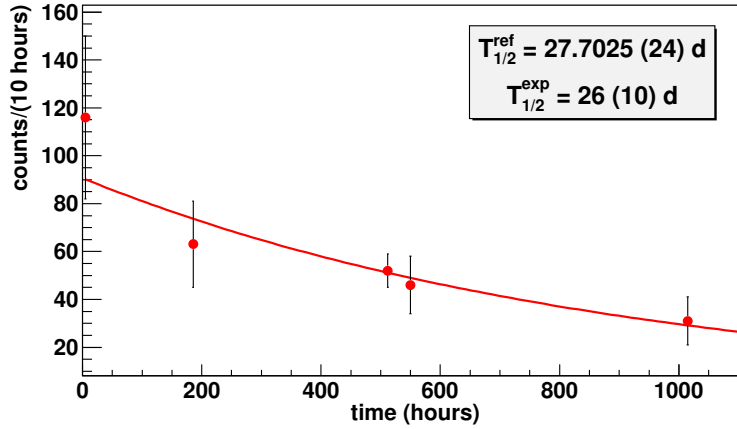
FIGURE 2.20: Decay curve for 320.1 keV from ^{51}Cr in the borated HDPE sample. E_P = 20 MeV, T_{irr} = 13 hours.

2115.9 keV from ^{56}Fe(n,p)^{56}Mn is of particular concern. Though Fe contributes to the high energy γ ray background, the activity from Fe is short lived ($T_{1/2}$ = 2.6 h). The production of long lived isomeric state in ^{65}Zn ($T_{1/2}$ = 243.9 d) is undesirable. Hence the compounds with Zn is not suitable for low background applications. The borated HDPE has not shown the presence of activity from any long lived isomeric states leading to high energy γ ray background, which makes it better suited for neutron shielding purposes. In the case of non-borated HDPE, the presence of F is identified from ^{19}F(n,2n)^{18}F reaction, which contributes to the observed peak at 511 keV. The presence of Al is identified in all the samples. However the source of Al could not be ascertained and the origin is suspected to be extraneous.
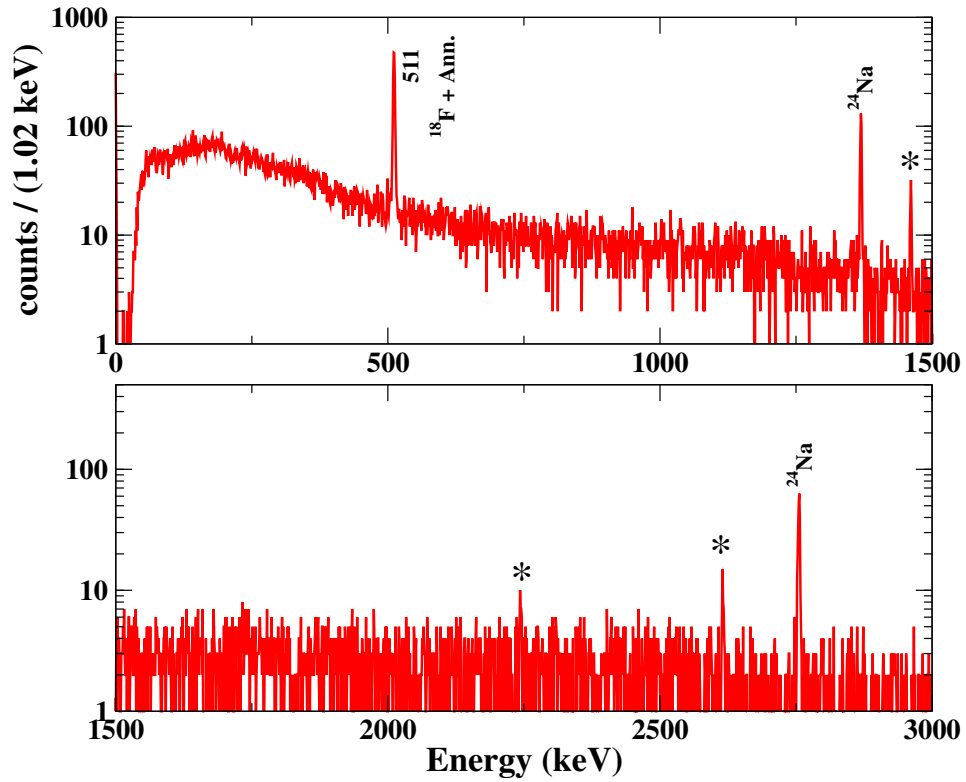
FIGURE 2.21: γ ray spectrum of irradiated HDPE (non-borated) taken in HPGe detector.
Sample counted on face. T_{irr} = 13 hours, T_{data} = 4.5 h. The γ rays from
the background are inicated with (*)
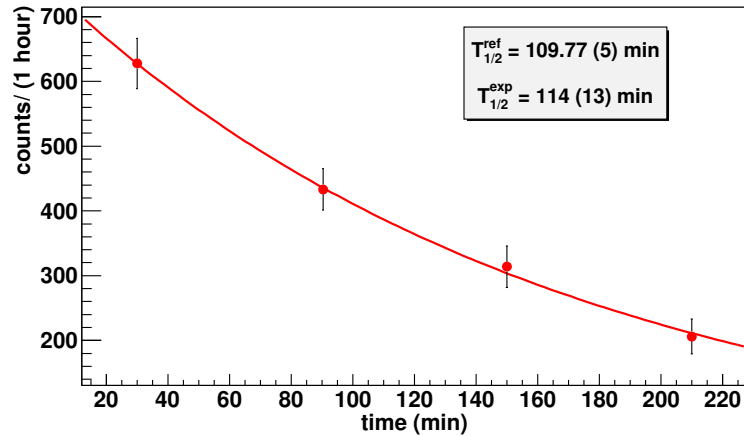
FIGURE 2.22: Decay curve for 511 keV from ^{18}F in the borated HDPE sample. E_P = 20
MeV, T_{irr} = 13 hours.

2.5   Summary

The suitability of various materials for neutron shielding purposes has been assessed. The thermalization of neutrons in the HDPE absorber was studied for varying thicknesses. The optimum thickness of HDPE, that would be suitable for the simultaneous detection of thermal neutrons and neutron capture γ rays, is obtained to be 10 cm. The attenuation of fast neutrons in borated rubber is studied for varying concentrations of Boron. It is observed that the neutron attenuation does not have a strong dependence on the boron loading. Neutron attenuation of 90% is obtained with 10% of boron loading and saturates to a value of 92% for 30% boron loading. The γ rays arising from the neutron capture steadily decreases with increasing concentration of Boron.

The fast neutron Neutron-induced background in borated rubber, borated HDPE and non-borated HDPE has been studied using fast neutron activation technique. The contribution to the gamma background has been studied with an average neutron flux $\sim 10^6$ $n\ cm^{-2}\ s^{-1}$ integrated over neutron energy range, E_n = $\sim$ 0.1 to $\sim$18 MeV. The non-borated HDPE sample has shown the presence of activity from ^{24}Na and ^{18}F, both of which are short-lived impurities. The borated rubber and borated HDPE samples have shown the presence of Al and Fe which will contribute to high energy gamma background. In addition, borated rubber has Zn impurity that can produce long-lived impurities like ^{65}Zn, with $T_{1/2}$ $\sim$ 244 d. The borated HDPE has not shown the presence of activity from any long lived isomeric states, that leads to high energy γ ray background, which makes it suitable for application as neutron shield in low background experiments.

Design of the MINT setup

Introduction

In this chapter, the Muon Induced Neutron measurement setup at TIFR (MINT), is presented. The MINT is a dedicated setup designed for the direct measurements of neutrons originating from the interactions of cosmic ray muons. As mentioned previously, the interaction of cosmic muons in high Z materials can give rise to secondary neutrons, which constitutes an important background to the rare event experimental searches. In the past, considerable experimental efforts have gone into the measurements of the cosmic muon induced secondary neutrons, using direct and indirect detection methods, both at shallow depths [12, 110, 111] as well as in deep underground locations [112–115]. Extensive simulation studies with various Monte Carlo simulation packages (GEANT4, FLUKA) have also been carried out by various groups [11, 116–119] . Significant variations are observed amongst experimental results themselves and also with simulations. Independent measurements using different reaction channels are highly essential to understand the overall experimental data and improve the

Monte Carlo simulations.

The MINT employs high efficiency thermal neutron detectors CLYC and NaIL which are superior in terms of neutron detection efficiency and performance compared to the conventional neutron detectors like liquid scintillators or ^3He based neutron counters [106]. The neutrons produced from the cosmic muon interactions are detected directly via neutron capture reaction in ^6Li present in the neutron detectors, which provides a unique signal for the neutron detection. Superior pulse shape discrimination capability and the compactness of the detector relative to liquid/plastic scintillators based detection systems, is an additional advantage. The setup is designed to be compact and portable and can be easily assembled at underground locations for neutron background measurements in the future.

This chapter describes the measurement of cosmic muon induced neutrons at the sea level, with the MINT set up. The production of neutrons in the Pb target is presented. The contribution to the neutron production from the stopping muons is also measured for Pb and Fe targets.

3.1   The MINT setup

The schematic picture and the experimental setup of MINT is shown in Figure 3.1. The setup is mounted on an Iron platform with a footprint of 80 cm × 80 cm, with Iron plates of dimensions 60 cm × 60 cm × 1 cm. The platform can hold a total weight of upto ∼ 1000 kg. Three layers of Iron plates are present for detector/target mounting (not shown in the schematic). The Pb blocks of 30 cm thickness are mounted in the top plate. The CLYC and NaIL detectors are mounted inside suitably designed HDPE mounts as shown in Figure 3.2.
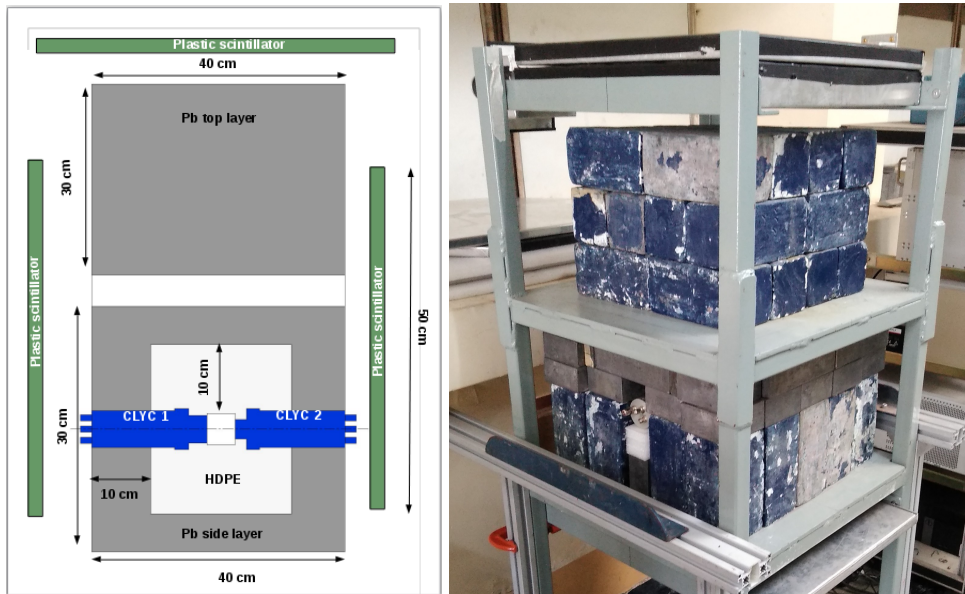
FIGURE 3.1: The schematic of the MINT experimental setup. The plastic scintillators placed in the sides are shown (left panel). The MINT setup with Pb mounting (right panel).

FIGURE 3.2: Clockwise from the top: 1. The inner view of the HDPE, 2. view of CLYC detector mounting from the back, 3. after mounting both the detectors, 4. Pb blocks partially mounted in the sides of the HDPE

The HDPE-detector assembly in mounted in the second layer, which is also
is also surrounded by Pb layers on the sides. The choice of the Pb thickness and
the discussion on the neutron production in Pb is discussed in the section 3.2.1.

3.1.1   Cosmic muon detection

In order to detect the cosmic muons entering the MINT setup, plastic scin-
tillator detectors are used. Each plastic scintillator is of area 50 cm × 50 cm
and have thicknesses ranging from 1 cm to 5 cm. Each scintillator is coupled to
a single photo multiplier tube (Hamamatsu R7723) through a light guide. The
assembly of the plastic scintillator is shown in Figure 3.3.
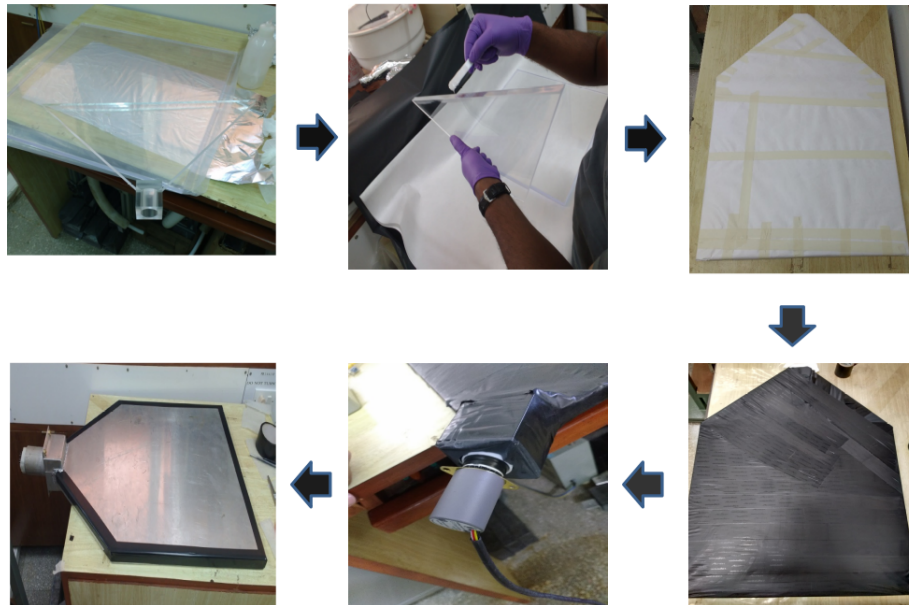
FIGURE 3.3: The assembly of the plastic scintillators for muon veto.

The operating voltages are optimized to maximize the efficiency of the plastic
scintillators, measured using coincidence techniques. The configuration for the
efficiency measurement of the scintillators is shown in Figure 3.4. Four scin-

tillators are used for the measurements, with the scintillator in the position P3, being the test scintillator whose efficiency is measured and P1,P2 and P4 being used for the trigger. The scintillators are separated by a distance of ~ 5 cm, with thin layers of Pb/Fe sheets placed in between them, to avoid the cross talk. The
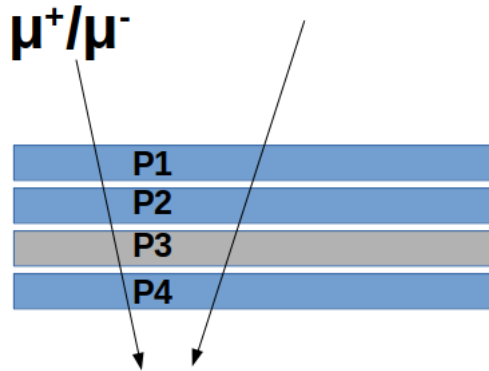
FIGURE 3.4: The schematic of the arrangement for the efficiency measurements of the plastic scintillators. The scintillator P3, is the test scintillator and the others are used for the trigger definition.

efficiency of the scintillator is given by the ratio of the number of events in four fold coincidence of all the scintillators to the number of events in the three fold coincidence, generated excluding the test scintillator :

$$\epsilon_3 = \frac{N_{1234}}{N_{124}} \tag{3.1}$$

where N_{1234} and N_{124} represents the counts measured in the four fold and three fold coincidence, respectively. It may be pointed out that the inefficiency of the trigger scintillators do not affect the measured efficiency of the test scintillator. The coincidence time window was set to 50 ns. The efficiencies of the scintilltors were measured to be in the range of 96% to 98%.

3.1.2   Neutron detection

The neutrons are detected by CLYC and NaIL detectors. The detectors are surrounded by 10 cm layer of HDPE, in all directions as shown in Figure 3.2. The description of the neutron detectors, their efficiency and choice of the thickness of the HDPE has been discussed in detail the previous chapter. The detection of the cosmic muon induced neutrons in MINT setup is as follows: the cosmic muons entering the setup are registered by the plastic scintillators followed by the muon interaction in the target material which may lead to the production of neutrons. These neutrons get transported through the Pb and HDPE, with some of them slowing down to thermal energy, which are detected by the neutron detectors via $^6Li(n, \alpha)^3H$ reaction.

The data acquisition system consists of CAEN V1730B digitizer (16 channel, 14 bit 500 Ms/s FLASH ADC, $2V_{pp}$), with digiTES (4.5.12) software. A pulser unit, set to 10 Hz in frequency, is also connected to the digitizer for monitoring purposes. The digital parameters for each of the detector is tuned separately and input to the digitizer through the digitizer configuration file. The settings of the neutron detectors have been discussed in Chapter 2.

3.2   Measurement of muon induced neutrons

3.2.1   Neutron production in Pb

For the measurements of neutron production in Pb, Pb blocks of 30 cm height and 40 cm × 40 cm footprint are mounted on the top ($\sim$ 528 kg) and surrounding the HDPE ($\sim$ 230 kg) as shown Figure 3.1. For this run, two CLYC detectors, both of 1″ × 1″, are employed. Five plastic scintillators one

at the top and four surrounding the setup, covering the Pb-HDPE castle, were
employed for detecting the cosmic muons. The independently acquired data of
the plastic scintillators are time ordered, zero suppressed and combined in a time
window of 150 ns, retaining the event flag for each of the plastic scintillator.
The event flag provides the information of the plastic scintillators which have
recorded a muon event in the time window. The search for the coincidence
between the muon events in the plastic scintillators and the neutron events in the
neutron detectors were performed using ROOT and C++ based offline analysis
algorithms. The time window for the muon to neutron delayed coincidence was
chosen considering the neutron transport and thermalization time in the MINT
geometry. For this purpose, Monte Carlo simulations were performed using
GEANT4 toolkit [16, 17]. Neutrons of energy E_n = 10 MeV were randomly
distributed in the volume of the Pb mounting. These neutrons are transported
through the Pb and HDPE geometry, until they enter the neutron detector. The
time distribution of the neutron of energies 10 MeV is shown in the Figure 3.5. It
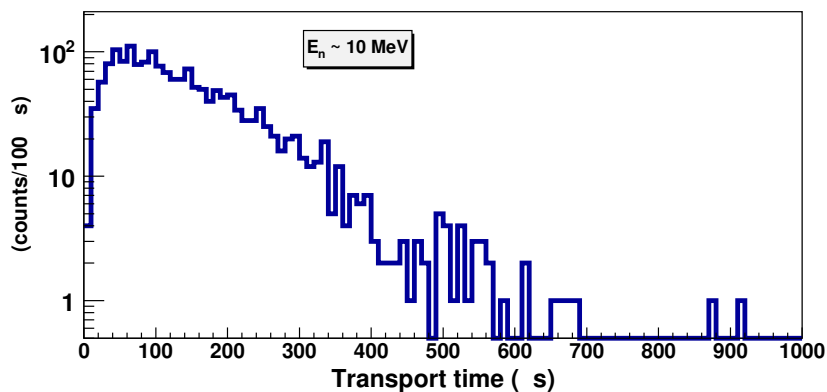
FIGURE 3.5: The transport time for neutron of energy 10 MeV in the MINT geometry,
simulated using GEANT4 toolkit. 10^5 neutrons were generated.

can be seen that the tail of the time distribution goes ∼ 700 μs. The prompt time

window for the coincidence was thus chosen to be in the range of 500 to 750 μs.

However, to assess the contribution from the background events (which comes

from the neutron generated by the non triggering muons as well as from the

natural radioactivity), wider time window needs to be chosen. Considering this,

a time window of ±10 ms was chosen for performing the offline coincidence. The

coincidence search for neutrons in CLYC is performed with the combined plastic

scintillator data. Figure 3.6 shows the coincidence time spectrum between the

plastic scintillator and the CLYC detector, for the thermal neutron events detected

in CLYC. A sharp rise in the detected thermal neutron counts can be seen in the 0
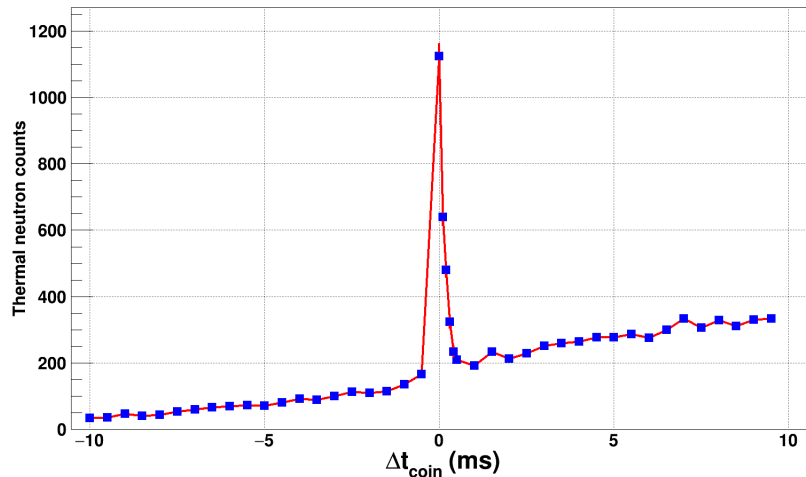
FIGURE 3.6: Evolution of the thermal neutron event rate in the CLYC detector, in the
coincidence time window. The prompt time window is indicated in dashed
lines.

to 100 μs window. The event rate falls and comes down to the background level

by ∼ 500 μs. This is the prompt window for the event selection. Figure 3.7 shows

the neutron-gated energy spectrum, combined for both the CLYC detectors. Table
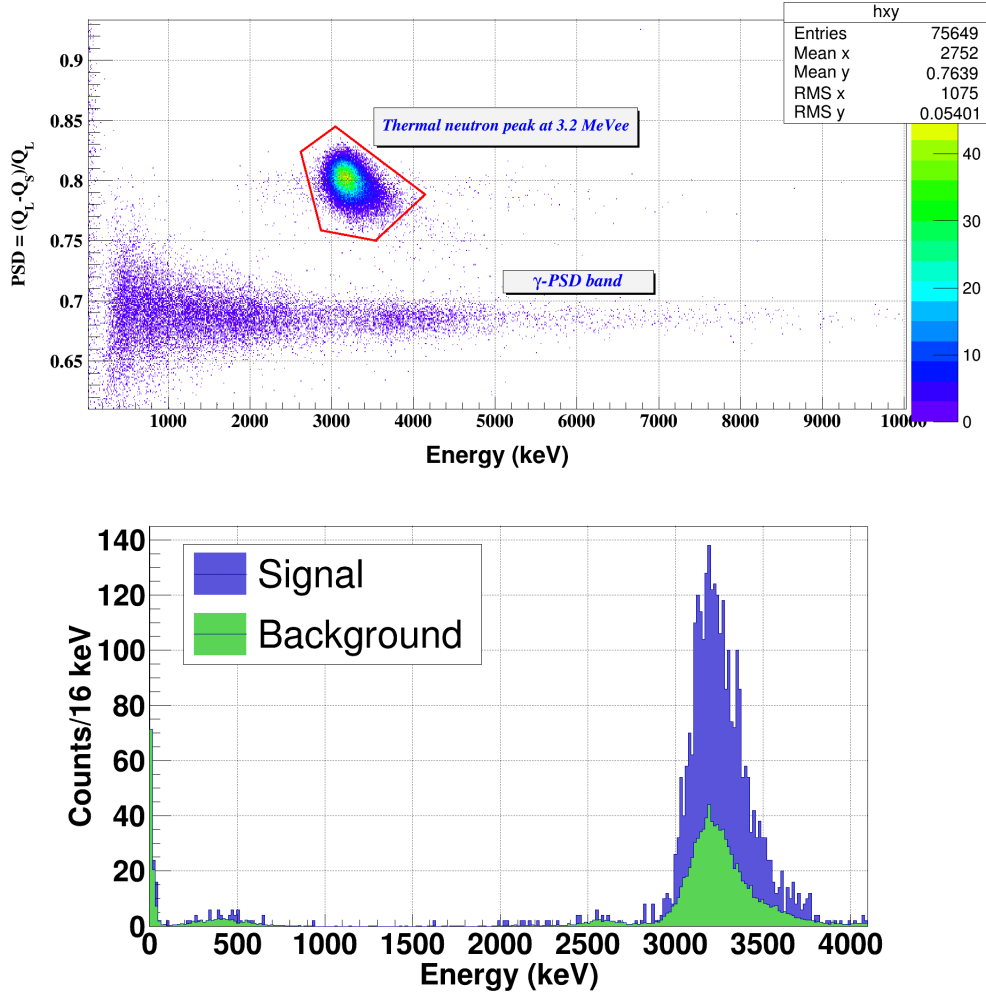
FIGURE 3.7: The energy-PSD spectrum of the CLYC detector (top panel) Neutron gated
energy spectrum in the CLYC detector (bottom panel). T_{data} = 40 days.

below summarizes the data acquired, for a period of 40 days, with the Pb target

	counts
Counts in T_{prompt}	2802 (306)
Counts in T_{chance}	869 (239)
Corrected counts (day^{-1})	48 (14)

The counts to the left and right of the prompt window is used for the chance

correction. The counts in the chance window has been normalized to the width of

the prompt, 500μs. The error bars on the counts are statistical. The thermalization fraction for the neutron from ^{252}Cf source for energy upto 10 MeV, has been measured independently, as explained in Chapter 2 and found to be $\sim 50\%$. Correcting for the thermal neutron detection efficiency of the CLYC, $\sim 25\%$, the neutron production in the Pb target for an effective thickness of 30 cm is obtained as 8.1 ± 2.4 neutrons $g^{-1}cm^2$ day^{-1}.

3.2.2   Neutron production from stopping muons

The dominant process governing the production of neutrons from cosmic muons, at the sea level and shallow depths is the capture of negative muons in the target. Even though most of cosmic muons pass through layers of materials without coming to a stop, the low energy component [110], typically, $E_\mu < 500$ MeV, can be stopped in sufficiently thick materials of high mass. The capture of a negative muon by the atomic nucleus can be written as:

$$\mu^- +^Z N \to^{Z-1} N' + \nu_\mu \qquad (3.2)$$

The final nucleus produced in the excited state, has the extra neutron which can either leave the nucleus directly or transfer the energy to the other nucleons, leading to the emission of multiple neutrons and γ rays.

The first studies of the neutron production from stopping muons was conducted by Sard et.al [120] and Groetzinger et.al [121] in Pb and Fe targets, respectively. The μ^- capture probability increases rapidly with the atomic number Z. For low Z, the capture probability is roughly proportional to Z^4. The Z^4 law, which is approximately valid for low Z is because of the fact that the capture probability is proportional to the number of protons in the nucleus, Z and the density of the μ^- wave function in the volume of the nucleus, which is propor-

tional to Z^3 [122, 123]. As the Z increases the measured probability departs from this simple law and for heavy nuclei with $Z \geq 40$, the capture probability reached a saturation value. This is because the muon radius becomes comparable to the nuclear radius and corrections have to be applied and an effective Z, Z_{eff} is calculated to obtain the modified muon capture rates [124].

In the MINT setup, measurements were performed for assessing the contribution of the stopping muons to the neutron production. In this run, one CLYC and one NaIL detector was used. The NaIL was primarily chosen due to higher detection efficiency and the possibility of the dual detection of thermal neutrons as well as gamma rays with a high efficiency. A schematic of the MINT configuration for the neutron measurement from stopping muons is shown in Figure 3.8. The configuration for measuring the stopping muons in MINT for Pb and Fe targets is shown in Figure. 3.9. The configuration of the Pb mounting for the measurement of neutron production is same as the previous run, on the top and the sides, surrounding the HDPE. In the case of Fe, the target is mounted only at the top, with a footprint of 30 cm $\times$ 30 cm and thickness of 30 cm,a s shown in the right panel of Figure 3.9. Four plastic scintillators are used in total in this configuration, two at the top (P1 and P2) and two at the bottom (P3 and P4). The events in the plastic scintillators are time ordered and combined in a window of 150 ns, retaining the event flag for each plastic detector, as in the previous run. The low energy component of the cosmic ray muons, which are close to the end of their range can come to a stop in the layer of the target material. In order to identify the neutrons produced by the low energy muons that comes to stop in the target, the trigger criteria is suitably modified. The scintillators on the top, namely P1 and P2, registers a muon event in coincidence.
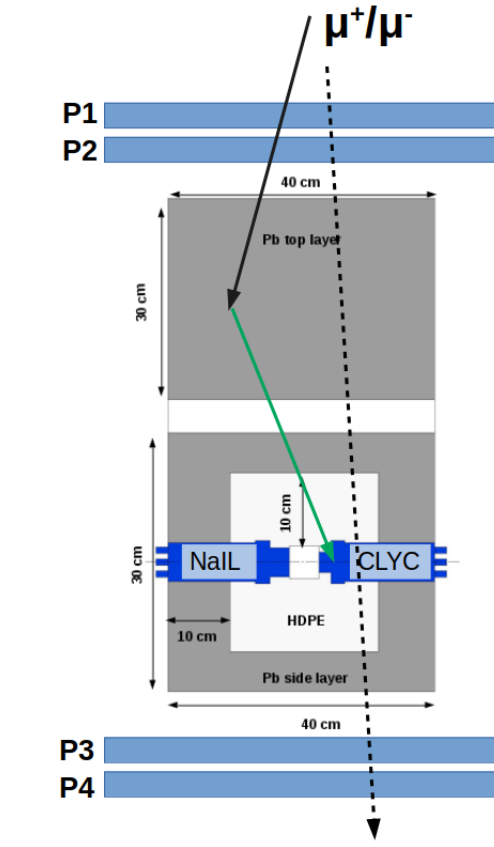
FIGURE 3.8: The schematic diagram of the configuration of stopping muon measurements in the MINT setup. The muons tracks are represented in black and neutrons in green.

For the muons that comes to a stop in the target, the bottom scintillators P3 and P4 does not register a muons. Thus, to estimate the neutron production from stopping muons, the delayed neutron signals in the CLYC/NaIL detectors are obtained with the following trigger condition: $(P1 \& P2) \& (\overline{P3} \& \overline{P4})$. Similarly, the contribution from the non stopping muons are obtained with the condition $(P1 \& P2) \& (P3 \& P4)$, followed by a delayed neutron coincident event. The presence of 2.2 MeV γ ray from $^1H(n, \gamma)^2H$ can also be seen in the NaIL detector as indicated in Figure 3.10, bottom panel. However, the Compton scattering
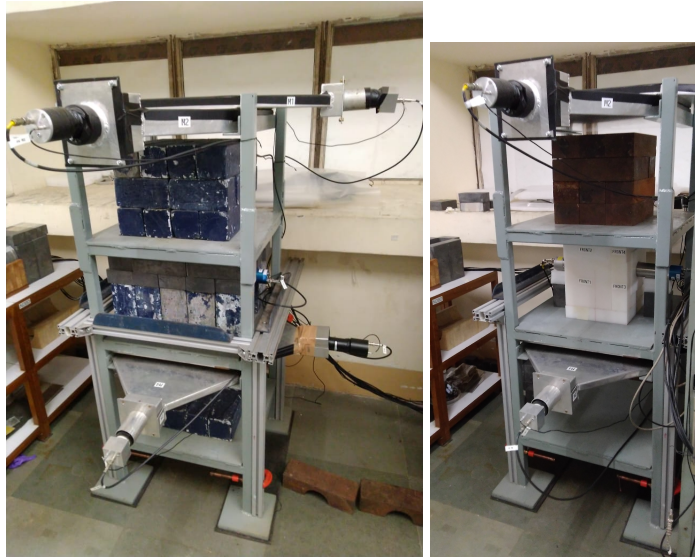
FIGURE 3.9: The configuration for the measurement of neutron production from stopping muons, in the MINT setup for Pb (left panel) and Fe (right panel).

background of the background γ ray at 2615 keV which arises from ^{208}Tl and the poor energy resolution of the detector, makes it difficult to reliably extract the neutron yield from the observed intensity of 2.2 MeV. The data was acquired for a total of $\sim$ 40 days for Pb target and $\sim$ 21 days for Fe. The energy-PSD spectrum of NaIL detector with Fe target is shown in Figure 3.11. The neutron yield is extracted from the number of events in the thermal neutron peak, with the trigger condition defined for the stopping muons. The background correction was performed by considering the counts gated upon the chance region of the coincidence time spectrum, as indicated in Figure 3.12. The number of thermal neutrons detected are normalized to the number of the incident muons (obtained from P1-P2 coincidence for stopping muons and P1-P2-P3-P4 coincidence for non stopping muons). The time spectrum shows an increasing trend towards the right of the prompt peak, the reason for which is not clearly understood. The detected neutron in the NaIL detector for Fe and Pb targets is summarized below:
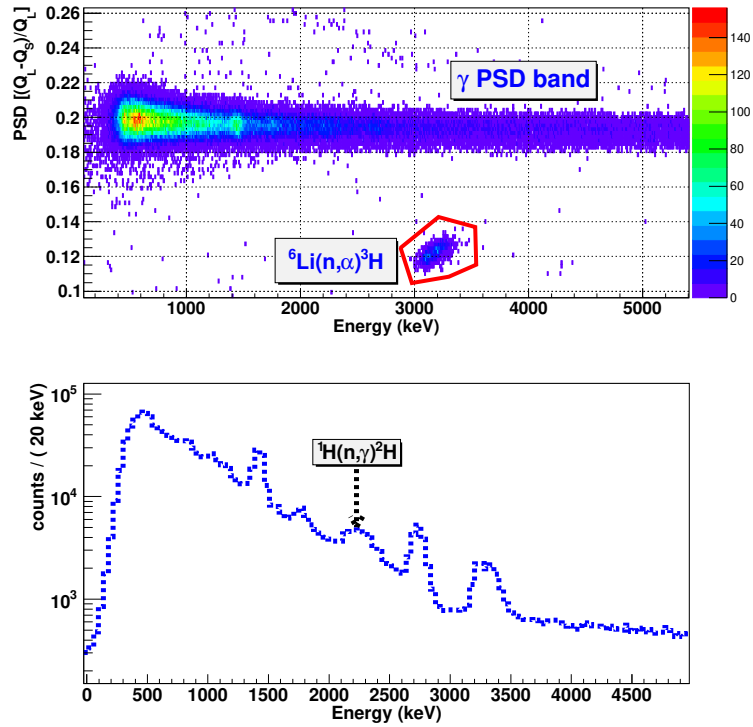
FIGURE 3.10: The Energy-PSD spectrum of NaIL detector (top panel) Energy-1d spec-
trum of NaIL detector. Gamma ray arising from $^1H(n,\gamma)^2H$ at 2.2 MeV is
indicated (bottom panel). T_{data} = 40 d with Pb target
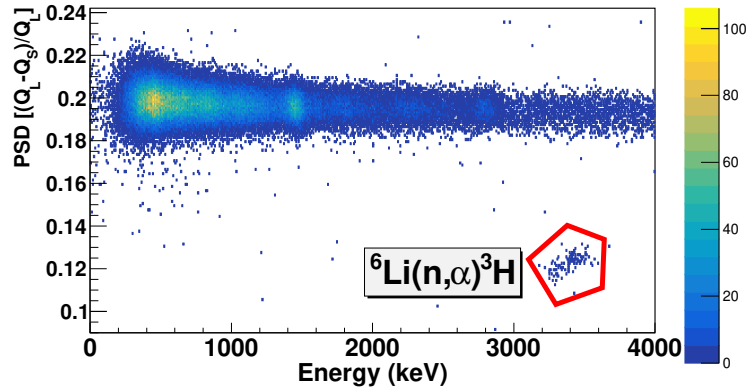
FIGURE 3.11: The Energy-PSD spectrum of NaIL detector. T_{data} = 21 d with Fe target
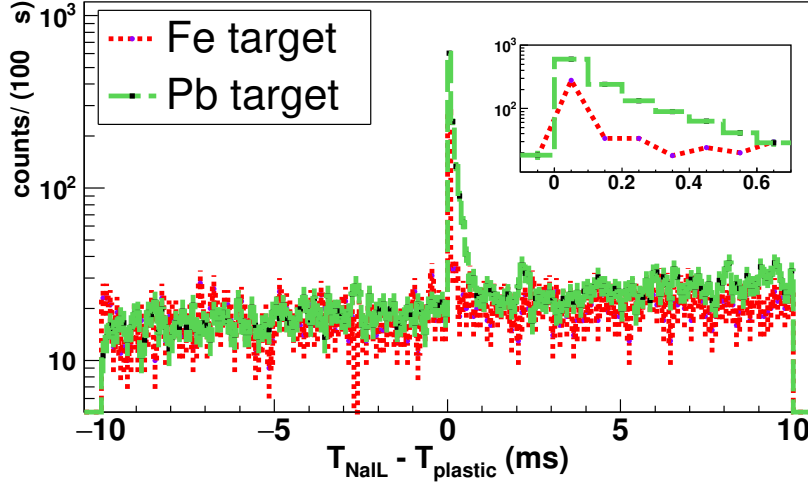
FIGURE 3.12: The coincidence time spectrum between the NaIL detectors and plastic scintillators for Fe and Pb targets. The prompt region is shown in the inset. The data is normalized to 21 days of counting time.

TABLE 3.1: Summary of the measurements in Pb and Fe targets for neutron production from stopping muons, in the NaIL detector. The numbers indicated in bold is normalized to target area of 30 cm × 30 cm.

Stopping muons	Pb	Fe
Thermal neutron counts/μ (prompt)	1.1 (0.3)×10^{-2}	1.9 (0.2)×10^{-4}
Thermal neutron counts/μ (chance)	0.25 (0.003)×10^{-2}	6.3 (0.2)×10^{-5}
chance corrected counts/μ	8.8 (0.3)×10^{-3}	1.2 (0.2)×10^{-4}
	4.9 (0.2) ×10^{-3}	
Non stopping muons	Pb	Fe
Thermal neutron counts/μ (prompt)	2.6 (0.4)×10^{-3}	1.9 (0.6)×10^{-3}
Thermal neutron counts/μ (chance)	0.23 (0.002)×10^{-2}	6.1 (0.2)×10^{-5}
chance corrected counts/μ	2.4 (0.4)×10^{-2}	1.9 (0.6)×10^{-3}
	1.4 (0.3) ×10^{-2}	
Total (neutrons/μ)	3.3 (0.5)×10^{-2}	2.0 (0.6)×10^{-3}
	1.8 (0.3) ×10^{-2}	

The neutron production from the stopping muons in Pb exceeds the production in Fe by a factor of ∼ 40. However the configurations of the Fe and Pb targets are

not completely equivalent. Hence for completely understanding the production rates of neutrons in Fe and Pb for the respective counting geometries in MINT, Monte Carlo simulations are necessary.

3.3   Summary

A dedicated setup, for measuring cosmic muon induced neutrons, MINT, has been developed. Novel, high efficiency neutron/gamma dual detectors, CLYC and NaIL are employed in the measurements. Initial measurements with MINT has been carried out at the sea level, at TIFR Mumbai. The neutron production from cosmic ray muons for Pb target has been measured to be 8.1 ± 2.4 neutrons $g^{-1}cm^2$ day^{-1} for an effective Pb thickness of 30 cm. The contribution to the secondary neutron production from the low energy stopping muons is assessed for Pb and Fe targets. Neutron yield of 4.95 $(0.15) \times 10^{-3}$ neutron/μ and 1.22 $(0.23) \times 10^{-4}$ neutron/μ is obtained for the Pb and Fe targets, respectively. The production from the stopping muons in Pb exceeds the production in Fe by a factor of $\sim$ 40. Detailed Monte Carlo simulations are necessary to completely understand the neutron production. The compact and portably design of the MINT setup, makes it ideal for the measurements in the underground laboratory locations.

Study of γ ray background from cosmic muon induced neutrons

Introduction

This chapter presents the measurements of cosmic muon induced neutrons measured in the Tifr Low-background Experimental Setup (TiLES)[14]. The setup is surrounded with Pb-Cu composite shield. Cosmic ray muons interact with the shield materials to produce secondary neutrons. These neutrons can inelastically scatter in the detector and shield materials. In the present measurement, the γ rays originating from the scattering of cosmic muon induced secondary neutrons have been measured by neutron inelastic scattering reactions. The γ rays generated in the the Cu shield (placed close to the detector) and the Ge detector crystal has been measured. Monte Carlo simulations were carried out with GEANT4 toolkit, for two different versions namely GEANT4.10.00 and GEANT4.10.05. [16, 17] and the results are compared with the experimental data.

4.1 Neutron production in TiLES setup

The TiLES HPGe detector is a coaxial p-type Ge (ORTEC GEM75-95-LB-CHJ), specially designed for low background measurements and rare dcecay studies[125] with a relative efficiency of 70% and an active detector volume of $\sim$ 230 cm^3 [14]. It has a low background carbon fiber outer body and copper support structures with a 60 cm long cold finger attached to a J-shaped cryostat. In addition to electrical contacts, the detector is surrounded by aluminized mylar and thin copper on sides as well as on bottom for thermal shielding. The setup is located at TIFR, Mumbai, at an elevation of $\sim$ 10 m from the sea level (Figure 4.1 and 4.2). The detector is shielded with 5 cm OFHC (Oxygen Free High Conductivity) Cu, 10 cm low activity Pb (^{210}Pb $<$ 0.3 Bq/kg) and an active cosmic muon veto system using four plastic scintillators (50 cm $\times$ 50 cm $\times$ 1 cm), placed at the top and on three sides. The plastic scintillators are coupled through a light guide to a single PMT (Photonis XP2262/B) operated at a voltage of -1.8 kV. The detector volume is enclosed in a Radon exclusion box made of Perspex, which is continuously purged with boil-off N_2 at an over-pressure of $\sim$10 mbar to reduce the ^{222}Rn contamination. TiLES is one of the best low background setup at sea level with an integral background rate of 1.7×10^4 /day/kg over the energy range of 40-2700 keV. In particular, the sensitivity achieved for ^{40}K and ^{232}Th are 2 mBq/g ($\sim$60 ppm) and 1 mBq/g ($\sim$0.25 ppm), respectively.

For the present analysis, coincidence of cosmic muons only with the top plastic scintillator has been considered, since the configuration of the side plastic scintillators varied during the measurement period. The top plastic scintillator has

a solid angle coverage[1] of 2.8 sr for the TiLES. From geometrical considerations, the top plastic scintillator accounts for ~ 50% of muons entering the setup, which is also consistent with simulations. The efficiency of the top plastic scintillator is measured to be 98%. The data acquisition system consists of a commercial CAEN N6724 digitizer (14-bit, 100 MS/s). The data from the detectors are acquired on an event by event basis with a time stamp. The dead time is monitored using a constant 10 Hz signal from a standard pulser connected to the pre-amplifier of the HPGe detector. The coincidence/anti-coincidence between HPGe and plastic scintillators are projected using offline algorithms developed in ROOT [13] and C++. A typical background spectrum, with partial cosmic muon veto (i.e. only with top plastic scintillator) is shown in Figure 4.3. It can be seen that γ rays arising from ambient thermal neutron capture and fast neutron reactions in Ge, Cu are visible in the spectrum. The contribution to $(n, n'\gamma)$ arises from natural radioactivity in the ambient as well as from the neutrons produced by non triggering muons entering the shield from the sides of TiLES.
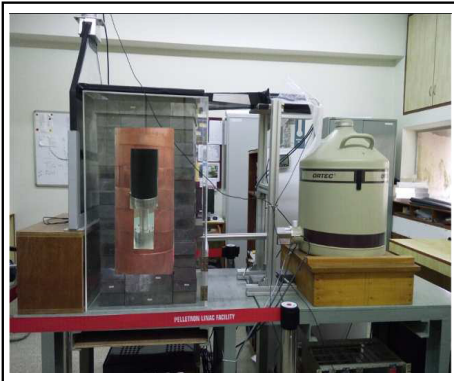
FIGURE 4.1: A schematic picture of TiLES
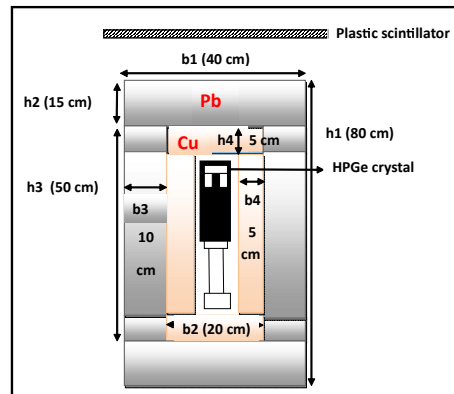
FIGURE 4.2: A cross-sectional view with shield dimensions

[1]with respect to the center of the Ge detector crystal

The data considered for the present analysis has been taken over an extended period of time and combined to a total of 329.2 days of live collection time, corresponding to $1.24 \pm 0.06 \times 10^9$ muon triggers. A subset of the data also consists of runs which were used for material screening and other measurements. This however, does not have any effect on the observed yield of the lines of interest in the coincidence γ-ray spectrum. Care has been taken to ensure that the experimental conditions remained stable throughout the data taking period. The count rate and FWHM of background lines at 661 keV (^{137}Cs) and 1460 keV (^{40}K) remained constant within the statistical error ($\pm 5\%$) for each data sub-set. The measured FWHM, integrated over the entire dataset, is 2.6 keV at 1460 keV.
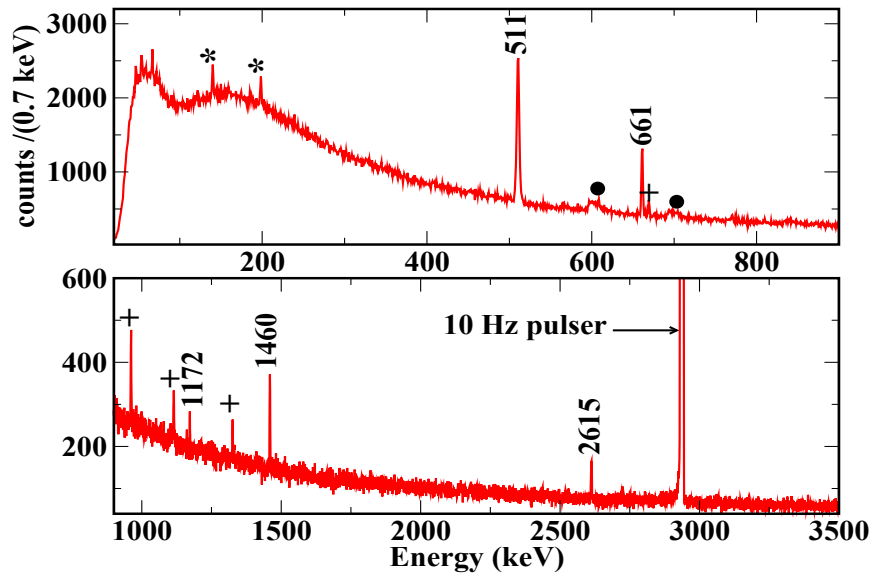
FIGURE 4.3: A typical γ-ray spectrum of room background in the TiLES HPGe detector with partial cosmic muon veto. Gamma rays arising from (n, γ) in Ge ($*$), $(n, n'\gamma)$ in Ge ($\bullet$) and Cu($+$) are indicated. (T_{data} = 27 d)

The incident muon flux for the TiLES is defined by the number of identified

muon triggers in the top plastic scintillator. At sea level, the dominant contribution to neutron production comes from the low energy component of the cosmic ray muon flux [110, 126] via μ^- capture in an atomic nucleus. Muons with energy $\sim$ 500 MeV, have a range[2] of $\sim$ 30 cm in Pb. For vertically travelling muons (selected by the top plastic scintillator), the effective shield thickness is larger than 30 cm and hence muons of energy $\leq$ 500 MeV are expected to stop in the Pb shield. The secondary neutrons undergo inelastic scattering, producing γ rays via $(n, n'\gamma)$ reaction in the Pb+Cu shield and Ge detector crystal. The coincidence search algorithm filters γ-ray events in HPGe detector within a 50 μs time window of the muon trigger in the plastic scintillator. Figure 4.4 shows the time distribution between the plastic scintillator and HPGe events. The optimal prompt time window was chosen to be T_{prompt} = 15 μs, as shown in Figure 4.4. Both the left and right side time windows of the prompt peak are used for the background correction. The background includes contributions from chance coincidence, muons incident from directions other than vertical as well as ambient neutrons from natural radioactivity. The γ-ray spectra of HPGe detectors gated on prompt and chance time windows are shown in Figure 4.5, where the lines of interest arising from $(n, n'\gamma)$ reactions in Cu and Ge are indicated. The γ rays from Pb are not visible in the spectrum because of attenuation in Pb material itself and the Cu shield. It should be mentioned that the pulser count rate has been used to independently verify chance corrections and for the estimation of the dead time.

---

[2]obtained from GEANT4 simulations with mono energetic muons
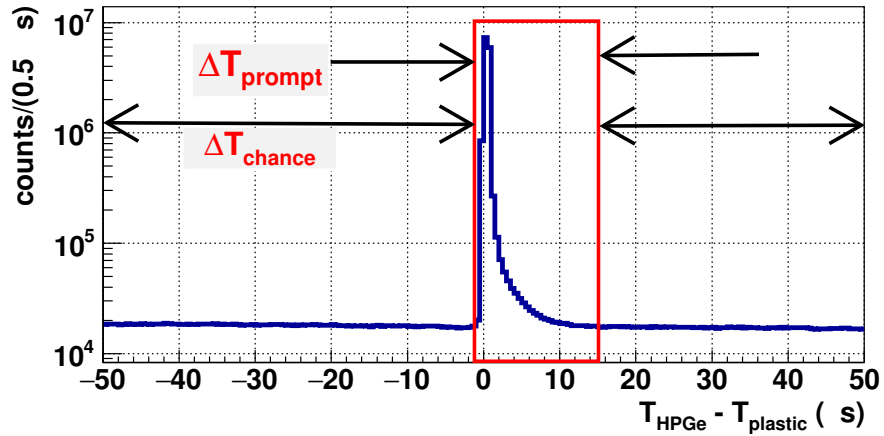
FIGURE 4.4: A coincidence time spectrum between the HPGe detector and the plastic scintillator
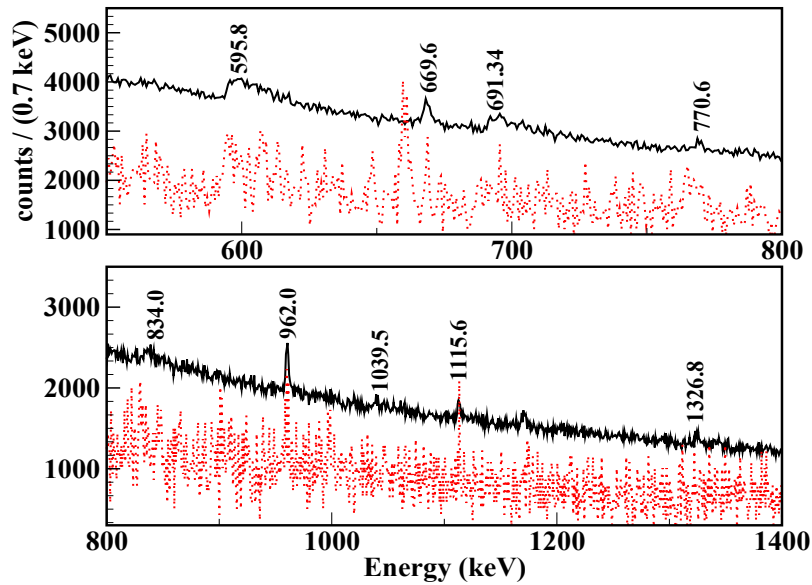
FIGURE 4.5: Prompt (black) and chance (red) gated γ-ray spectra in the TiLES HPGe detector. The chance gated spectrum has been scaled up by an arbitrary factor (~330) for better viewing (T_{data} = 329.2 days).

4.2 Monte Carlo simulations

Monte Carlo simulations of the generation of γ-ray spectrum from muon induced secondary neutrons in TiLES detector involves three steps: (i) generation of the primary cosmic muon energy and angular distributions at the geographical location of the experiment, (ii) production of secondary neutrons in Pb and Cu, from the cosmic muon distributions obtained in the first step and (iii) the production of γ rays via inelastic scattering of neutrons in Cu, Ge and their detection in HPGe detector. The actual experimental shield geometry together with the optimised TiLES HPGe detector model [14] has been employed in the simulations. The primary cosmic muon energy and angular distributions are generated using CORSIKA package [15] for Mumbai location ($18^\circ54'$N, $72^\circ48'$ E), using the rigidity cut off map for the primary protons as described in [127]. Simulation of production of secondary neutrons and $(n, n'\gamma)$ were carried out using GEANT4 toolkit [16, 17]. For the muon charge ratio, the experimental value of 1.276 ± 0.003 [128] has been used, though a slightly lower value of 1.17 has been obtained from the CORSIKA simulations. Two step approach of separating neutron production and inelastic scattering was adopted to generate statistically significant γ-ray yield in optimal computation time using standard desktop computers. The simulated neutron distribution (momentum and position) obtained in the second step is fitted to an empirical function, and is used as an input for the production of γ rays via inelastic scattering in the third step.

In the previous works, discrepancies in neutron production have been reported for older versions of GEANT4(9.6) [12]. Ref. [113] has reported an enhancement in the neutron yield in Pb with GEANT4.9.5 as compared to GEANT4.8.2.

The present study employs two recent versions, namely, GEANT4.10.00 and GEANT4.10.05. The main difference relevant to the present study is in the evaluated neutron cross section data, which is taken from G4NDL4.4 and G4NDL4.5 libraries for GEANT4.10.00 and GEANT4.10.05, respectively. Further, the choice of Physics list in simulations is an important factor. The QGSP_BERT is recommended Physics list for high energy hadron interactions and is suitable for neutron production by cosmic muons, while the Shielding Physics is better suited for low energy neutron transport processes and hence more relevant for the γ production via neutron inelastic scattering . Since the present study involves neutron production, transport and inelastic scattering, simulations have been carried out with both the Physics lists. The simulation data sets are labelled as:

- Set 1a :GEANT4.10.00.p04 with QGSP_BERT_HP (version 3.0)

- Set 1b :GEANT4.10.00.p04 with Shielding Physics (version 2.1)

- Set 2a :GEANT4.10.05 with QGSP_BERT_HP

- Set 2b :GEANT4.10.05 with Shielding Physics

4.2.1   Neutron production from cosmic ray muons

The muon source geometry employed in current GEANT4 simulation is a generator plane of dimensions 5 m × 5 m, placed at a distance of 20 cm above the setup, that is, on the top of the Pb shield layer. The muon position, momentum and angular distribution are randomised at this generator plane using the CORSIKA output histograms, as shown in Figure 4.6 and 4.7. A total of 5×10^7 muons were generated to obtain the secondary neutron distributions for each set.
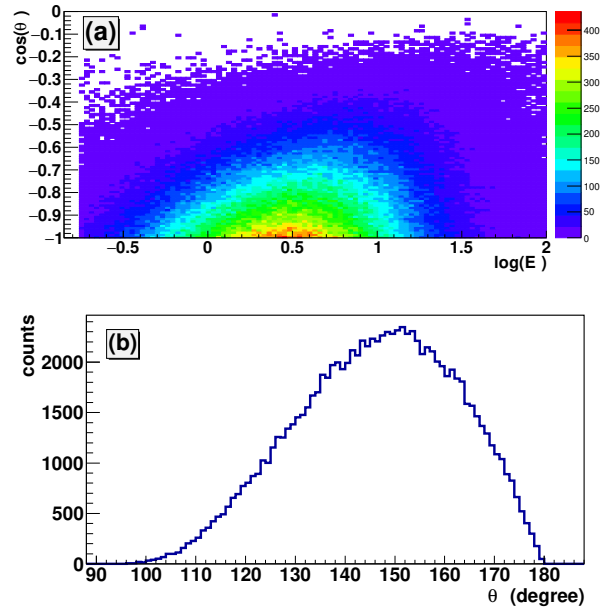
FIGURE 4.6: Energy (GeV) and angular distribution of muons from CORSIKA output: (a) $log(E_\mu)$ vs $cos(\theta_\mu)$ (b) θ_μ distribution (θ_μ is measured w.r.t. Zenith).
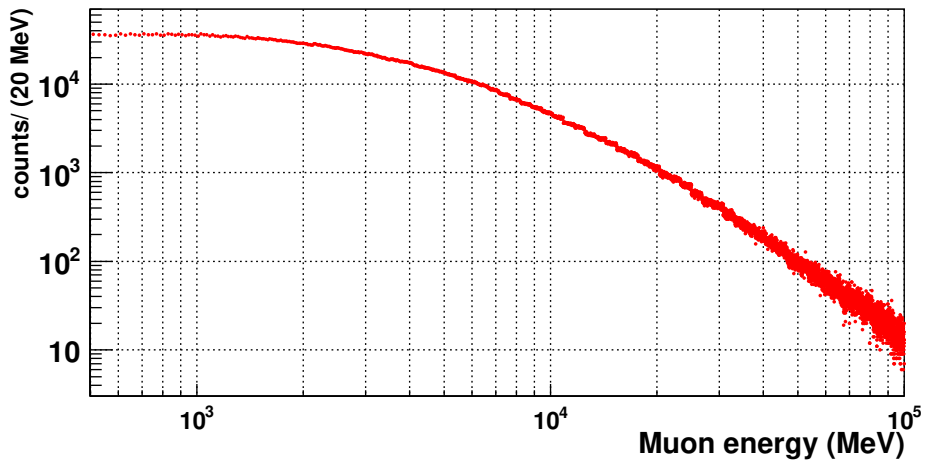
FIGURE 4.7: Energy spectrum of the cosmic muons at sea level generated from COR-SIKA, for Mumbai location.

The generated muons are propagated through the TiLES volume. A muon event in the simulations is accepted as a "triggered" event if it passes through

the top plastic scintillator and enters the TiLES volume. The accepted muon events are corrected for the efficiency of the plastic scintillator. The neutrons generated by the triggered muons are stored for further analysis. The parameters recorded for secondary neutrons are: the spatial and momentum distribution, the physics process of creation and the volume where neutron is produced. It should be mentioned that multiple counting of the same neutron is carefully avoided, if the neutron re-enters the volume after multiple scattering from the surrounding. The relative contributions of different muon interaction processes to secondary neutron production for Set 1b and Set 2b are shown in Figure 4.8. It is observed that μ^--capture in the shield volume is the dominant mechanism, while contribution from e^+/e^--nuclear interactions is negligibly small. The contributions from muon nuclear interactions, pion inelastic scattering and hyperon capture (processes 4, 8-10 in Figure 4.8) are significantly enhanced in Set 2b. For all four sets, nearly $\sim 90\%$ of the neutrons are produced in the Pb shield. For the average vertical thickness in the present geometry, this implies a neutron production rate of $1.45 \times 10^{-4} n/gcm^{-2}/\mu$. The effect of the presence of the concrete layers in the laboratory building was also tested in the simulations. A concrete slab of 5 m$\times$ 5 m$\times$ 30 cm was placed 2.5 m above the the top layer of Pb. The generator plane was placed above the concrete layer, at z = 3.5 m. Figure 4.9 shows the Z-coordinates of the neutrons produced for the configurations with and without concrete. Though the overall neutron production increased in presence of the concrete slab, neither the neutron yield nor the energy spectrum of neutrons in the shield volume originating from the triggered muons was affected due to the inclusion of the concrete.
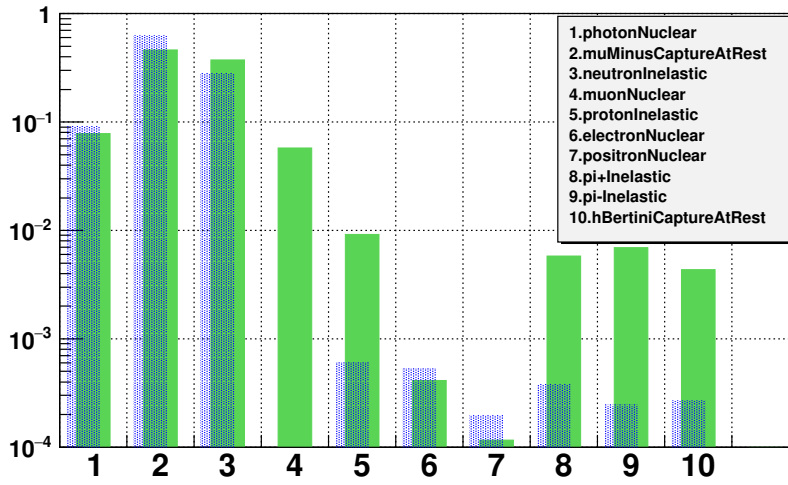
FIGURE 4.8: Relative contributions of different muon interaction processes to the secondary neutron production in Cu+Pb shield of TiLES, simulated with GEANT4.10.00 (dotted bars) and GEANT4.10.05 (solid bars)
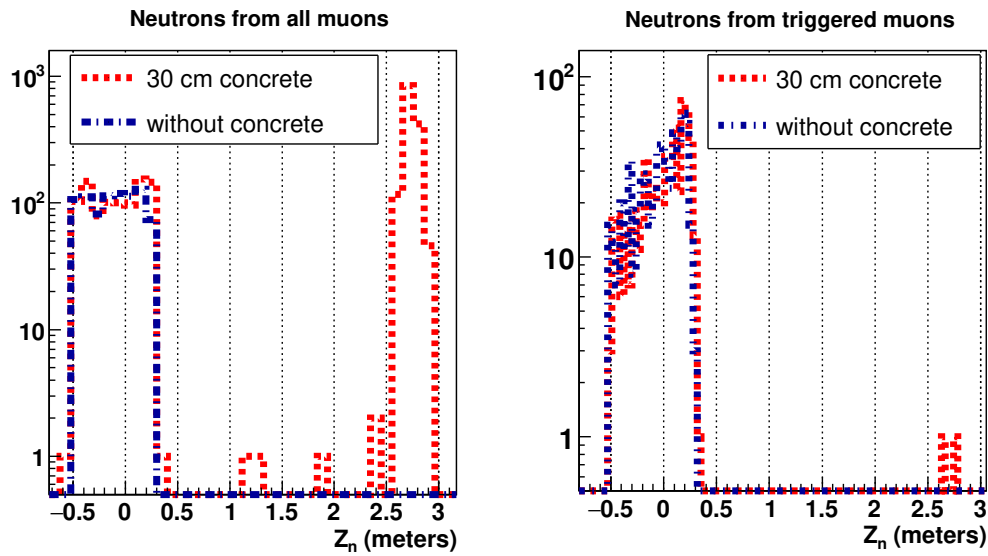
FIGURE 4.9: The Z coordinate of neutron production for simulations with and without concrete. The concerete slab is of 30 cm thickness. The left panel shows the neutrons generated from all the muons and the right panel shows the neutrons from the muons that satisfy the trigger. The increase in the number of neutrons from triggered muons is only about 0.3% after the placement of concerete.
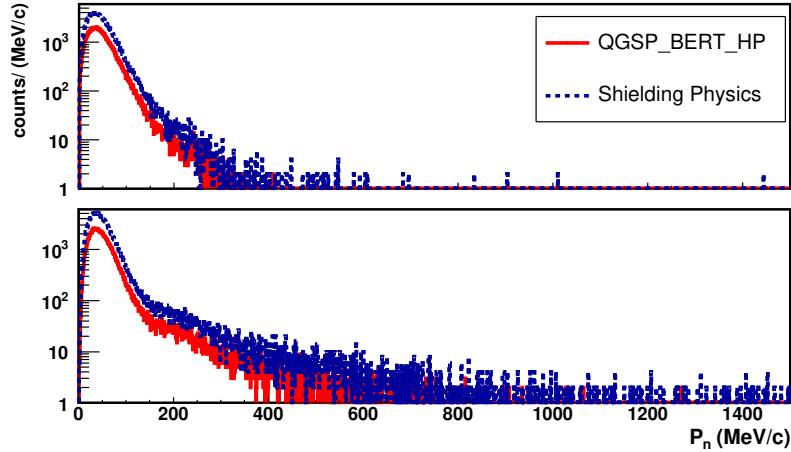
FIGURE 4.10: Simulated momentum distributions of the secondary neutrons for two different physics cases in GEANT4.10.00 (top panel) and GEANT4.10.05 (bottom panel). Shielding Physics is scaled by a factor of two for better visibility

The striking difference in the momentum distribution of neutrons simulated in GEANT4.10.00 and GEANT4.10.05 is evident from Figure 4.10, with latter exhibiting much harder spectrum. The yield of low energy neutrons (0-50 MeV/c) is also about 13% higher in Set 2b as compared to Set 1b. However, for a given GEANT4 version, neutron momentum distributions are similar for the QGSP_BERT_HP and the Shielding Physics list. It is observed that the momentum distribution of neutrons does not show strong dependence on Pb or Cu volume and hence is described by a common empirical fit function for the entire shield volume. The average momentum obtained in Set 1 and 2 are ∼ 47.5 MeV/c and ∼ 55 MeV/c, respectively. As mentioned earlier, the neutron momentum distributions of Set 1 and Set 2 have been fitted to empirical functions given in Eq. 1 and 2, respectively, as below:

$$\frac{dN(P_n)}{dP_n} = a_0.e^{a_1.P_n}.sinh(a_2.\sqrt{P_n}) + a_3.P_n.e^{a_4.P_n} \qquad (4.1)$$

$$\frac{dN(P_n)}{dP_n} = a_0.e^{a_1.P_n}.sinh(a_2.\sqrt{P_n}) + a_3.P_n.e^{a_4.P_n} + a_5 \qquad (4.2)$$

A typical fit to the simulated neutron spectrum for Set 2b is shown in the Figure 4.11. The fit parameters are listed in Table 4.1. The neutron multiplicity for different sets are also given in Table 4.1. The neutron multiplicity (N_n/N_μ) varies between 0.111 to 0.126 and is ∼ 13% higher in Set 2 as compared to the Set 1.
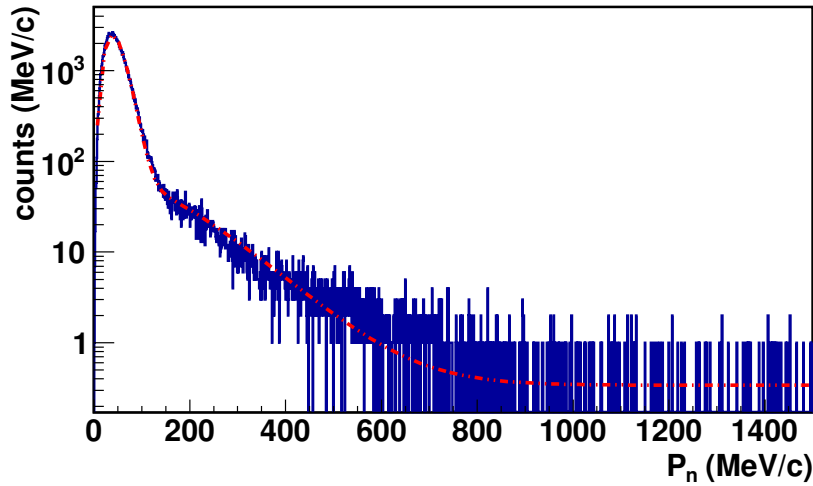
FIGURE 4.11: Momentum distribution of the secondary neutrons (Set 2b) together with the empirical fit function (dashed line)

It should be mentioned that the neutron momentum (P_n) distribution was found to be isotropic and independent of vertical position (Z) within the production volume. The position distribution was also found to be nearly uniform

TABLE 4.1: Empirical fit parameters for neutron momentum distribution

Fit parameter	GEANT4.10.00		GEANT4.10.05	
	QGSP_BERT_HP	Shielding Physics	QGSP_BERT_HP	Shielding Physics
a0	46.86± 1.70	49.21± 1.89	4.119±0.185	3.773±0.171
a1 $((MeV/c)^{-1})$	-0.1345±0.001	-0.1339±0.0011	-0.1869±0.0011	-0.1889±0.0011
a2 $((MeV/c)^{-0.5})$	1.537±0.012	1.524±0.013	2.30±0.01	2.329±0.014
a3	3.428±0.322	3.618±0.351	1.762±0.079	1.72±0.07
a4 $((MeV/c)^{-1})$	-0.02098±0.00044	-0.02119±0.00046	-0.01271±0.00019	-0.01238±0.000018
a5 $((MeV/c)^{-1})$	–	–	0.2859±0.023	0.341±0.025
N_n/N_μ	0.111±0.006	0.111±0.006	0.125±0.006	0.126±0.006

in X-Y-Z. Hence, the secondary neutrons are distributed uniformly in the shield volume for γ-ray production. The simulated neutron momentum distributions projected for individual process of secondary neutron production is shown in Figure 4.12.
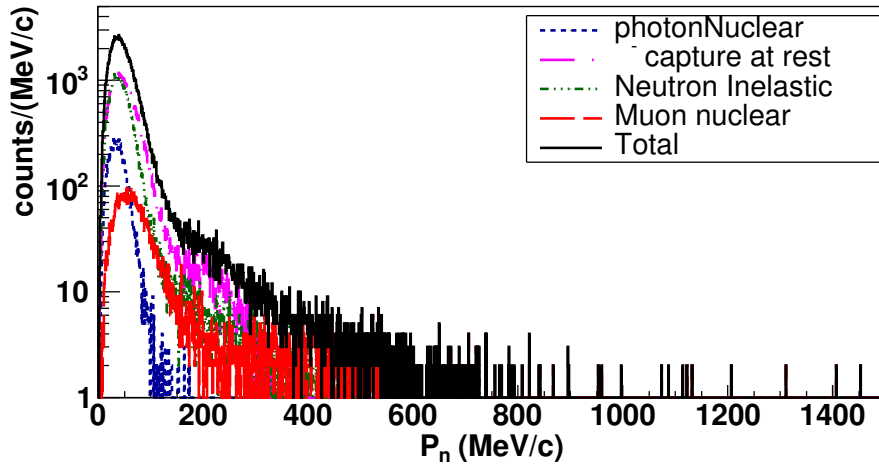
FIGURE 4.12: Momentum distribution of the secondary neutrons for dominant process (Set 2b)

4.2.2 Gamma production from secondary neutrons

Neutrons are generated within the TiLES shield volume from the empirical momentum and spatial distribution obtained in Section 4.2.1. The relative

fraction for neutrons in Pb to Cu is taken to be 90:10, as obtained from simulations in Section 4.2.1. Fast neutrons can interact with nuclei via different mechanisms such as $(n, n'\gamma)$, (n, γ), (n, α) etc. Charged particles (due to their short range) do not contribute to energy deposition in the HPGe detector, except when production takes place within the Ge volume. The present study focused on the measurement of characteristic γ-rays of Cu and Ge via $(n, n'\gamma)$. Natural isotopic composition of both Cu and Ge are used in the simulation. In each Set, $1.5 - 2 \times 10^8$ neutron events were generated to obtain γ-ray yield comparable to the experimental data. The excited states upto 5 MeV for ^{63}Cu, 8.5 MeV for ^{65}Cu, and 8 MeV for ^{208}Pb are considered from the default version of library (G4ENSDFSTATE2.2). Hence, even though the experimental γ-ray spectrum range is limited to 5 MeV, the simulated spectra are generated upto 10 MeV to get an estimate of the contribution of high energy γ rays. It should be noted that the γ-ray peak centroid energies are found to vary within 1-2 keV of the reference values of NNDC [129].

The resolution function R(E) was derived from the experimentally measured energy resolution (FWHM/E) over 100 to 2615 keV range as

$$R(E) = \frac{P_0}{E^{0.73}} \tag{4.3}$$

with $P_0 = 0.430 \pm 0.003$. For each event, first the energy deposited in the HPGe detector is obtained. This energy is then randomized with a Gaussian distribution of energy dependent FWHM given by Eq. 4.3 and is recorded. In Ref. [14] it is shown that the photopeak efficiency as well as the overall line shape of γ-rays is well reproduced using the optimized TiLES HPGe detector model, employed in the present simulations. It should be mentioned that in the present

two step simulation approach (i.e. muon to neutron and neutron to gamma), the contribution of muons to the background in the HPGe spectrum is not taken into account.

The generated γ-ray spectra of Set 1b and Set 2b in the range 500-1700 keV are shown in Figure 4.13, where lines of interest of Ge and Cu are visible. The fast neutron scattering in the Ge gives rise to nuclear recoils in addition to the γ ray emission from nuclear de-excitation. As it is well known, this recoil distribution is responsible for the broad nature of the neutron inelastic scattering peaks in Ge, which is visible in both experimental and the simulation spectra. The $(n, n'\gamma)$ yield in Ge are found to be similar in both sets, but the line shape of the recoil tail is better reproduced in Set 2b. (shown in Figure 4.14.)

The $\text{Cu}(n, n'\gamma)$ yield are strongly enhanced in the Set 2b. Similar to neutron spectra, no significant differences are seen in the γ ray spectra for two physics lists in a given GEANT4 version. Hence, for comparison with experimental data, only simulations with the Shielding Physics list are considered.

In a previous work done by Boswell *et al.* [130], the level deexcitation cross sections were extracted from the γ production cross section for energy levels in Cu. These measurements were compared with the ENDF/B-VII evaluation for level excitation cross section of discrete levels. The ENDF/B-VII level cross sections do not include feeding from higher lying levels in the measured cross sections and nuclear model calculations. The comparison of the measured and ENDF/B-VII data is given in Figure 4.15. The figures are adapted from [130].
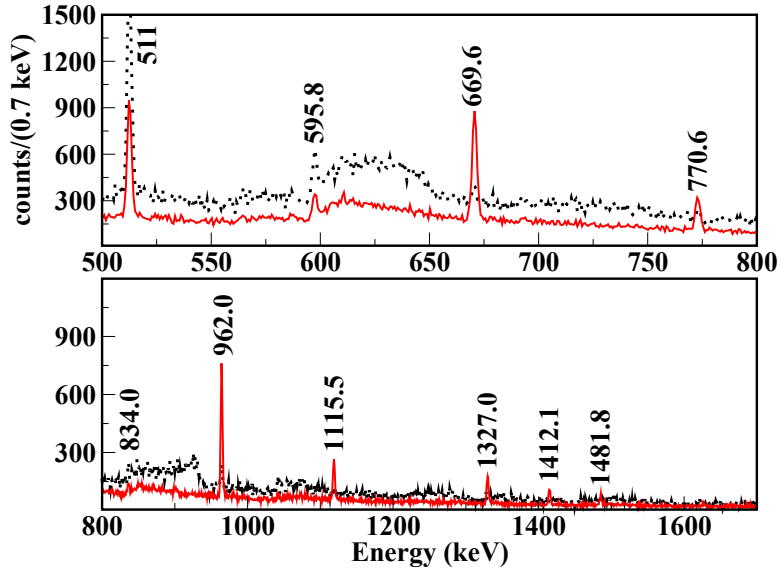
FIGURE 4.13: A comparison of simulated γ-ray spectra generated with GEANT4.10.00 (black, dotted, scaled up by a factor of two for better visibility) and GEANT4.10.05 (red, solid) ($N_{inc}(n)= 1.435 \times 10^8$)
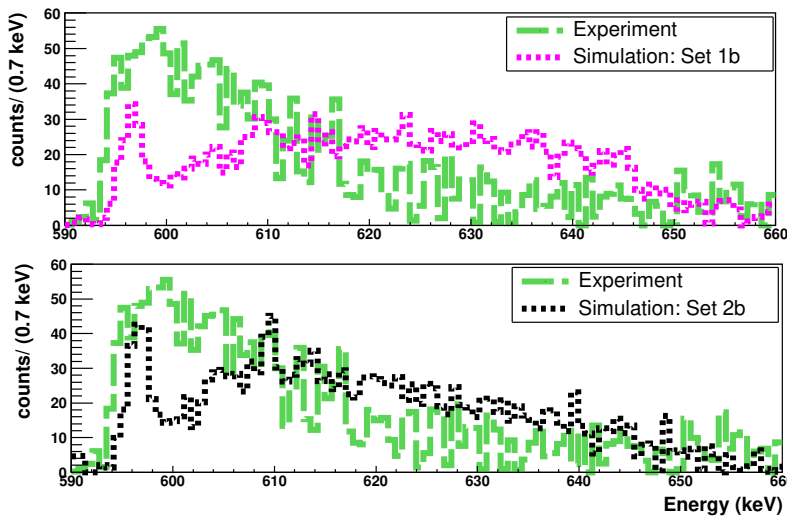
FIGURE 4.14: A comparison of the lineshape of the 595 keV for the experimental and the simulated data. The spectrum is background subtracted and the total counts are normalized to the counts in the experimental peak.
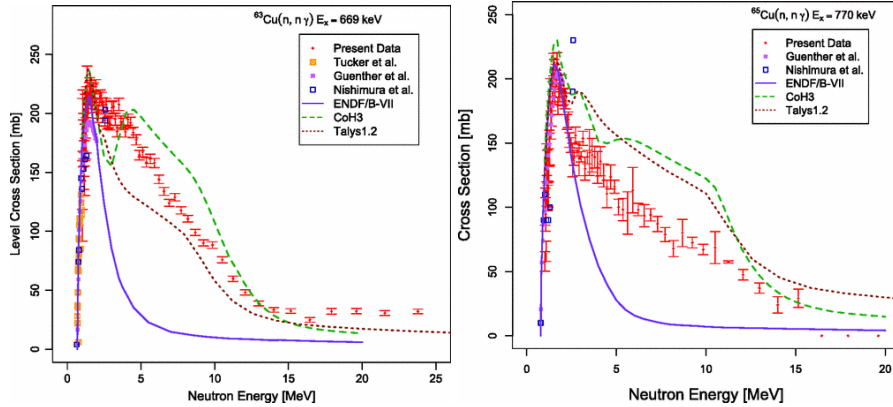
FIGURE 4.15: The total γ-ray production cross section for the first excited level in ^{63}Cu (E_γ = 669 keV) and ^{65}Cu (E_γ = 770 keV). The experimental data is also compared with other measurements and model calculations. The Figures are adapted from [130]. The present data legend in the figure corresponds to the experimental data in the reference.

The underestimation of the γ ray yield in the simulations using GEANT4.10.00, ENDF/B-VII, may possibly due to the non inclusion of feeding from the higher lying levels in Cu.

4.3 Comparison of simulation and experimental results

Intensities of γ rays of interest are extracted from both measured and simulated spectra and are normalized to the incident muon counts for comparison. It should be noted that the measured γ-ray multiplicity is specific to the experiment geometry. In the present analysis, the choice of γ rays was restricted by measurable intensities above the background in the experimental spectrum to minimize the fitting errors. Given the broad line shapes in Ge, only 595.8 keV γ-ray of ^{74}Ge having highest intensity is considered, whereas in case of ^{63}Cu and ^{65}Cu yield of multiple prominent γ rays are used for comparison.

TABLE 4.2: A comparison of measured and simulated $(n, n'\gamma)$ yield of Ge and Cu.

Reaction	γ-ray Energy	N_γ/N_μ (10^{-7})		
	(keV)	Experiment	Simulations	
			Set 1b	Set 2b
$^{74}Ge(n, n'\gamma)^{74}Ge$	595.8	75±8	63±4	72 ± 4
$^{63}Cu(n, n'\gamma)^{63}Cu$	669.6	16±2	1.3±0.2	24 ± 2
$^{63}Cu(n, n'\gamma)^{63}Cu$	962.0	22±5	1.6±0.3	26 ± 2
$^{63}Cu(n, n'\gamma)^{63}Cu$	1326.8	7 ±3	< 0.7	6.1 ± 0.5
$^{65}Cu(n, n'\gamma)^{65}Cu$	770.64	8±2	< 1	7.4±0.6
$^{65}Cu(n, n'\gamma)^{65}Cu$	1115.6	9±3	< 0.5	8.5 ± 0.6

For the experimental data, the intensities of the γ-rays are extracted from the coincident γ-ray spectrum gated on the prompt time window (see Figure 4.5), by fitting a Gaussian+quadratic background function over the energy window of interest in LAMPS (Linux Advanced Multi-Parameter System) analysis software [131]. The chance correction is obtained from the integral counts in the same energy window from the chance gated spectrum, with appropriate normalisation. As mentioned earlier, $Ge(n, n'\gamma)$ peaks are broad and extraction of area needs to be done with proper care. To ensure the robustness, the yield of 595.8 keV γ-ray of $Ge(n, n'\gamma)$ was extracted by two independent methods - (i) extracting the background with in-built background function of ROOT and manually subtracting this background from integral counts in the region of interest, and (ii) by using a Gaussian with right exponential tail +quadratic background function in Lamps. The extracted intensity from two different methods agrees within fitting errors (~ 10%).

From the simulated spectra, the γ-ray multiplicity per muon, i.e., N_γ/N_μ is calculated as:

$$\frac{N_\gamma}{N_\mu} = \frac{N_\gamma}{N_n} \times \frac{N_n}{N_\mu} \qquad (4.4)$$

Table 4.2 shows a comparison of the γ-ray multiplicity per muon for the experiment and simulation data Sets 1b and 2b (i.e. two different GEANT4 versions with the Shielding Physics list). All the listed γ rays correspond to the transitions to the ground state. It is evident that measured ^{74}Ge$(n, n'\gamma)^{74}$Ge yield agrees well with both simulation data sets, but the scenario for Cu$(n, n'\gamma)$ is vastly different. The simulations with GEANT4.10.00 (Set 1b) under-predict the production of γ rays in ^{63,65}Cu almost by an order of magnitude (a factor of 10-15), while those with GEANT4.10.05 (Set 2b) show very good agreement with data. In Set 1b, wherever the Cu γ-ray peaks were not visible, the upper limit has been estimated with Currie formula [19]. For most of the ^{63,65}Cu γ-rays, the observed gamma multiplicity is consistent with Set 2b simulations within errors. However, the simulated multiplicity of one of the γ-rays of ^{63}Cu, (669.6 keV) is about 50% higher than the data. Additionally, a few γ-rays of ^{63,65}Cu having multiplicity $\sim 1 - 4 \times 10^{-7}$ are visible in the simulated spectra (indicated in Figure 4.13), but the corresponding expected intensity in the measured spectra is below the experimental detection limit. It may be pointed out that the measured γ multiplicity is not only dependent on the shield material, but also depends on the experiment geometry.

A simple order of magnitude estimate of the average muon induced fast neutron flux, $\langle N_n \rangle$, can be obtained using an average neutron inelastic scattering cross section, $\langle \sigma \rangle$, in the neutron energy range of 1 - 20 MeV as

$$\langle N_n \rangle = \frac{N_\gamma}{\langle \sigma \rangle \times N_T \times \epsilon_\gamma \times I_\gamma} \qquad (4.5)$$

where N_γ is the photopeak intensity per unit time, ϵ_γ is the simulated photopeak efficiency for a volume source corresponding to the copper shield, I_γ is the branching ratio, N_T is the number of target atoms for the isotope of interest. The average neutron flux is estimated to be $7(2) \times 10^{-5}$ neutrons $cm^{-2}s^{-1}$ from the lowest energy transitions in ^{63}Cu and ^{65}Cu isotopes.

Figure 4.16 shows the simulated γ-ray energy spectra (Set 2b) above 2 MeV. It is important to note the presence of high energy γ rays arising from Pb - ^{208}Pb$(n, n'\gamma)^{208}$Pb (2614.5, 7913 keV), ^{206}Pb$(n, n'\gamma)^{206}$Pb (7063 keV) and from Ge - ^{76}Ge$(n, n'\gamma)^{76}$Ge (2023.3, 2782.7 keV). The estimated γ multiplicity per muon is rather small $(0.4 - 0.8 \times 10^{-7})$ due to lower photopeak efficiency of the HPGe detector at higher energy, but the contribution of the Compton tail of these high energy γ-rays to lower energy of interest (2- 2.5 MeV) can be a significant factor in rare decay studies. As mentioned earlier, the muon energy and interactions are different in underground setups as compared to the sea level, but fast neutron induced reactions in Pb can significantly contribute to the background. The Cu material is an integral part of cryogenic detectors used in rare decay studies and hence the muon induced $(n, n'\gamma)$ data for Cu is important for understanding the background. Further, the present $(n, n'\gamma)$ data in Ge and Cu provides a crucial input towards validation of GEANT4 simulation of both muon induced neutron production and neutron inelastic scattering. It may be pointed out that even though simulations have shown significant improvement, the measurement of high energy γ rays from muon/neutron induced reaction is essential for the assessment of the cosmic muon induced contribution to the background.
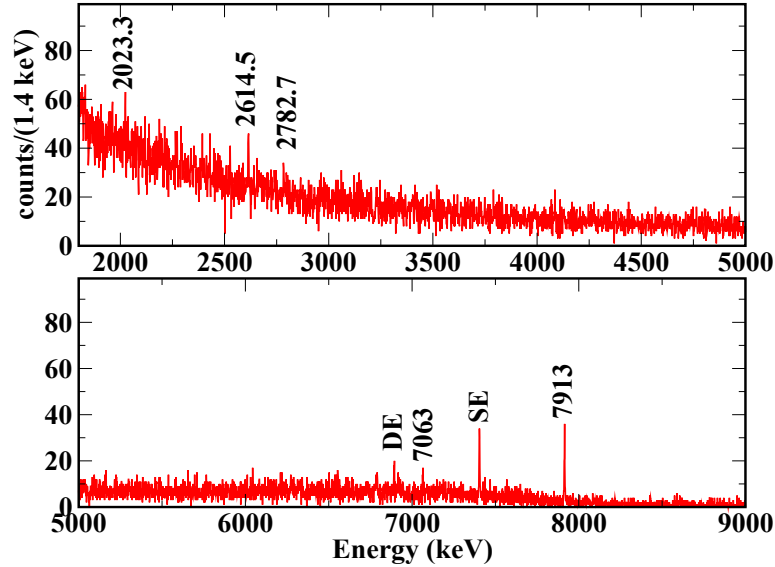
FIGURE 4.16: Simulated γ-ray spectra (Set 2b) showing high energy γ rays (E>2 MeV), single/double escape (SE/DE) of 7913 keV γ-ray are also indicated.

4.4 Summary

The contribution to the γ-ray background arising from cosmic muon induced fast neutrons has been directly measured in the TiLES low background setup. Neutrons are produced in the Pb-Cu composite shield of TiLES. The resultant γ rays produced via $(n, n'\gamma)$ reactions in Ge and Cu is measured. The Cu material is an integral part of cryogenic detectors used in rare decay studies and hence the muon induced $(n, n'\gamma)$ data for Cu is very important. The experimental results are compared with Monte Carlo simulations using GEANT4 simulation toolkit for two different versions of GEANT4(10.00 and 10.05), each with two different Physics lists, QGSP_BERT_HP and Shielding Physics. While GEANT4.10.00 significantly under-predicts the γ-ray production in Cu, reasonably good agree-

ment with the experimental data is obtained with GEANT4.10.05. The dominant process contributing to the neutron production at the sea level is the capture of negative muons, which accounts to more than 50% of the neutrons produced from the cosmic muon interactions. The lineshape of the peak arising from neutron inelastic scattering in Ge is also better predicted in GEANT4.10.05. It is shown that the neutron energy spectrum has no strong dependence on these physics lists, but does shows variation in two GEANT4 versions. The simulations have further shown the presence of several high energy γ rays in the range 2-8 MeV and the contribution of the Compton tail of these high energy γ-rays to lower energy of interest (2-2.5 MeV) is a background of concern in rare decay studies. Measurements of high energy γ rays from muon/neutron induced reactions is necessary for the assessment of the actual background.

Thermal neutron induced γ ray background in ^{124}Sn

Introduction

Thermal neutron induced γ-ray background in ^{124}Sn is investigated in connection with neutrinoless double beta decay ($0\nu\beta\beta$) studies in ^{124}Sn. Thermal neutron capture reactions are extremely important as a source of background in $0\nu\beta\beta$ studies. The capture of neutrons in the detector fiducial volume can lead to nuclear excitation. The resultant nuclear de-excitation can proceed with successive β and γ decays, which leads to the direct energy deposition in the detector, leading to significant deterioration of the background levels. In this regard, the study of thermal neutron capture reactions in ^{124}Sn is important for the TIN.TIN experiment. For this purpose, enriched ^{124}Sn sample was irradiated with thermal neutron fluence of 3×10^{15}/cm^2, in Dhruva reactor at BARC, Mumbai. The gamma ray spectra of the irradiated sample were measured in low background counting setup to study both long and short lived activities. Simulations are

performed using GEANT4 [16, 17] toolkit to estimate the contribution to the observed photopeak intensities of these γ rays from the coincidence summing effect. Impact of the observed high energy gamma-rays and the residual activity due to ^{125}Sb, on the background in the region of interest around of $Q_{\beta\beta}$ value of ^{124}Sn ($\sim$ 2.291 MeV) is discussed. The background contribution arising from thermal neutrons to the region of interest (ROI) for $0\nu\beta\beta$ in ^{124}Sn is evaluated from the reactor thermal neutron flux. Based on the observed background in the ROI, the maximum neutron dose to which the Tin detector material can be exposed to be able to achieve the desired background levels, is estimated.

5.1   Neutron capture in ^{124}Sn

A ^{124}Sn sample ($4\,\text{mm} \times 4\,\text{mm} \times 0.2\,\text{mm}$, 23.3 mg) having 99.26% enrichment (procured from ISOTOPE JSC, Russia), is used for the present irradiation. The traces of other tin isotopes were measured to be less than 20 ppm and metallic impurities were estimated to be less than 5 ppm, using secondary ion mass spectroscopy (SIMS) measurements. The natural isotopic abundance of ^{124}Sn is 5.79%.

It can be seen that the Q value of beta decay of ^{125}Sn is larger than $Q_{\beta\beta}(^{124}$Sn$)$ = 2.2911±0.0015 MeV [10] and hence is a potential source of background. In addition, several γ rays are generated in the decay of ^{125}Sn and ^{125}Sb. Verma *et al.* [132] have reported detailed gamma ray measurements in ^{124}Sn(n,γ) reaction, including those with very weak branching ratios. As per the available spectroscopy data [18], gamma rays in the energy range 1.5-2.275 MeV can be emitted in this decay chain with upto 1.9% branching ratio. These high energy gamma-rays are of concern, as they can adversely affect the sensitivity of the
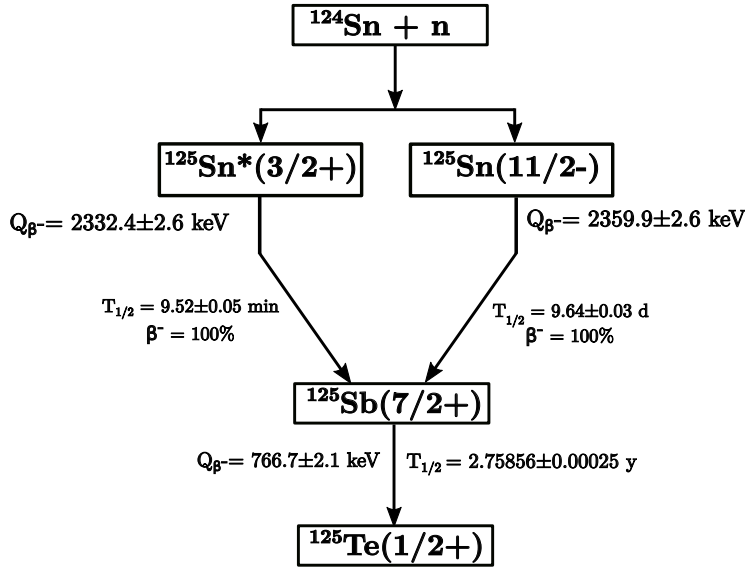
FIGURE 5.1: Schematic presentation of n-capture of ^{124}Sn and subsequent β^- decay.

$0\nu\beta\beta$ measurement in ^{124}Sn. As shown in Figure 5.1, ^{125}Sn*($\frac{3}{2}^+$, $T_{1/2}$ = 9.52 min) and ^{125}Sn ($\frac{11}{2}^-$, $T_{1/2}$ = 9.64 d) are populated in thermal n-capture reactions with cross-sections of 130 mb and 4 mb, respectively [18].

Prior to irradiation, radiopurity of the pristine ^{124}Sn sample was studied in the TiLES low background counting setup [14] for ~14 days (see Figure 5.2) and no additional gamma rays were observed above the background level within the measurement sensitivity of TiLES. In particular, the background in the region of interest (ROI) close to $Q_{\beta\beta}(^{124}$Sn) was found to be similar to the ambient background.

Thermal n-capture by ^{124}Sn leads to ^{125}Sn that decays to ^{125}Sb, which further decays to ^{125}Te. The schematic reaction and decay processes are shown in Figure 5.1. It should be mentioned that n-capture can lead to population of excited states of ^{125}Sn (upto 5.7335 MeV [133]). However, all these states decay predominantly by gamma ray emission either to $\frac{3}{2}^+$ or to $\frac{11}{2}^-$ states.
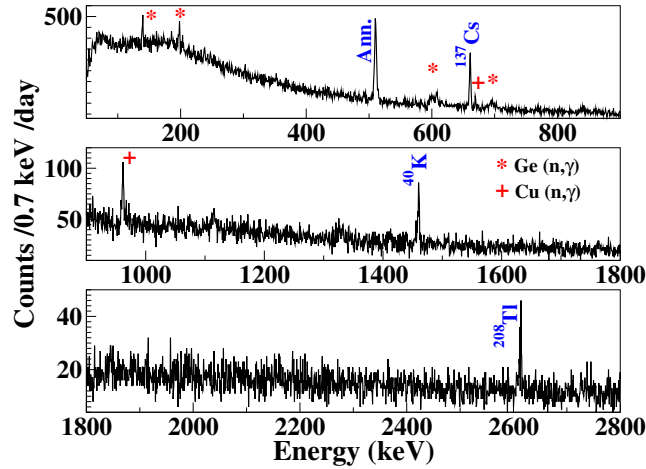
FIGURE 5.2: The gamma ray spectrum of ^{124}Sn before irradiation.

5.2 Thermal neutron irradiation and γ ray measurements

The ^{124}Sn is irradiated with thermal neutrons at Dhruva reactor at BARC, Mumbai, with thermal neutron flux of 5×10^{13} n/cm^2/sec for 1 min. Both short lived and long lived activities are studied ($\sim$10 min-550 days) in the low background counting setup. Identification of gamma rays was confirmed by measurement of half-life. The gamma ray spectrum of the irradiated sample was measured immediately after the irradiation (cool down time (t_c) $\sim$ 10 min) with a standard HPGe detector ($\sim$ 30% relative efficiency) at 10 cm and is shown in Figure 5.3. The intense peak arising from the short lived ^{125}Sn($\frac{3}{2}^{+}$) is clearly visible at 331.9 keV. The half-life of 331.9 keV γ ray was measured to be 10.01(8) min (see Figure 5.3b), which is consistent with the literature value [18]. No additional short lived impurities were observed in the spectrum.
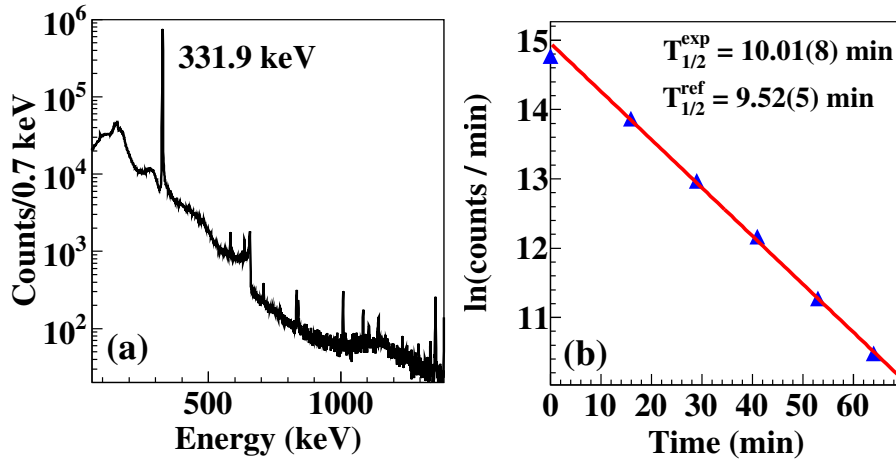
FIGURE 5.3: (a) The gamma ray spectrum of irradiated ^{124}Sn after t_c = 10 mins. ($T_{counting}$= 1 min) and (b) The decay curve of E_γ = 331.9 keV (^{125}Sn*, $\frac{3}{2}^+$)

The irradiated sample was then transported to TIFR and the gamma ray measurements were mainly done in TIFR Low background Experimental Set-up (TiLES) [14]. The data analysis is done using LAMPS (Linux Advanced MultiParameter System) [131]. Energy calibration of TiLES is done using standard ^{152}Eu source and is monitored with known background lines over energy range of 120-2615 keV. The energy resolution of detector is ~2.6 keV at 1408 keV. The dead time is measured using 10 Hz pulser and is estimated to be ~0.1%. The setup also has a provision for counting a sample in a close geometry with higher efficiency. The detector efficiency in close counting geometry is estimated using Monte Carlo simulations with GEANT4 [16, 17] for the optimized model of the detector. In Ref. [14], it is shown that the photopeak efficiency as well as the overall line shape of γ rays is well reproduced using the optimized TiLES HPGe detector model, employed in the present simulations. The energy spectra were recorded at a distance (*l*) of 12 cm from the detector face to minimize the coincident summing effect and in close geometry (*l*~1-5 cm) for measurement

of background in ROI due to summing.
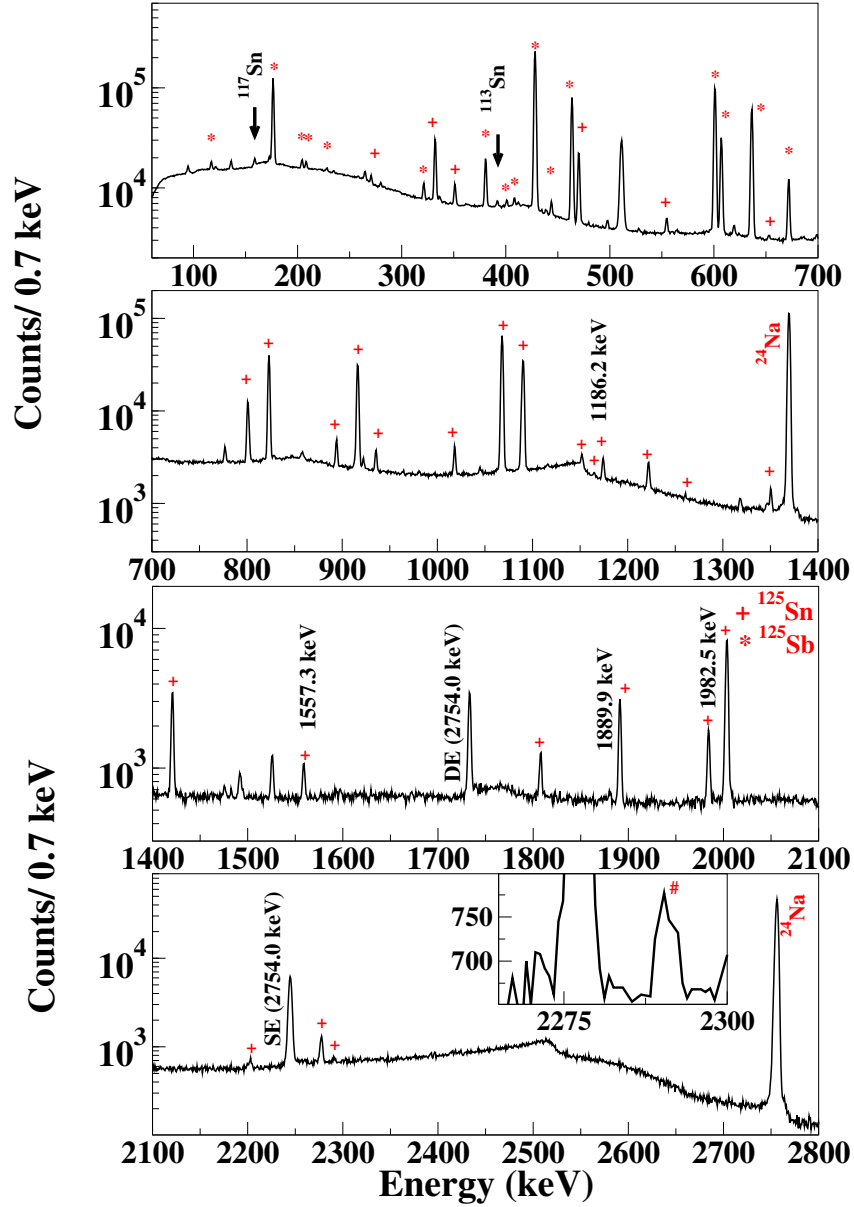
FIGURE 5.4: The gamma ray spectrum of the irradiated ^{124}Sn after t_c ~1 day in TiLES
(l= 9 mm, $T_{counting}$ = 16.3 h, SE: Single Escape, DE: Double Escape). Inset
shows expanded view of ROI and sum peak (#) at 2288.2 keV

The intensities of gamma rays are extracted from spectra at l=12 cm. The

identification of various gamma rays was further confirmed by tracking the half-

life of individual gamma rays. A typical spectrum is shown in Figure 5.4, where gamma rays from decay of ^{125}Sn and ^{125}Sb are indicated. An inset in the bottom panel shows expanded view of 2250-2300 keV, where peak at 2288.2 keV is visible. This peak arises purely from the coincidence summing effects and its impact for the background in the ROI for $0\nu\beta\beta$ in ^{124}Sn is discussed in section 5.5.

5.3 Measurement of γ ray activity

The observed gamma rays from the decay of ^{125}Sn ($\frac{11}{2}^{-}$) and ^{125}Sb are listed in table 5.1 and 5.2, respectively. For ^{125}Sn*($\frac{3}{2}^{+}$), all gamma rays other than 331.9 keV have much lower intensities (see Fig. 5.3) [18]. The measured intensity relative to the most dominant gamma-ray i.e. 1067.1 keV for ^{125}Sn and 427.9 keV for ^{125}Sb, extracted from l=12 cm data are also listed in the Table 5.1 and 5.2, respectively. Errors are computed by fitting the gaussian peak and the background. Fitted peak centroids are within $\pm$ 0.5 keV of the corresponding Ref. [18] values. The typical fitting and calibration uncertainties on the gamma ray energy is of the order of 0.5 keV in our measurements. Additionally, γ rays corresponding to ^{24}Na, which arise due to ^{27}Al(n,α) reaction are also observed. However, origin of the aluminum could not be ascertained. The Compton background arising from ^{24}Na and other high energy gamma rays was the main limiting factor for measurement of weaker decay branches and gamma rays with intensities less than ~0.04% could not be observed at l=12 cm. The present measurement has also resulted in more accurate value of $T_{1/2}$ = 9.63(2) d for ^{125}Sn ($\frac{11}{2}^{-}$) as shown in Figure 5.5.
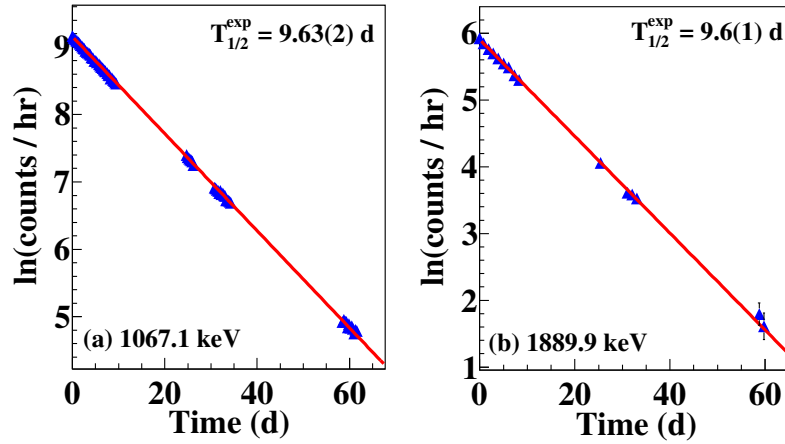
FIGURE 5.5: Decay curves for different gamma-rays produced in the decay of ^{125}Sn (a) 1067.1 keV, (b) 1889.9 keV ($T^{\text{ref}}_{1/2}$ = 9.64(3) d).

TABLE 5.1: Observed gamma rays from the decay of ^{125}Sn($\frac{11}{2}^{-}$, $T^{\text{ref}}_{1/2}$ = 9.64(3) d) together with measured intensity (I_r) relative to the intensity of 1067.1 keV.

Energy (keV)	I_r (%) (Measured)	I_r (%) (Ref.)	Energy (keV)	I_r (%) (Measured)	I_r (%) (Ref.)
270.6	1.8(3)	1.10(2)	1163.8	-	0.32(2)
332.1	14.1(4)	14.5(3)	1173.3	2.5(6)	1.87(4)
351.0[1]	9.7(6)	2.72(5)	1186.2	-	0.09(1)
469.9	15.9(2)	15.3(3)	1220.9	2.4(5)	2.76(6)
563.0	-	0.16(2)	1349.4	0.7(4)	0.61(2)
652.6	-	0.42(1)	1419.7	4.6(5)	5.02(10)
800.3	10.0(9)	11.00(22)	1557.3	-	0.042(10)
822.5	43(1)	44.1(9)	1591.4	2.3(9)	0.26(2)
893.4	3.8(7)	3.0(1)	1806.7	1.8(5)	1.53(3)
915.6	40(1)	42.6(9)	1889.9[3]	1.8(7)	0.76(4)
934.6	2.8(4)	2.15(4)	1982.5	-	0.033(10)
1017.4	2.8(6)	3.30(7)	2002.1	20(1)	19.8(4)
1067.1	100.0(2)	100	2201.0	-	0.40(2)
1089.2[2]	56(2)	12.3(2)+47.3(9)	2275.7	2.2(6)	1.88(4)
1151.2	1.2(4)	1.18(2)			

[1] Mixed with 351.9 keV gamma-ray of the ambient background (^{214}Pb decay).

[2] Composite of 1087.7 keV and 1089.2 keV, which could not be resolved.

[3] Intensity affected by coincident summing, see text for details

TABLE 5.2: Observed gamma rays from the decay of ^{125}Sb together with measured intensity (I_r) relative to the intensity of 427.9 keV.

Energy (keV)	I_r (%) (Measured)	I_r (%) (Ref.)
117.0	1.0(4)	0.887(9)
176.3	21.1(7)	23.11(5)
204.1	1.3(4)	1.070(21)
208.1[1]	1.2(4)	0.837(14)
227.9	-	0.443(6)
321.0	1.3(2)	1.404(9)
380.5	5.6(4)	5.124(19)
402.0	-	0.021(2)
408.1[2]	1.1(1)	0.623(6)
427.9	100(1)	100
443.6	0.8(3)	1.035(6)
463.4	36.1(6)	35.45(10)
600.6	58(1)	59.62(16)
606.7	16.2(8)	16.83(6)
636.0	38.3(9)	37.9(3)
671.4	6.7(4)	6.049(19)

[1] Mixed with 209.3 keV gamma-ray of the ambient background (^{228}Ac decay).
[2] Mixed with 409.5 keV gamma-ray of the ambient background (^{228}Ac decay).

5.4 Coincidence summing contribution for $E_\gamma > 1$ MeV

Observed intensities of most of the gamma rays from the decay of ^{125}Sn and ^{125}Sb are consistent with reference values, except for very weak ($< 0.1\%$) high energy gamma-rays like 1889.9 keV. From the measured $T_{1/2}$ of 1889.9 keV, which is in very good agreement with the reference value [18], it is evident that this peak arises from the ^{125}Sn decay and does not have extraneous contribution. As mentioned earlier, depending on the detector geometry, the measured intensity of high-energy gamma-rays can be affected by coincident summing of multiple

gamma rays in a cascade. A partial decay scheme of ^{125}Sb, populated in the decay

of ^{125}Sn, is shown schematically in the Figure 5.6. A list of possible pathways of
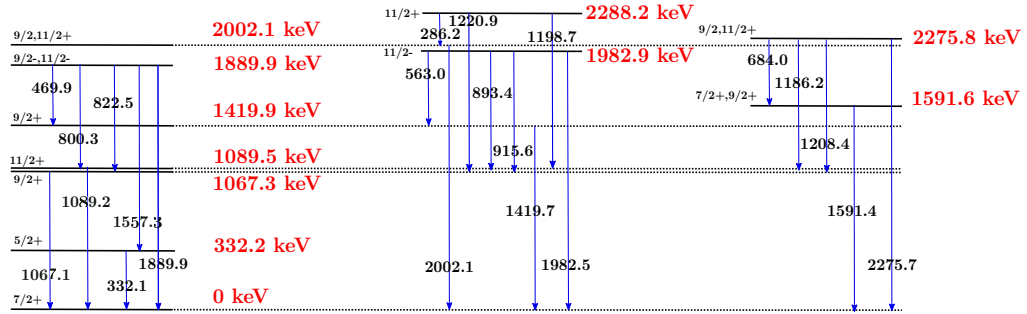
FIGURE 5.6: A partial level scheme of ^{125}Sb, populated in the beta decay of ^{125}Sn.

coincident summing of two gamma rays in a cascade resulting in a high energy

photopeak is shown in Table 5.3 for few energies of interest. The probability P_0

for the photopeak detection of a direct γ_0 transition with branching ratio I_{γ_0} and

detector efficiency ϵ_0, can be given as $I_{\gamma_0}\epsilon_0$. A simple estimation of coincident

summing probability P_{12} of two gamma rays (γ_1, γ_2) in a given cascade to the

photpeak of E_{γ_0} ($=E_{\gamma_1}+E_{\gamma_2}$), is carried out using GEANT4 simulations [16, 17].

The simulations employ the optimized TiLES detector [14] geometry with

a distributed source of sample size (4 mm × 4 mm) at a distance l from the

detector face. An event consists of two components: i) generation of the first

gamma-ray in the cascade with energy E_{γ_1}, ii) generation of the second gamma-

ray with energy E_{γ_2} with a probability f_{γ_2}, which is the partial branching ratio of

γ_2 emission from the corresponding level. Both these gamma rays are tracked in

the detector and energy deposited is recorded for $N_{s0}=10^7$ events. The gamma

rays are emitted isotropically, neglecting angular correlations. The summing

fraction is obtained from the N_{sum}- intensity of the peak corresponding to E_{γ_0} in

the simulated spectrum, as

$$P_{sum} = N_{sum}/N_{s0} \tag{5.1}$$

The probability of summing contribution to the photopeak of E_{γ_0} is then calculated as

$$P_{12} = I_{\gamma_1} P_{sum} \tag{5.2}$$

where, I_{γ_1} is the branching ratio of γ_1. Table 5.3 lists the simulated summing probability P_{12} at l=12 cm and 1 cm together with the corresponding P_0. It is evident that for 1889.9 keV the coincident summing contribution is significant ($\sim$ 50%) even at 12 cm distance and results in the higher observed intensity. The simulations further illustrate that intensities of the weak decay branches are affected by the coincident summing, e.g. for 1982.5 keV ($I_\gamma = 0.0032\%$, $P_{12} \sim 10P_0$). Hence, intensities of such weak transitions cannot be reliably extracted in the present measurements even at 12 cm counting distance. More importantly, coincident summing contributes significantly at energies higher than 2 MeV and its impact is discussed in the next section. The contribution from summing of three gamma rays will be further reduced by corresponding $\epsilon_{\gamma3} f_{\gamma3}$ and hence is neglected here. It should be mentioned that absolute yield of ^{125}Sn was measured to be $1.36(\pm0.2) \times 10^9$, which is found to be consistent with calculated value using the listed cross-section and the incident neutron flux.

TABLE 5.3: A list of possible pathways for coincident summing of two gamma rays in decay of ^{125}Sn for few energies of interest. Corresponding branching ratio/partial branching ratio in % are indicated in the bracket for each gamma ray.

E_{level} ($I_{\gamma 0}$) keV	l mm	P_0 (%)	$E_{\gamma 1}$($I_{\gamma 1}$) keV	$E_{\gamma 2}$($f_{\gamma 2}$) keV	P_{sum} (%)	P_{12} (%)
1889.9	120	1.7×10^{-4}	1557.3(0.0041)	332.1(100)	2.5×10^{-3}	1.0×10^{-7}
(0.074)			822.5(4.3)	1067.1(100)	1.4×10^{-3}	6.1×10^{-5}
			800.3(1.1)	1089.2(100)	1.3×10^{-3}	1.4×10^{-5}
			469.9(1.5)	1419.7(29)	4.7×10^{-4}	7.1×10^{-6}
1982.9	120	7.1×10^{-6}	915.6(4.1)	1067.1(100)	1.4×10^{-3}	5.9×10^{-5}
(0.0032)			893.4(0.29)	1089.2(100)	1.3×10^{-3}	3.8×10^{-6}
2240.7	9	–	1173.3(0.18)	1067.1(100)	0.14	2.5×10^{-4}
			1151.2(0.11)	1089.2(100)	0.14	1.5×10^{-4}
			890.5(0.009)	1349.4(14.5)		$<1 \times 10^{-5}$
			434.1(0.024)	1806.7(96.8)		$<1 \times 10^{-5}$
			351(0.26)	1889.9(1.06)		$<1 \times 10^{-5}$
			258.3(0.01)	1982.5(0.07)		$<1 \times 10^{-5}$
2275.8	9	4.2×10^{-3}	684.0(0.011)	1591.4(37.9)	4.5×10^{-2}	5.0×10^{-6}
(0.18)			1186.1(0.009)	1089.2(100)	0.15	1.3×10^{-5}
			1208.4(0.008)	1067.1(100)	0.14	1.2×10^{-5}
2288.2	9	–	1220.9(0.27)	1067.1(100)	0.13	3.6×10^{-4}
			1198.7(0.016)	1089.2(100)	0.14	2.2×10^{-5}
			286.2(0.0058)	2002.1(88)	0.22	1.2×10^{-5}

5.5 Impact on the background for $0\nu\beta\beta$ in ^{124}Sn

The main motivation for the present study is to assess the neutron induced background in the ROI close to $Q_{\beta\beta}$(^{124}Sn), namely, 2250 to 2300 keV. For this purpose, the spectrum of the irradiated Sn sample has been measured in a close geometry after $t_c \sim 1$ day and 39 days ($\sim 4T_{1/2}$) as well as after a prolonged cool down period of 1.5 y (see Figure 5.7).
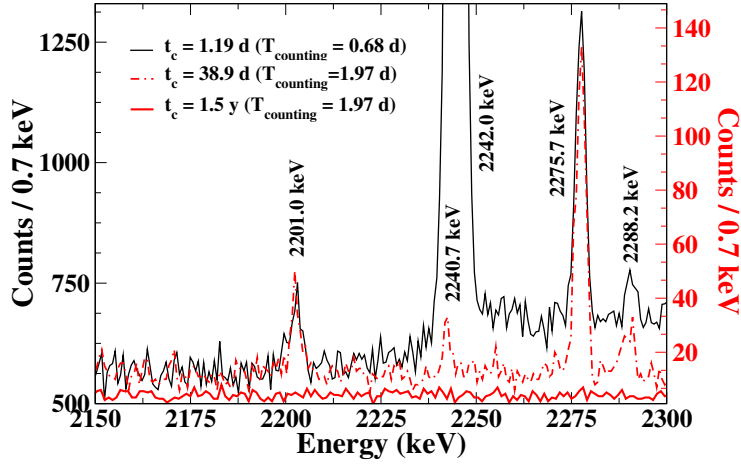
FIGURE 5.7: Comparison of energy spectra in the ROI after different cooldown periods. The left scale corresponds to t_c = 1.19 d, while that for the latter cooling time is indicated on the right side

The energy windows chosen are: (w1) 2282-2300 keV ($Q_{\beta\beta}\pm9$ keV), (w2) 2269-2281 keV (photopeak region of highest energy gamma-ray in the ^{125}Sn decay cascade) and (w3) 2166-2265 keV (as a measure of integral background level). It is important to note that there is no direct gamma transition of 2288.2 keV and observed enhancement in the window w1 results from coincident summing as depicted in Table 5.3. For energy windows w1 and w2, the excess counts above the background are obtained using a Gaussian peak shape together with linear background fit function. In the lower energy window (w3) integral counts are taken into consideration. The ambient background has been measured before and after the counting of the irradiated sample at t_c=1.5 y and is shown in Table 5.4 for energy windows of interest. In the background and t_c = 1.5 y spectra, no peaks are visible in either window and hence the integral counts are listed. In the region of w3, initially the background is dominated by the Compton tail of ^{24}Na γ rays, but shows a significant reduction after t_c ~39 d. Thus, in the spectrum

at t_c ~39 d, weak coincident summing peak corresponding to E=2240.7 keV is also visible. It is evident that counts in both w1 and w2 energy windows show reduction in data sets at t_c ~ 1 and 39 d consistent with $T_{1/2}(^{125}\text{Sn})$. The measured yields are also compared with the expected yield inclusive of coincident summing contribution obtained in simulation. The errors in the simulated spectra are estimated considering 1 mm error in l during the placement of the source (i.e. l=9-10 mm). It can be seen that the measured yield for 2275.7 keV photopeak agrees very well with the corresponding simulated value. For the crucial $Q_{\beta\beta}$ region (i.e. w1) both measured and simulated yields seem to agree within errors, although the experimentally measured mean yield appears to be ~30% higher than the corresponding simulated value.

TABLE 5.4: Background in ROI close to $Q_{\beta\beta}(^{124}\text{Sn})$ for energy windows of interest: w1:2282-2300 keV, w2:2269-2281 keV, w3:2166-2265 keV after different cooldown times (^{125}Sn, $N_{s0} = (1.36 \pm 0.2) \times 10^9$). Shielding configuration of TiLES for each case is also mentioned.

T_c	Window	Yield(exp) (/d)	Yield(sim) (/d)
1.19 d	w1	479(168)*	357(30)
(w/o muon veto)	w2	4213(191)*	3825(559)
	w3	175784(419)	-
38.9 d	w1	36(12)*	23(2)
(w/o muon veto)	w2	275(12)*	250(36)
	w3	972(31)	-
1.5 y	w1	36(6)	
(with muon veto +	w2	28(5)	
passive shield)	w3	204(14)	
Ambient Background	w1	38(6)	
(with muon veto +	w2	24(5)	
passive shield)	w3	193(14)	

* Area of the peak with gaussian+linear background fit

From the measured yield in Table 5.4, the activity due to $^{124}\text{Sn}(n,\gamma)$ in the energy window 2282-2300 keV just after the irradiation is estimated to be 14.4

mBq/g/keV for incident neutron fluence of $3 \times 10^{15}/\text{cm}^2$. It is evident that after the prolonged cooldown period of t_c =1.5 y, integral counts in all three energy windows are similar to the ambient background. However, ^{125}Sb ($T_{1/2}$= 2.76 y) gamma rays are still present in the spectra below 1 MeV. For energy windows w1 and w2, the minimum detectable limit for detection (L_D) can be estimated using Currie's method [19]

$$L_D = 4.65\sigma_B + 2.7 \tag{5.3}$$

where σ_B is the standard deviation in the ambient background level (N_B). Using $\sigma_B = \sqrt{N_B}$, $L_D \sim 25$ μBq/keV is obtained. Hence, the activity of the irradiated sample after t_c =1.5 y is found to be lower than $\sim$1 mBq/g/keV.

It is important to note that the prolonged exposure of ^{124}Sn to thermal neutrons will lead to a build up of ^{125}Sn and the expected equilibrium concentration would be $\sim$K/λ, where K is the production rate and λ is the decay constant. In a Sn detector module, the background contribution in the ROI will arise both from the high energy electrons originating in the beta decay of ^{125}Sn to the ground state of ^{125}Sb (I=81%) and the gamma rays originating after the beta decay of ^{125}Sn to ^{125}Sb($\frac{11}{2}^+$) with feeding fraction I=0.29%. In case of the former, the expected fraction of electrons in this energy window -which is close to Q_β (see Figure 1), is $\sim 1 \times 10^{-3}$. It should be mentioned that the beta decay of ^{125}Sn to states other than the ground state of ^{125}Sb have effective Q value ≤ 1290 keV and hence not relevant for the background consideration in the ROI. Assuming that the decay cascade of ^{125}Sb($\frac{11}{2}^+$) is contained within the detector module, the maximum contribution to the background from gamma rays will be $\sim 3 \times 10^{-3}$ (of the order feeding fraction). To estimate a tolerable neutron dose, based on the observed background in w1 energy range (see table 5.4), a fraction of $\sim 5 \times 10^{-3}$

spread over a 10 keV window is assumed to contribute to the ROI. Therefore, to achieve a desired background rate of 10^{-2} cts/(kg-y-keV) in energy window of 2282-2300 keV, the tin detector material should not be exposed to neutron flux larger than 3×10^{-5} n/cm^2/sec during handling or processing stages.

5.6   Summary

Thermal neutron-induced background has been studied in ^{124}Sn, with a thermal neutron fluence of $\sim 3 \times 10^{15}$/cm^2. The measured intensities of most of the γ rays populated in the decay of ^{125}Sn($\frac{11}{2}^{-}$) are found to be consistent with the literature. The half lives of the γ rays were also tracked to confirm their origin. The high energy γ rays (1368.6 keV and 2754.0 keV) arising from ^{24}Na arising from $^{27}Al(n, \alpha)$ reactions were also observed in the sample, though the source of Al cound not be ascertined. The photopeaks of several high energy γ rays showed higher intensities than expected because of the presence of coincidence summing effects. Photopeak observed at 2288.2 keV arises purely from the coincidence summing effects, as there is no direct γ ray transition at that energy. Monte Carlo simulations were performed for the relevant counting geometry to extract the contribution of coincident summing, for a few high energy γ rays of interest, namely 1889.9, 1982.9, 2240.7, 2275.8, 2288.2 keV, for different possible pathways. The contribution to the background in the ROI for $0\nu\beta\beta$ in ^{124}Sn, namely 2282-2300 keV, from the thermal neutron induced reactions, has been evaluated for a neutron fluence$\sim 3 \times 10^{15}$/cm^2 to be 14.4 mBq/g/keV immediately after the irradiation and reduced to <1 mBq/g/keV after a cool down period of 1.5 y. From measured yield in region of interest near Q$_{\beta\beta}$(^{124}Sn), it is estimated that prolonged exposure to neutron flux exceeding 3×10^{-5} n/cm^2/sec can be a

significant concern for the background.

Summary and future outlook

6.1 Summary

The processes with rare experimental signatures like neutrinoless double beta decay ($0\nu\beta\beta$), interaction of dark matter particles, rare α and β decays etc., are important probes for the Physics beyond the standard model. The extremely rare nature of these processes makes it necessary to reduce the background to unprecedented levels to be able to have the sensitivity to detect the event signature with required significance. Techniques of background reduction thus plays a key role in the next generation large scale experimental efforts aiming to probe these rare processes. The sources of background include the radiation arising from natural radioactivity (α, β, γ rays and neutrons), cosmic ray muons and muon induced shower of secondary particles and cosmogenic activation. Materials of very high radiopurity is chosen for the detector/shield assembly to mitigate the background from surface/bulk impurities. The cosmic muon background is dramatically reduced by deep underground locations with large overburden, typically a few thousands of meter water equivalent. Implementation of active muon veto further

reduces the background from the muons and muon induced secondary particles. To achieve the desired sensitivity levels, a large detector mass, high energy resolution, good efficiency, ultra low background ($\sim$ 0.01 counts keV^{-1}kg^{-1}y^{-1}) and long counting period is necessary. The best background levels (N_{bkg}) in units of keV^{-1}kg^{-1}y^{-1}, achieved by the experiments till date include the $0\nu\beta\beta$ experiments namely, KamLAND-Zen – 1.5×10^{-4}, GERDA – 7×10^{-4}, and direct darkmatter experiments namely, LUX-ZEPLIN(LZ) – 4×10^{-4}, XENON1T – 9×10^{-3}, DARKSIDE-50 – 1×10^{-3} and DEAP-3600 – 3×10^{-4}.

Among all the backgrounds, neutrons are the most difficult to suppress. Neutrons can travel through layers of shield materials without attenuation and lead to background via nuclear excitations through radiative capture or scattering reactions. The resultant γ rays of high energies and the formation of long lived nuclear isomeric states can lead to the deteriorate the background levels. In the case of direct dark matter detection experiments, neutrons act as limiting background since they can produce nuclear recoils via elastic scattering off target nuclei resulting in a signal similar to that of WIMPs (Weakly Interacting Massive Particles). The origin of neutron background is two fold: from natural radioactivity (spontaneous fission and (α, n) reactions) and cosmic muon interactions. The neutrons from natural radioactivity are low in energy E_n < 20 MeV. The cosmic muon induced neutrons on the other hand have a hard spectrum with energies extending $\sim$ 10 GeV in range, though the flux rapidly reduces as the energy increases. The high Z shield materials which are often used for γ ray shielding acts as a source of the production of the secondary neutrons from cosmic muon interactions. The understanding of neutron background from these sources is thus an important factor for all the rare event experimental searches.

Feasibility studies for neutrinoless double beta decay search in ^{124}Sn, The INdia-based TIN detector (TIN.TIN) has been initiated at TIFR. Moderate isotopic abundance ($\sim$ 5%) and Q-value (2.2911$\pm$0.0015 MeV) makes it a suitable candidate for $0\nu\beta\beta$ studies. The development of cryogenic bolometers are underway. Understanding of the background aspects for TIN.TIN is also extremely important to achieve the desired sensitivity levels. In this thesis, study of various aspects of neutron background relevant to the TIN.TIN experiment is carried out.

The novel, high efficiency thermal neutron detectors CLYC and NaIL are characterized for their neutron detection properties using neutrons from ^{241}Am-^{9}Be and ^{252}Cf neutron sources. High detection efficiency, compact size and superior pulse shape discrimination capability makes these ideal for the detection of thermal neutrons. Digital data acquisition for neutron and γ spectroscopy using CLYC and NaIL detectors was setup using CAEN V1730B (16 channel, 14 bit ADC, 500 MS/s, 2 V$_{pp}$) fast digitizer. Monte Carlo simulations were carried out to obtain the intrinsic thermal neutron detection efficiency. The obtained values for intrinsic detection efficiency are 25% and 50%, respectively for CLYC and NaIL detectors. The values are consistent with the values provided by the manufacturer for the specified concentration of ^{6}Li. Different materials are studied for the suitability of using as neutron shield in the low background experiments. Borated rubber with different concentrations of Boron loading were studied for the attenuation of thermal neutrons. The neutron attenuation did not show a strong dependence on the Boron concentration. Neutron attenuation of 90% is obtained with 10% of boron loading and saturates to a value of 92% for 30% boron loading. The γ rays arising from the neutron capture in Hydrogen, at E$_{\gamma}$ = 2.2 MeV, steadily decreased with increasing concentration

of Boron. The thermalization of neutrons in the non-borated HDPE absorber was studied for varying thicknesses. The optimum thickness, that would be suitable for the simultaneous detection of thermal neutrons and neutron capture γ rays, is obtained to be 10 cm. Fast neutron irradiation was performed at the Pelletron-Linac facility at TIFR, to evaluate the suitability of the absorber materials for application in low background studies. Fast neutrons were produced from ^{9}Be(p,n)^{9}B (Q = -1.850 MeV) reaction. Proton beams of energy E$_P \sim$ 20 MeV on a Be target (5 mm thick) were used to obtain an average neutron flux $\sim 10^6$ n cm^{-2} s^{-1} integrated over neutron energy range, E$_n$ = $\sim$ 0.1 to $\sim$18 MeV. The samples were counted in low background HPGe detector to identify the characteristic γ rays arising from the dissolved impurities. The half lives of the γ rays were tracked to confirm the origin. The presence of Zn and Fe impurities was identified in the Borated rubber sample, which may be attributed to the Boron-Zinc compounds used for Boron loading in the rubber. The presence of high energy γ rays, E$_\gamma$ > 1 MeV and long lived isotopes arising from neutron induced reaction in Zn were identified makes it undesirable for the low background applications. The Borated HDPE sample did not show the presence of Zn, but Fe was identified. The origin of Fe in both the samples is not clear. The non-Borated HDPE sample showed the presence of ^{19}F identified by the presence of E$_\gamma$ = 511 keV, arising from ^{19}F(n,2n)^{18}F.

A dedicated setup designed for the measurement of cosmic muon induced neutrons, called as, Muon Induced Neutron measurement setup at TIFR (MINT) is setup at TIFR. The MINT consists of a plastic scintillator for cosmic muon detection, CLYC and NaIL detectors for neutron detection. The neutron detectors are surrounded by 10 cm thick HDPE, to thermalize the fast neutrons arising from

the muon interactions. The efficiency of the plastic scintillators were measured using coincidence techniques before employing in MINT, and found to be in the range of $\sim 95\%$. The overall neutron production in Pb was measured to be 8.1 $\pm$ 2.4 neutrons $g^{-1}cm^2$ day^{-1} for an effective Pb thickness of 30 cm. The contribution to the secondary neutron production from the low energy stopping muons is assessed for Pb and Fe targets. Neutron yield of 4.95 (0.15)$\times 10^{-3}$ neutron/μ and 1.22 (0.23)$\times 10^{-4}$ neutron/μ is obtained for the Pb and Fe targets, respectively. The production from the stopping muons in Pb exceeds the production in Fe by a factor of ~ 40. The compact and portably design of the MINT setup, makes it ideal for the measurements in the underground laboratory locations.

The γ ray background arising from the muon induced fast neutrons was measured in the TiLES low background HPGe setup. The fast neutrons produced in the Pb-Cu composite shield of TiLES, produces γ rays from $(n, n'\gamma)$ reactions in the inner Cu shield and Ge crystal. The cosmic muons entering the TiLES setup are detected using plastic scintillator placed on the top of the setup. The γ ray yield from the cosmic muon induced neutrons is extracted from the co-incident γ ray spectrum in the HPGe detector. Monte Carlo simulations were performed using two versions of GEANT4 toolkit, namely GEANT4.10.00 and GEANT4.10.05, each with two different Physics Lists, QGSP-BERT-HP and Shielding Physics list. The simulations did not show any strong dependence on the Physics lists, but differed significantly for the two versions of GEANT4. While GEANT4.10.00 significantly under-predicts the γ-ray production in Cu, reasonably good agreement with the experimental data is obtained with GEANT4.10.05. The simulations have further shown the presence of several high energy γ rays in the range 2-8 MeV and the contribution of the Compton tail of these high energy

γ-rays to lower energy of interest (2-2.5 MeV) is a background of concern in rare decay studies.The Cu material is an integral part of cryogenic detectors used in rare decay studies and hence the muon induced $(n, n'\gamma)$ data for Cu is very important. The direct contribution of fast neutrons generated from cosmic muon interactions to the γ-ray background via $(n, n'\gamma)$ reactions is investigated for the first time.

Thermal neutron induced γ ray background was investigated to understand its contribution to the ROI of $0\nu\beta\beta$ in ^{124}Sn. A 99.26% Sn sample was irradiated in the Dhruva reactor at BARC, Mumbai. The intensities of the γ rays arising from ^{124}Sn$(n, \gamma)^{125}$Sn. The intensities of most of the γ rays populated in the decay of ^{125}Sn$(\frac{11}{2}^{-})$ are found to be consistent with the literature. The photopeaks of some of the high energy γ rays from the decay of ^{125}Sn, were found to have contribution from the coincidence summing effects. It is important to note the contribution which arises purely from coincidence summing at 2240.7 keV and 2288.2 keV, which is extremely close to the Q$_{\beta\beta}$ in ^{124}Sn. The contribution to the background in the ROI for $0\nu\beta\beta$ in ^{124}Sn, namely 2282-2300 keV, from the thermal neutron induced reactions, has been evaluated for a neutron fluence $\sim 3 \times 10^{15}$/cm^2 to be 14.4 mBq/g/keV immediately after the irradiation and reduced to <1 mBq/g/keV after a cool down period of 1.5 y. From measured yield in region of interest near Q$_{\beta\beta}$(^{124}Sn), it is estimated that prolonged exposure to neutron flux exceeding 3×10^{-5} n/cm^2/sec can be a significant concern for the background.

In summary, various aspects of neutron background, crucial to $0\nu\beta\beta$ in ^{124}Sn have been studied in this thesis, providing key inputs for the TIN.TIN experiment. These studies indicate that thermal neutron capture in ^{124}Sn can give rise to

significant background in ROI near $Q_{\beta\beta}$(^{124}Sn). It is important to restrict the exposure of Tin material to a thermal neutron flux. Prolonged exposure to thermal neutron flux exceeding 3×10^{-5} n/cm^2/sec is a significant consideration for the background. These results suggest that it would be necessary to store Sn material in underground location for extended periods prior to use in the cryogenic bolometer setup. Further, fast neutron induced high energy gammas in Pb also necessitates the careful shield design.

6.2 Future outlook

Various sources of background needs to be studied and minimized to improve the sensitivity of rare event experiments. Materials of high radiopurity and effective radiation shielding are two important factors that can lead to significant improvement in the background aspects. The improvements to the existing low background counting setup will enable probing of lower concentrations of impurities in various materials of importance to TIN.TIN. Further, the relevant aspects of neutron and cosmogenic background and their contribution to the background in the ROI also needs to be understood.

The low background gamma spectroscopy technique has been used to study rare decay events like DBD to the excited states of the daughter nuclei and rare alpha decays. The TiLES low background setup is one of the best experiment setup at the sea level with an impressive background level of 1.7×10^4 /day/kg. Implementation of neutron shield in TiLES can lead to further improvement in the overall background of TiLES. As discussed in Chapter 2, neutrons of $E_n < 10\,MeV$ can be effectively thermalized and attenuated to 90% of the incident neutron flux with the combination HDPE and boron loaded rubber. Neutron

shield composed of HDPE layer and Boron loaded rubber can be mounted inside the existing Pb-Cu γ ray shield to reduce the γ ray background arising from the low energy neutrons.

The MINT set up can be improved further by implementation of plastic scintillators surrounding the setup. The muons entering the setup from all the directions can thus be measured. The study of cosmogenic neutron background in Sn and the associated Monte Carlo simulations can be carried out with the MINT set up. The understanding of γ ray and neutron production from the cosmic muon interactions in Sn, will together provide a crucial understanding of one of the most important background aspects for TIN.TIN. Monte Carlo simulations for the understanding of neutron production for various materials in MINT set up needs to be carried out. As mentioned in Chapter 3, the input from the simulations are necessary to have a direct comparison of the existing measurements with Pb and Fe. The measurements with Sn, would provide a valuble input for the understanding of background for TIN.TIN experiment. The comparison of neutron production in the three targets will also provide a better understanding of the dependence of neutron production with the atomic number.

Activation of materials is known to cause background events in underground experiments that may affect the sensitivity of these experiments to rare event searches. The formation of long lived isomeric states is undesirable in the low background experiments, as discussed in detail in Chapter 1. The understanding of cosmogenic activation in Sn is extremely important for TIN.TIN experiment. The experimental data for the cosmogenic activation in Tin is scarce, which makes these measurements important. The cosmic muons can be detected with plastic scintillators and the resultant γ and X rays can be measured using HPGe

detectors in coincidence with the cosmic muons. The activation in materials such as Cu, which is often a part of the detector and components, can also be studied. The experimental results amongst themselves and in comparison with simulations have shown considerable variations for various cosmogenic backgrounds. These measurements will not only provide valuable input towards the overall understanding of the experimental data but also help to benchmark the Monte Carlo simulations. The improvements in the low background aspects can lead to considerable improvement in the experimental sensitivity.

Bibliography

[1] W. Pauli. "Dear radioactive ladies and gentlemen". In: *Phys.Today* 31N9 (1930), p. 27.

[2] Frederick Reines and Clyde L. Cowan. "The Neutrino". In: *Nature* 178.4531 (1956), pp. 446–449. ISSN: 00280836. DOI: `10.1038/178446a0`.

[3] Ettore Majorana. "Teoria simmetrica dell'elettrone e del positrone". In: *Nuovo Cim.* 14.4 (1937), pp. 171–184. ISSN: 0029-6341. DOI: `10.1007/BF02961314`.

[4] M. Goeppert-Mayer. "Double Beta-Disintegration". In: *Phys. Rev.* 48.6 (1935), pp. 512–516. ISSN: 0031-899X. DOI: `10.1103/PhysRev.48.512`.

[5] A. S. Barabash. "Review of double beta decay experiments". In: (2014), pp. 295–299. DOI: `10.1142/9789814663618_0055`. arXiv: `1403.2870`.

[6] Vandana Nanal. "Is Neutrino its own Antiparticle?" In: *Curr. Sci.* 112.07 (2017), p. 1375. ISSN: 0011-3891. DOI: `10.18520/cs/v112/i07/1375-1380`.

[7] Stefano Dell'Oro et al. "Neutrinoless double beta decay: 2015 review". In: *Adv. High Energy Phys.* 2016 (2016). ISSN: 16877365. DOI: `10.1155/2016/2162659`.

[8] A. Gando et al. "Search for Majorana Neutrinos Near the Inverted Mass Hierarchy Region with KamLAND-Zen". In: *Phys. Rev. Lett.* 117.8 (2016), p. 082503. ISSN: 0031-9007. DOI: `10.1103/PhysRevLett.117.082503`. arXiv: `1605.02889`.

[9] Vandana Nanal. "Search for neutrinoless double beta decay in ^{124}Sn". In: *EPJ Web Conf.* 66 (2014). Ed. by S. Lunardi et al., p. 08005. ISSN: 2100-014X. DOI: `10.1051/epjconf/20146608005`.

[10] Meng Wang et al. "The AME2016 atomic mass evaluation (II). Tables, graphs and references". In: *Chinese Phys. C* 41.3 (2017). ISSN: 16741137. DOI: `10.1088/1674-1137/41/3/030003`.

[11] D.-M. Mei and A. Hime. "Muon-induced background study for underground laboratories". In: *Phys. Rev. D* 73.5 (2006), p. 053004. ISSN: 1550-7998. DOI: `10.1103/PhysRevD.73.053004`. arXiv: `0512125 [astro-ph]`.

[12] I. Abt et al. "The muon-induced neutron indirect detection EXperiment, MINIDEX". In: *Astropart. Phys.* 90 (2017), pp. 1–13. ISSN: 09276505. DOI: `10.1016/j.astropartphys.2017.01.011`.

[13] *ROOT a Data analysis Framework* `https://root.cern.ch/`.

[14] N. Dokania et al. "Characterization and modeling of a low background HPGe detector". In: *Nucl. Instruments Methods Phys. Res. Sect. A Accel. Spectrometers, Detect. Assoc. Equip.* 745 (2014), pp. 119–127. ISSN: 01689002. DOI: `10.1016/j.nima.2014.01.064`. arXiv: 1311.4779.

[15] D Heck et al. *CORSIKA: A Monte Carlo Code to Simulate Extensive Air Showers*. Tech. rep. 1998.

[16] S. Agostinelli et al. "GEANT4 - A simulation toolkit". In: *Nucl. Instruments Methods Phys. Res. Sect. A Accel. Spectrometers, Detect. Assoc. Equip.* 506.3 (2003), pp. 250–303. ISSN: 01689002. DOI: `10.1016/S0168-9002(03)01368-8`.

[17] J. Allison et al. "Recent developments in GEANT4". In: *Nucl. Instruments Methods Phys. Res. Sect. A Accel. Spectrometers, Detect. Assoc. Equip.* 835 (2016), pp. 186–225. ISSN: 01689002. DOI: `10.1016/j.nima.2016.06.125`.

[18] J. Katakura. "Nuclear Data Sheets for A = 125". In: *Nucl. Data Sheets* 112.3 (2011), pp. 495–705. ISSN: 00903752. DOI: `10.1016/j.nds.2011.02.001`.

[19] Lloyd A. Currie. "Limits for qualitative detection and quantitative determination. Application to radiochemistry". In: *Anal. Chem.* 40.3 (1968), pp. 586–593. ISSN: 0003-2700. DOI: `10.1021/ac60259a007`.

[20] C. Patrignani et al. "Review of particle physics". In: *Chinese Phys. C* 40.10 (2016), p. 100001. ISSN: 16741137. DOI: `10.1088/1674-1137/40/10/100001`.

[21]   Peter W. Higgs. "Broken symmetries and the masses of gauge bosons". In: *Phys. Rev. Lett.* 13.16 (1964), pp. 508–509. ISSN: 00319007. DOI: `10.1103/PhysRevLett.13.508`.

[22]   F. Englert and R. Brout. "Broken symmetry and the mass of gauge vector mesons". In: *Phys. Rev. Lett.* 13.9 (1964), pp. 321–323. ISSN: 00319007. DOI: `10.1103/PhysRevLett.13.321`.

[23]   G. S. Guralnik, C. R. Hagen, and T. W.B. Kibble. "Global conservation laws and massless particles". In: *Phys. Rev. Lett.* 13.20 (1964), pp. 585–587. ISSN: 00319007. DOI: `10.1103/PhysRevLett.13.585`.

[24]   G. Aad et al. "Observation of a new particle in the search for the Standard Model Higgs boson with the ATLAS detector at the LHC". In: *Phys. Lett. Sect. B Nucl. Elem. Part. High-Energy Phys.* 716.1 (2012), pp. 1–29. ISSN: 03702693. DOI: `10.1016/j.physletb.2012.08.020`. arXiv: `1207.7214`.

[25]   Pablo F. de Salas et al. "Neutrino Mass Ordering from Oscillations and Beyond: 2018 Status and Future Prospects". In: *Front. Astron. Sp. Sci.* 5 (2018). ISSN: 2296-987X. DOI: `10.3389/fspas.2018.00036`. arXiv: `1806.11051`.

[26]   M. H. Ahn et al. "Indications of Neutrino Oscillation in a 250 km Long-Baseline Experiment". In: *Phys. Rev. Lett.* 90.4 (2003), p. 041801. ISSN: 0031-9007. DOI: `10.1103/PhysRevLett.90.041801`. arXiv: `0212007` `[hep-ex]`.

[27]   A. Gando et al. "Constraints on $\theta 13$ from a three-flavor oscillation analysis of reactor antineutrinos at KamLAND". In: *Phys. Rev. D - Part.*

Fields, Gravit. Cosmol. 83.5 (2011), p. 052002. ISSN: 15507998. DOI: 10.1103/PhysRevD.83.052002. arXiv: 1009.4771.

[28] P. Adamson et al. "Measurement of the neutrino mass splitting and flavor mixing by minos". In: *Phys. Rev. Lett.* 106.18 (2011), p. 181801. ISSN: 00319007. DOI: 10.1103/PhysRevLett.106.181801. arXiv: 1103.0340.

[29] B. Aharmim et al. "Combined analysis of all three phases of solar neutrino data from the Sudbury Neutrino Observatory". In: *Phys. Rev. C - Nucl. Phys.* 88.2 (2013), p. 025501. ISSN: 1089490X. DOI: 10.1103/PhysRevC.88.025501. arXiv: 1109.0763.

[30] C. Bauer et al. "Background-free search for neutrinoless double-β decay of ^{76}Ge with GERDA". In: *Nature* 544.7648 (2017), pp. 47–52. ISSN: 0028-0836. DOI: 10.1038/nature21717. arXiv: 1703.00570.

[31] C. Alduino et al. "Study of rare nuclear processes with CUORE". In: *Int. J. Mod. Phys. A* 33.9 (2018). ISSN: 0217751X. DOI: 10.1142/S0217751X18430029. arXiv: 1801.05403.

[32] R. Bernabei et al. "New results from DAMA/LIBRA". In: *Eur. Phys. J. C* 67.1 (2010), pp. 39–49. ISSN: 14346044. DOI: 10.1140/epjc/s10052-010-1303-9. arXiv: 1002.1028.

[33] J. Cherwinka et al. "First data from DM-Ice17". In: *Phys. Rev. D - Part. Fields, Gravit. Cosmol.* 90.9 (2014), p. 092005. ISSN: 15502368. DOI: 10.1103/PhysRevD.90.092005. arXiv: 1401.4804.

[34]   R. Agnese et al. "Search for Low-Mass Weakly Interacting Massive Particles Using Voltage-Assisted Calorimetric Ionization Detection in the SuperCDMS Experiment". In: *Phys. Rev. Lett.* 112.4 (2014), p. 041302. ISSN: 0031-9007. DOI: 10.1103/PhysRevLett.112.041302. arXiv: 1309.3259.

[35]   E Aprile et al. "Dark Matter Search Results from a One Ton-Year Exposure of XENON1T". In: *Phys. Rev. Lett.* 121.11 (2018), p. 111302. ISSN: 0031-9007. DOI: 10.1103/PhysRevLett.121.111302.

[36]   P. Agnes et al. "DarkSide-50 532-day dark matter search with low-radioactivity argon". In: *Phys. Rev. D* 98.10 (2018), p. 102006. ISSN: 24700029. DOI: 10.1103/PhysRevD.98.102006. arXiv: 1802.07198.

[37]   E. Aprile et al. "Observation of two-neutrino double electron capture in ^{124}Xe with XENON1T". In: *Nature* 568.7753 (2019), pp. 532–535. ISSN: 14764687. DOI: 10.1038/s41586-019-1124-4. arXiv: 1904.11002.

[38]   Vitaly A. Kudryavtsev. "Cosmogenic activation: Recent results". In: *AIP Conf. Proc.* Vol. 1921. 1. 2018, p. 090004. DOI: 10.1063/1.5022583.

[39]   S. Cebrián et al. "Cosmogenic activation in germanium double beta decay experiments". In: *J. Phys. Conf. Ser.* Vol. 39. 1. Institute of Physics Publishing, 2006, pp. 344–346. DOI: 10.1088/1742-6596/39/1/089.

[40]   S. Cebrián et al. "Cosmogenic activation in germanium and copper for rare event searches". In: *Astropart. Phys.* 33.5-6 (2010), pp. 316–329. ISSN: 09276505. DOI: 10.1016/j.astropartphys.2010.03.002.

[41] C. Arpesella et al. "Measurements of extremely low radioactivity levels in BOREXINO". In: *Astropart. Phys.* 18.1 (2002), pp. 1–25. ISSN: 09276505. DOI: 10.1016/S0927-6505(01)00179-7. arXiv: 0109031 [hep-ex].

[42] G. Zuzel and H. Simgen. "High sensitivity radon emanation measurements". In: *Appl. Radiat. Isot.* 67.5 (2009), pp. 889–893. ISSN: 09698043. DOI: 10.1016/j.apradiso.2009.01.052.

[43] Hardy Simgen. "Radon assay and purification techniques". In: *AIP Conf. Proc.* Vol. 1549. 1. American Institute of Physics, 2013, pp. 102–107. ISBN: 9780735411746. DOI: 10.1063/1.4818086.

[44] K. Pushkin et al. "Study of radon reduction in gases for rare event search experiments". In: *Nucl. Instruments Methods Phys. Res. Sect. A Accel. Spectrometers, Detect. Assoc. Equip.* 903 (2018), pp. 267–276. ISSN: 01689002. DOI: 10.1016/j.nima.2018.06.076. arXiv: 1805.11306.

[45] R. Agnese et al. "Search for low-mass dark matter with CDMSlite using a profile likelihood fit". In: *Phys. Rev. D* 99.6 (2019), p. 062001. ISSN: 2470-0010. DOI: 10.1103/PhysRevD.99.062001. arXiv: 1808.09098.

[46] G. Angloher et al. "Results from low mass WIMPs using an upgraded CRESST-II detector". In: *Eur. Phys. J. C 2014 7412* 74.12 (2014), pp. 1–6. DOI: 10.1140/EPJC.

[47] Xiangyi Cui et al. "Dark Matter Results from 54-Ton-Day Exposure of PandaX-II Experiment". In: *Phys. Rev. Lett.* 119.18 (2017), p. 181302. ISSN: 10797114. DOI: 10.1103/PhysRevLett.119.181302. arXiv: 1708.06917.

[48] D. S. Akerib et al. "Liquid xenon scintillation measurements and pulse shape discrimination in the LUX dark matter detector". In: *Phys. Rev. D* 97.11 (2018), p. 112002. ISSN: 24700029. DOI: `10.1103/PhysRevD.97.112002`. arXiv: `1802.06162`.

[49] A. S. Barabash et al. "Calorimeter development for the SuperNEMO double beta decay experiment". In: *Nucl. Instruments Methods Phys. Res. Sect. A Accel. Spectrometers, Detect. Assoc. Equip.* 868 (2017), pp. 98–108. ISSN: 01689002. DOI: `10.1016/j.nima.2017.06.044`.

[50] M. Goldhaber, L. Grodzins, and A. W. Sunyar. "Helicity of neutrinos [7]". In: *Phys. Rev.* 109.3 (1958), pp. 1015–1017. ISSN: 0031899X. DOI: `10.1103/PhysRev.109.1015`.

[51] Raymond Davis, Don S. Harmer, and Kenneth C. Hoffman. "Search for neutrinos from the sun". In: *Phys. Rev. Lett.* 20.21 (1968), pp. 1205–1209. ISSN: 00319007. DOI: `10.1103/PhysRevLett.20.1205`.

[52] J. N. Bahcall et al. "Solar Neutrino Flux." In: *Astrophys. J.* 137 (1963), p. 344. ISSN: 0004-637X. DOI: `10.1086/147513`.

[53] Y. Fukuda et al. "Evidence for oscillation of atmospheric neutrinos". In: *Phys. Rev. Lett.* 81.8 (1998), pp. 1562–1567. ISSN: 10797114. DOI: `10.1103/PhysRevLett.81.1562`. arXiv: `9807003` `[hep-ex]`.

[54] Q. R. Ahmad et al. "Measurement of the rate of $\nu_e + d \rightarrow p + p + e$ interactions produced by ^{8}B solar neutrinos at the sudbury neutrino observatory". In: *Phys. Rev. Lett.* 87.7 (2001), pp. 71301–1–71301–4. ISSN: 10797114. DOI: `10.1103/PhysRevLett.87.071301`. arXiv: `0106015` `[nucl-ex]`.

[55] G. Alimonti et al. "Science and technology of Borexino: A real-time detector for low energy solar neutrinos". In: *Astropart. Phys.* 16.3 (2002), pp. 205–234. ISSN: 09276505. DOI: `10.1016/S0927-6505(01)00110-4`.

[56] M. Altmann et al. "Complete results for five years of GNO solar neutrino observations". In: *Phys. Lett. Sect. B Nucl. Elem. Part. High-Energy Phys.* 616.3-4 (2005), pp. 174–190. ISSN: 03702693. DOI: `10.1016/j.physletb.2005.04.068`.

[57] J. N. Abdurashitov et al. "Measurement of the solar neutrino capture rate with gallium metal. III. Results for the 2002-2007 data-taking period". In: *Phys. Rev. C - Nucl. Phys.* 80.1 (2009), p. 015807. ISSN: 1089490X. DOI: `10.1103/PhysRevC.80.015807`.

[58] F. Kaether et al. "Reanalysis of the Gallex solar neutrino flux and source experiments". In: *Phys. Lett. Sect. B Nucl. Elem. Part. High-Energy Phys.* 685.1 (2010), pp. 47–54. ISSN: 03702693. DOI: `10.1016/j.physletb.2010.01.030`.

[59] A. Gando et al. "^{7}Be solar neutrino measurement with KamLAND". In: *Phys. Rev. C - Nucl. Phys.* 92.5 (2015), p. 055808. ISSN: 1089490X. DOI: `10.1103/PhysRevC.92.055808`.

[60] K. Eguchi et al. "First Results from KamLAND: Evidence for Reactor Antineutrino Disappearance". In: *Phys. Rev. Lett.* 90.2 (2003), p. 021802. ISSN: 10797114. DOI: `10.1103/PhysRevLett.90.021802`. arXiv: `0212021 [hep-ex]`.

[61]   T. Araki et al. "Measurement of Neutrino Oscillation with KamLAND: Evidence of Spectral Distortion". In: *Phys. Rev. Lett.* 94.8 (2005), p. 081801. ISSN: 0031-9007. DOI: 10.1103/PhysRevLett.94.081801. arXiv: 0406035 [hep-ex].

[62]   S. Abe et al. "Precision measurement of neutrino oscillation parameters with KamLAND". In: *Phys. Rev. Lett.* 100.22 (2008), p. 221803. ISSN: 00319007. DOI: 10.1103/PhysRevLett.100.221803. arXiv: 0801.4589.

[63]   M. H. Ahn et al. "Indications of Neutrino Oscillation in a 250 km Long-Baseline Experiment". In: *Phys. Rev. Lett.* 90.4 (2003), p. 5. ISSN: 10797114. DOI: 10.1103/PhysRevLett.90.041801. arXiv: 0212007 [hep-ex].

[64]   D. G. Michael et al. "Observation of muon neutrino disappearance with the MINOS detectors in the NuMI neutrino beam". In: *Phys. Rev. Lett.* 97.19 (2006), p. 191801. ISSN: 00319007. DOI: 10.1103/PhysRevLett.97.191801. arXiv: 0607088 [hep-ex].

[65]   Ziro Maki, Masami Nakagawa, and Shoichi Sakata. "Remarks on the Unified Model of Elementary Particles". In: *Prog. Theor. Phys.* 28.5 (1962), pp. 870–880. ISSN: 0033-068X. DOI: 10.1143/ptp.28.870.

[66]   W. H. Furry. "On Transition Probabilities in Double Beta-Disintegration". In: *Phys. Rev.* 56.12 (1939), pp. 1184–1193. ISSN: 0031-899X. DOI: 10.1103/PhysRev.56.1184.

[67]   S. R. Elliott, A. A. Hahn, and M. K. Moe. "Direct evidence for two-neutrino double-beta decay in ^{82}Se". In: *Phys. Rev. Lett.* 59.18 (1987),

pp. 2020–2023. ISSN: 00319007. DOI: `10.1103/PhysRevLett.59.2020`.

[68] T. D. Lee and C. N. Yang. "Question of parity conservation in weak interactions". In: *Phys. Rev.* 104.1 (1956), pp. 254–258. ISSN: 0031899X. DOI: `10.1103/PhysRev.104.254`.

[69] C. S. Wu et al. "Experimental Test of Parity Conservation in Beta Decay". In: *Phys. Rev.* 105.4 (1957), pp. 1413–1415. ISSN: 0031-899X. DOI: `10.1103/PhysRev.105.1413`.

[70] L. Winslow and R. Simpson. "Characterizing quantum-dot-doped liquid scintillator for applications to neutrino detectors". In: *J. Instrum.* 7.07 (2012), P07010. ISSN: 1748-0221. DOI: `10.1088/1748-0221/7/07/P07010`. arXiv: `1202.4733`.

[71] S. R. Elliott et al. "Initial Results from the Majorana Demonstrator". In: *J. Phys. Conf. Ser.* Vol. 888. 1. Institute of Physics Publishing, 2017, p. 012035. DOI: `10.1088/1742-6596/888/1/012035`. arXiv: `1610.01210`.

[72] N. Abgrall et al. "The large enriched germanium experiment for neutrino-less double beta decay (LEGEND)". In: *AIP Conf. Proc.* Vol. 1894. American Institute of Physics Inc., 2017, p. 020027. ISBN: 9780735415775. DOI: `10.1063/1.5007652`. arXiv: `1810.00849`.

[73] C. Alduino et al. "Study of rare nuclear processes with CUORE". In: *Int. J. Mod. Phys. A* 33.09 (2018), p. 1843002. ISSN: 0217-751X. DOI: `10.1142/S0217751X18430029`. arXiv: `1801.05403`.

[74]   O. Azzolini et al. "Search of the neutrino-less double beta decay of ^{82} Se into the excited states of ^{82} Kr with CUPID-0". In: *Eur. Phys. J. C* 78.11 (2018). ISSN: 14346052. DOI: `10.1140/epjc/s10052-018-6340-9`. arXiv: `1807.00665`.

[75]   O. Azzolini et al. "Final Result of CUPID-0 Phase-I in the Search for the ^{82}Se Neutrinoless Double-β Decay". In: *Phys. Rev. Lett.* 123.3 (2019), p. 032501. ISSN: 10797114. DOI: `10.1103/PhysRevLett.123.032501`.

[76]   J. B. Albert et al. "Search for Majorana neutrinos with the first two years of EXO-200 data". In: *Nature* 510.7504 (2014), pp. 229–234. ISSN: 14764687. DOI: `10.1038/nature13432`. arXiv: `1402.6956`.

[77]   J. B. Albert et al. "Sensitivity and discovery potential of the proposed nEXO experiment to neutrinoless double-β decay". In: *Phys. Rev. C* 97.6 (2018), p. 065503. ISSN: 24699993. DOI: `10.1103/PhysRevC.97.065503`. arXiv: `1710.05075`.

[78]   J. J. Gomez-Cadenas. "The NEXT experiment". In: *Nucl. Part. Phys. Proc.* 273-275 (2016), pp. 1732–1739. ISSN: 24056014. DOI: `10.1016/j.nuclphysbps.2015.09.279`.

[79]   R. Arnold et al. "Results of the search for neutrinoless double-β decay in ^{100}Mo with the NEMO-3 experiment". In: *Phys. Rev. D - Part. Fields, Gravit. Cosmol.* 92.7 (2015), p. 072011. ISSN: 15502368. DOI: `10.1103/PhysRevD.92.072011`.

[80]   S. Andringa et al. "Current Status and Future Prospects of the SNO+ Experiment". In: *Adv. High Energy Phys.* 2016 (2016), pp. 1–21. ISSN: 1687-7357. DOI: `10.1155/2016/6194250`. arXiv: `1508.05759`.

[81] L. A. Winslow. "Discovering the Majorana neutrino: The next generation of experiments". In: *AIP Conf. Proc.* Vol. 1666. American Institute of Physics Inc., 2015, p. 170005. ISBN: 9780735413139. DOI: `10.1063/1.4915595`.

[82] V. Alenkov et al. "First results from the AMoRE-Pilot neutrinoless double beta decay experiment". In: *Eur. Phys. J. C* 79.9 (2019). ISSN: 14346052. DOI: `10.1140/epjc/s10052-019-7279-1`. arXiv: `1903.09483`.

[83] Joachim Ebert et al. "Results of a search for neutrinoless double-β decay using the COBRA demonstrator". In: *Phys. Rev. C* 94.2 (2016), p. 024603. ISSN: 24699993. DOI: `10.1103/PhysRevC.94.024603`. arXiv: `1509.04113`.

[84] A. S. Barabash et al. "Final results of the Aurora experiment to study 2β decay of ^{116}Cd with enriched ^{116}CdWO4 crystal scintillators". In: *Phys. Rev. D* 98.9 (2018), p. 092007. ISSN: 24700029. DOI: `10.1103/PhysRevD.98.092007`.

[85] O. G. Polischuk et al. "New limit on two neutrino electron capture with positron emission in ^{106}Cd". In: *AIP Conf. Proc.* Vol. 2165. 1. American Institute of Physics Inc., 2019, p. 020020. ISBN: 9780735419100. DOI: `10.1063/1.5130981`.

[86] D. S. Akerib et al. "Projected WIMP sensitivity of the LUX-ZEPLIN (LZ) dark matter experiment". In: (2018). arXiv: `1802.06039`.

[87] Xiangyi Cui et al. "Dark Matter Results from 54-Ton-Day Exposure of PandaX-II Experiment". In: *Phys. Rev. Lett.* 119.18 (2017), p. 181302.

ISSN: 0031-9007. DOI: `10.1103/PhysRevLett.119.181302`. arXiv: `1708.06917`.

[88]   R. Ajaj et al. "Search for dark matter with a 231-day exposure of liquid argon using DEAP-3600 at SNOLAB". In: *Phys. Rev. D* 100.2 (2019), p. 022004. ISSN: 2470-0010. DOI: `10.1103/physrevd.100.022004`. arXiv: `1902.04048`.

[89]   R. Bernabei et al. "New limits on WIMP search with large-mass low-radioactivity NaI(T1) set-up at Gran Sasso". In: *Phys. Lett. Sect. B Nucl. Elem. Part. High-Energy Phys.* 389.4 (1996), pp. 757–766. ISSN: 03702693. DOI: `10.1016/S0370-2693(96)80020-7`.

[90]   R. Bernabei et al. "Investigation on light dark matter". In: *Mod. Phys. Lett. A* 23.26 (2008), pp. 2125–2140. ISSN: 02177323. DOI: `10.1142/S0217732308027473`. arXiv: `0802.4336`.

[91]   R. Bernabei et al. "The DAMA/LIBRA apparatus". In: *Nucl. Instruments Methods Phys. Res. Sect. A Accel. Spectrometers, Detect. Assoc. Equip.* 592.3 (2008), pp. 297–315. ISSN: 01689002. DOI: `10.1016/j.nima.2008.04.082`. arXiv: `0804.2738`.

[92]   R. Bernabei et al. "Final model independent result of DAMA/LIBRAâĂŞphase1". In: *Eur. Phys. J. C* 73.12 (2013), p. 2648. ISSN: 1434-6044. DOI: `10.1140/epjc/s10052-013-2648-7`.

[93]   R. Bernabei et al. "First model independent results from DAMA/LIBRA-Phase2". In: *Nucl. Phys. At. Energy* 19.4 (2018), pp. 307–325. ISSN: 20740565. DOI: `10.15407/jnpae2018.04.307`. arXiv: `1805.10486`.

[94] J. Amaré et al. "First Results on Dark Matter Annual Modulation from the ANAIS-112 Experiment". In: *Phys. Rev. Lett.* 123.3 (2019), p. 031301. ISSN: 10797114. DOI: `10.1103/PhysRevLett.123.031301`.

[95] G. Adhikari et al. "Search for a Dark Matter-Induced Annual Modulation Signal in NaI(Tl) with the COSINE-100 Experiment". In: *Phys. Rev. Lett.* 123.3 (2019), p. 031302. ISSN: 10797114. DOI: `10.1103/PhysRevLett.123.031302`. arXiv: `1903.10098`.

[96] E. Barbosa De Souza et al. "First search for a dark matter annual modulation signal with NaI(Tl) in the Southern Hemisphere by DM-Ice17". In: *Phys. Rev. D* 95.3 (2017), p. 032006. ISSN: 24700029. DOI: `10.1103/PhysRevD.95.032006`. arXiv: `1602.05939`.

[97] M. Antonello et al. "Monte Carlo simulation of the SABRE PoP background". In: *Astropart. Phys.* 106 (2019), pp. 1–9. ISSN: 09276505. DOI: `10.1016/j.astropartphys.2018.10.005`. arXiv: `1806.09344`.

[98] A. Best et al. "Underground nuclear astrophysics: Why and how". In: *Eur. Phys. J. A* 52.4 (2016), p. 0355503. ISSN: 1434601X. DOI: `10.1140/epja/i2016-16072-7`.

[99] P. Belli et al. "Experimental searches for rare alpha and beta decays". In: *Eur. Phys. J. A* 55.8 (2019). ISSN: 1434601X. DOI: `10.1140/epja/i2019-12823-2`. arXiv: `1908.11458`.

[100] Naba K. Mondal. "India-based neutrino observatory". In: *Pramana - J. Phys.* Vol. 79. 5. Indian Academy of Sciences, 2012, pp. 1003–1020. DOI: `10.1007/s12043-012-0444-9`.

[101]   J. Dawson et al. "Search for double-β decays of tin isotopes with enhanced sensitivity". In: *Phys. Rev. C - Nucl. Phys.* 78.3 (2008). ISSN: 1089490X. DOI: 10.1103/PhysRevC.78.035503.

[102]   A. S. Barabash et al. "Search for β+ EC and ECEC processes in ^{112}Sn and β- β- decay of ^{124}Sn to the excited states of ^{124}Te". In: *Nucl. Phys. A* 807.3-4 (2008), pp. 269–281. ISSN: 03759474. DOI: 10.1016/j.nuclphysa.2008.04.009. arXiv: 0804.3849.

[103]   V SINGH et al. "Cryogen-free dilution refrigerator for bolometric search of neutrinoless double beta decay ($0\nu\beta\beta$) in ^{124}Sn". In: *Pramana* 81.4 (2013), pp. 719–725. ISSN: 0304-4289. DOI: 10.1007/s12043-013-0601-9.

[104]   S. Mathimalar et al. "Characterization of Neutron Transmutation Doped (NTD) Ge for low temperature sensor development". In: *Nucl. Instruments Methods Phys. Res. Sect. B Beam Interact. with Mater. Atoms* 345 (2015), pp. 33–36. ISSN: 0168583X. DOI: 10.1016/j.nimb.2014.12.020.

[105]   A. Garai et al. "Development of NTD Ge Sensors for Superconducting Bolometer". In: *J. Low Temp. Phys.* 184.3-4 (2016), pp. 609–614. ISSN: 15737357. DOI: 10.1007/s10909-015-1379-6.

[106]   M. M. Bourne et al. "Characterization of the CLYC detector for neutron and photon detection". In: *Nucl. Instruments Methods Phys. Res. Sect. A Accel. Spectrometers, Detect. Assoc. Equip.* 736 (2014), pp. 124–127. ISSN: 01689002. DOI: 10.1016/j.nima.2013.10.030.

[107] M. B. Smith et al. "Fast neutron measurements using Cs_2LiYCl_6:Ce (CLYC) scintillator". In: *Nucl. Instruments Methods Phys. Res. Sect. A Accel. Spectrometers, Detect. Assoc. Equip.* 784 (2015), pp. 162–167. ISSN: 01689002. DOI: `10.1016/j.nima.2014.09.021`.

[108] Li Kui-Nian et al. "Characterization of the new scintillator CLYC". In: (2016). arXiv: `1608.08696`.

[109] Sabyasachi Paul et al. "Measurement of neutron spectra generated from bombardment of 4 to 24 MeV protons on a thick ^{9}Be target and estimation of neutron yields". In: *Rev. Sci. Instrum.* 85.6 (2014), p. 063501. ISSN: 10897623. DOI: `10.1063/1.4880202`.

[110] A. Da Silva et al. "Neutron background for a dark matter experiment at a shallow depth site". In: *Nucl. Instruments Methods Phys. Res. Sect. A Accel. Spectrometers, Detect. Assoc. Equip.* 354.2-3 (1995), pp. 553–559. ISSN: 01689002. DOI: `10.1016/0168-9002(94)01049-8`.

[111] F. Boehm et al. "Neutron production by cosmic-ray muons at shallow depth". In: *Phys. Rev. D* 62.9 (2000), p. 092005. ISSN: 0556-2821. DOI: `10.1103/PhysRevD.62.092005`. arXiv: `0006014 [hep-ex]`.

[112] Holger Martin Kluck. "Measurement of the cosmic-induced neutron yield at the Modane underground laboratory". PhD thesis. 2013.

[113] L. Reichhart et al. "Measurement and simulation of the muon-induced neutron yield in lead". In: *Astropart. Phys.* 47 (2013), pp. 67–76. ISSN: 09276505. DOI: `10.1016/j.astropartphys.2013.06.002`. arXiv: `1302.4275`.

[114] LVD Collaboration. "Measurement of the Neutron Flux Produced by Cosmic-Ray Muons with LVD at Gran Sasso". In: (1999). arXiv: `9905047 [hep-ex]`.

[115] C. Zhang and D.-M. Mei. "Measuring muon-induced neutrons with liquid scintillation detector at Soudan mine". In: *Phys. Rev. D* 90.12 (2014), p. 122003. ISSN: 1550-7998. DOI: `10.1103/PhysRevD.90.122003`.

[116] O. M. Horn. "Simulations of the Muon-Induced Neutron Background of the EDELWEISS-II Experiment for Dark Matter Search". PhD thesis. 2007.

[117] Y.-F. Wang et al. "Predicting neutron production from cosmic-ray muons". In: *Phys. Rev. D* 64.1 (2001), p. 013012. ISSN: 0556-2821. DOI: `10.1103/PhysRevD.64.013012`. arXiv: `0101049 [hep-ex]`.

[118] V.A. Kudryavtsev, N.J.C. Spooner, and J.E. McMillan. "Simulations of muon-induced neutron flux at large depths underground". In: *Nucl. Instruments Methods Phys. Res. Sect. A Accel. Spectrometers, Detect. Assoc. Equip.* 505.3 (2003), pp. 688–698. ISSN: 01689002. DOI: `10.1016/S0168-9002(03)00983-5`. arXiv: `0303007 [hep-ex]`.

[119] A. Lindote et al. "Simulation of neutrons produced by high-energy muons underground". In: *Astropart. Phys.* 31.5 (2009), pp. 366–375. ISSN: 09276505. DOI: `10.1016/j.astropartphys.2009.03.008`. arXiv: `0810.1682`.

[120] R. D. Sard et al. "Evidence for neutrons associated with the stopping of sea level mesons in lead". In: *Phys. Rev.* 74.1 (1948), pp. 97–98. ISSN: 0031899X. DOI: `10.1103/PhysRev.74.97`.

[121]   Gerhart Groetzinger and Gordon W. Mcclure. "Production of neutrons by the capture of cosmic-ray mesons at sea level". In: *Phys. Rev.* 74.3 (1948), pp. 341–342. ISSN: 0031899X. DOI: `10.1103/PhysRev.74.341`.

[122]   A O Vajsenberg. *Muons*. North-Holland, 1967.

[123]   D. F. Measday. "The nuclear physics of muon capture". In: *Phys. Rep.* 354.4-5 (2001), pp. 243–409. ISSN: 03701573. DOI: `10.1016/S0370-1573(01)00012-6`.

[124]   H. Primakoff. "Theory of muon capture". In: *Rev. Mod. Phys.* 31.3 (1959), pp. 802–822. ISSN: 00346861. DOI: `10.1103/RevModPhys.31.802`.

[125]   N. Dokania et al. "New limit for the half-life of double beta decay of ^{94}Zr to the first excited state of ^{94}Mo". In: *Eur. Phys. J. A* 53.4 (2017), p. 74. ISSN: 1434-6001. DOI: `10.1140/epja/i2017-12266-9`.

[126]   G. Cocconi and V. Cocconi Tongiorgi. "Intensity and lateral distribution of the N-component in the extensive showers of the cosmic radiation". In: *Phys. Rev.* 79.4 (1950), pp. 730–732. ISSN: 0031899X. DOI: `10.1103/PhysRev.79.730`.

[127]   D.F. Smart and M.A. Shea. "A review of geomagnetic cutoff rigidities for earth-orbiting spacecraft". In: *Adv. Sp. Res.* 36.10 (2005), pp. 2012–2020. ISSN: 02731177. DOI: `10.1016/j.asr.2004.09.015`.

[128]   V. Khachatryan et al. "Measurement of the charge ratio of atmospheric muons with the CMS detector". In: *Phys. Lett. B* 692.2 (2010), pp. 83–104. ISSN: 03702693. DOI: `10.1016/j.physletb.2010.07.033`. arXiv: `1005.5332`.

[129] *National Nuclear Data Center* `https://www.nndc.bnl.gov/`.

[130] M. S. Boswell et al. "Neutron inelastic scattering in natural Cu as a background in neutrinoless double-β decay experiments". In: *Phys. Rev. C - Nucl. Phys.* 87.6 (2013), p. 064607. ISSN: 1089490X. DOI: `10.1103/PhysRevC.87.064607`.

[131] `https://www.tifr.res.in/$\sim$pell/lamps.html`.

[132] H. R. Verma et al. "The Decay of ^{125g}Sn". In: *J. Phys. Soc. Japan* 48.5 (1980), pp. 1415–1422. ISSN: 13474073. DOI: `10.1143/JPSJ.48.1415`.

[133] I. Tomandl et al. "Nuclear structure study of semi-magic ^{125}Sn via (n,γ) and (d,p) reactions". In: *Phys. Rev. C - Nucl. Phys.* 83.4 (2011), p. 044326. ISSN: 1089490X. DOI: `10.1103/PhysRevC.83.044326`.